UNIVERSITY OF SOUTHAMPTON

FACULTY OF PHYSICAL SCIENCES AND ENGINEERING

School of Physics and Astronomy

ON POLARITON CONDENSATION AND POLARITON-MEDIATED SUPERCONDUCTIVITY IN NOVEL TYPES OF PLANAR MICROCAVITIES

by

Evgeniia Cherotchenko

Thesis for the degree of Doctor of Philosophy

October 2017

UNIVERSITY OF SOUTHAMPTON

ABSTRACT

FACULTY OF PHYSICAL SCIENCES AND ENGINEERING

Physics

Thesis for the degree of Doctor of Philosophy

ON POLARITON CONDENSATION AND POLARITON-MEDIATED SUPERCONDUCTIVITY IN NOVEL TYPES OF PLANAR MICROCAVITIES

by Evgeniia Cherotchenko

The many-body phenomena in photonic structures are of great interest due to the vast area of potential applications. This thesis is devoted to the theoretical investigations of collective phenomena in different types of semiconductor structures, in particular, parabolic quantum wells, hybrid Bose-Fermi structures, and transition metal dichalcogenide monolayers.

It is shown that the experimentally obtained integrated photoluminescence spectra from the parabolic quantum well in a microcavity can be described with the use of the semiclassical Boltzmann equations. However, contrary to expectations, the ladder mechanism of exciton relaxation does not describe the experimental data, as the relaxation processes in the PQW involve transitions from all levels to the ground state.

The theoretical investigation of the light-mediated superconductivity in hybrid Bose-Fermi systems is performed. The critical temperature of the phase transition is shown to increase with the density of the polariton condensate and to decrease with the density of electron gas in the superconducting layer. Also, a possible mechanism of suppression of superconductivity by the external magnetic field is discussed, which differs in the considered case from the conventional Meissner effect, because the magnetic field penetration depth is longer than the thickness of the superconducting layer.

The possibility of polariton condensation in microcavities with embedded monolayers of transition metal dichalcogenides is discussed. It is shown that these structures are highly promising for the room temperature polaritonics. The first observation of the strong coupling regime and exciton-polariton modes in WSe_2 was realised by our collaborators from the Würzburg University. These results have been described by the coupled harmonic oscillator approach.

Table of Contents

List of Tables

List of Figures

DECLARATION OF AUTHORSHIP

I, Evgeniia Cherotchenko, declare that the thesis “On polariton condensation and polariton-mediated superconductivity in different types of planar microcavities” and the work presented in it are my own and has been generated by me as the result of my own original research.

I confirm that:

1. This work was done wholly or mainly while in candidature for a research degree at this University;
2. Where any part of this thesis has previously been submitted for a degree or any other qualification at this University or any other institution, this has been clearly stated;
3. Where I have consulted the published work of others, this is always clearly attributed;
4. Where I have quoted from the work of others, the source is always given. With the exception of such quotations, this thesis is entirely my own work;
5. I have acknowledged all main sources of help;
6. Where the thesis is based on work done by myself jointly with others, I have made clear exactly what was done by others and what I have contributed myself;
7. Parts of this work have been published as:

i. N. Lundt, S. Klembt, E. Cherotchenko, S. Betzold, O. Iff, A. V. Nalitov, M. Klaas, C. P. Dietrich, A. V. Kavokin, S. Höfling and C. Schneider, "Room-temperature Tamm-plasmon exciton-polaritons with a WSe_2 monolayer," *Nature Communications,* vol. 7, 2016

ii. N. Lundt, A. Maryński, E. Cherotchenko, A. Pant, X. Fan, S. Tongay, G. Sęk, A. V. Kavokin, S. Höfling and C. Schneider, "Monolayered $MoSe_2$: A candidate for room temperature polaritonics," *2D Materials,* vol. 4, p. 015006, 2016.

iii. E. D. Cherotchenko, T. Espinosa-Ortega, A. V. Nalitov, I. A. Shelykh and A. V. Kavokin, "Superconductivity in semiconductor structures: the excitonic mechanism," *Superlattices and Microstructures,* vol. 90, pp. 170-175, 2016.

iv. E. S. Sedov, E. D. Cherotchenko, S. M. Arakelian and A. V. Kavokin, "Light propagation in tunable exciton-polariton one-dimensional photonic crystals," *Physical Review B,* vol. 94, p. 125309, 2016.

v. A. V. Trifonov, E. D. Cherotchenko, J. L. Carthy, I. V. Ignatiev, A. Tzimis, S. Tsintzos, Z. Hatzopoulos, P. G. Savvidis and A. V. Kavokin, "Dynamics of the energy relaxation in a parabolic quantum well laser," *Physical Review B,* vol. 93, p. 125304, 2016.

vi. N. Lundt, E. Cherotchenko, O. Iff, X. Fan, Y. Shen, P. Bigenwald, A. Kavokin, S. Höfling and C. Schneider, "The interplay between excitons and trions in a monolayer of $MoSe_2$," *arXiv preprint arXiv:1702.04231,* 2017.

Signed: ....

Date: ....

Acknowledgements

I would like to thank my supervisor Prof. Alexey Kavokin for giving me the opportunity and resources to conduct the research in his group at the University of Southampton, and also for arranging my visits to several international conferences, which were an exceptional experience during my studies.

I am grateful to all colleagues I had a chance to work with. Especially I should mention the experimental group in the University of Würzburg for their experiments on TMDC monolayers that yield to several very nice collaborative articles, Arthur Trifonov for the discussions on the experiment, that we worked on together, and Simone De Liberato for his questions during my progress examinations.

Special thanks are going to all people I worked with during my teaching practice, who helped me a lot in improving my teaching skills.

My gratitude also goes to Evgeniy Sedov, for his reasonable comments during the reading of this thesis.

I thank my grandpa for being proud of me about studying here, and encouraging me to continue the scientific career.

I am greatly indebted to my family: mom, dad, my sisters Ksenia and Polina, and brother Vasiliy. I missed them a lot while being in Southampton, and without their support I would not be able to reach the stage, where I am now.

At last I would like to thank my husband Anton Nalitov for always being with me during these four years, for his ultimate support during my studies, for the unbelievable patience and imperturbability he was showing while I was preparing this manuscript and finally for the infinite amount of cups of tea he made me, that for some reason has become a symbol of steadiness and confidence.

Definitions and Abbreviations

2DEG – Two-dimensional electron gas

BCL – Bosonic Cascade Laser

BCS – Bardeen-Cooper-Schrieffer

BEC – Bose-Einstein Condensate

CVD – Chemical Vapour Deposition

DBR – Distribute Bragg Reflectors

GPE – Gross-Pitaevskii Equation

LPB – Lower Polariton Branch

MC – Microcavity

ML – Monolayer

PL – Photoluminescence

PQW – Parabolic Quantum Well

QCL – Quantum Cascade Laser

QW – Quantum Well

TMDC – Transitional Metal Dichalcogenides

UPB – Upper Polariton Branch

VCSEL – Vertical Cavity Surface Emitting Laser

CW – Continuous Wave

EFC – Equifrequency Contour

HTSC – High Temperature Superconductivity

FDTD – Finite Difference Time Domain

Chapter 1: Introduction

1.1 Excitons and Exciton-Polaritons

1.1.1 Excitons: general description

An exciton is a quasi-particle, composed by an electron and a hole, bound by the Coulomb attraction. The concept of excitons was introduced by Yakov Frenkel [1] for organic molecular crystals. These initially proposed excitons are nowadays referred to as Frenkel excitons. They are characterised by small interparticle distances: in the initial model an electron and a hole were assumed to be localised at the same lattice vertex. They possess high binding energies of the order of hundreds of meV. This type of excitons is typically formed in organic crystals.

Wannier-Mott excitons, proposed in the late 1930s for inorganic semiconductor crystals, have rather different properties [2]. In order to estimate their characteristics let us consider an electron in the conduction band and a hole in the valence band having effective masses m_e and m_h, respectively. The interaction potential between these quasi-particles is considered to be the standard Coulomb interaction:

$$V(r) = \frac{e^2}{\varepsilon r}, \tag{1.1}$$

where r is the interparticle distance and ε is the static dielectric permittivity. Schrödinger equation in this case coincides with the well known equation for the hydrogen atom:

$$\left(-\frac{\hbar^2}{2m_e}\Delta_e - \frac{\hbar^2}{2m_h}\Delta_h - \frac{e^2}{\varepsilon r}\right)\Psi = E\Psi. \tag{1.2}$$

The solution for the bound states ($E < 0$) reads:

$$\Psi_{nlm} = e^{i\boldsymbol{kR}} F_{nlm}(\boldsymbol{r}), \tag{1.3}$$

where n, l, m compose a set of integer quantum numbers, $\boldsymbol{R}$ is the centre-of-mass coordinate, $F_p(\boldsymbol{r})$ is a hydrogen-like wave-function, $\hbar\boldsymbol{k}$ is a momentum that characterizes the translational motion of an electron-hole pair as a unit. Substituting the wave function (1.3) into Eq.(1.2) one can find the exciton eigenenergies. Counted from the bottom of the conduction band they can be written as:

$$E_n(k) = -\frac{\mu e^4}{2\hbar^2\varepsilon^2 n^2} + \frac{\hbar^2 k^2}{2(m_e + m_h)}, \qquad \mu = \left(\frac{1}{m_e} + \frac{1}{m_h}\right)^{-1}. \tag{1.4}$$

This energy at $\boldsymbol{k}$=0 is equal to the binding energy of a stationary exciton. When the electron-hole interactions in real crystals are taken into account, the expression for the eigenvalues becomes more cumbersome [3]. Assuming that the exciton energy can be developed into a series at small $\boldsymbol{k}$**,** one can write:

$$E_s(\boldsymbol{k}) = E_s(0) + \frac{\hbar^2}{m_{i,j}^*} k_i k_j + \cdots, \tag{1.5}$$

where $m_{i,j}^*$ is an effective mass tensor in the s-band:

$$m_{i,j}^* = \hbar^2 \left[\frac{\partial^2 E_s(\boldsymbol{k})}{\partial k_i \partial k_j} \right]_{k=0}^{-1}, \tag{1.6}$$

which reduces to the simplified expression

$$m^* = \hbar^2 \left[\frac{d^2 E_s(k)}{dk^2} \right]_{k=0}^{-1}, \tag{1.7}$$

when the energy $E_s(\boldsymbol{k})$ depends only on the absolute value of the wave vector. The expression (1.5) where only first two terms are left is obtained within the so-called *effective mass approximation*, which is often used in the theory of excitons.

The main difference between Frenkel and Wannier-Mott excitons is that in the former one the electron-hole interaction is much stronger than the intermolecular interactions. In contrast, in semiconductors, where the typical Wannier-Mott excitons are formed, the interatomic coupling is much stronger than the Coulomb interaction between an electron and a hole, so the latter can be treated as a perturbation with respect to the atomic interactions. Usually, these excitons are characterized with Bohr radii larger than the lattice constant of the crystal and binding energies of the order of several meV. However, there are exceptions: excitons in recently discovered monolayers of transition metal dichalcogenides (TMDC) have very high binding energies of the order of 0.5 eV. At the same time, they still can be described within the Wannier-Mott model, because the characteristic Bohr radius of these excitons is one order of magnitude larger than the lattice constant. Some of the properties of TMDC materials are discussed in detail in the last chapter of this work.

In the systems that are studied in this thesis excitons are confined in quantum wells (QWs), which are created by sandwiching one type of semiconductor between layers of different semiconductors having wider band gaps. Essentially, this means that quasi-particles can move freely in two dimensions, while in the direction, perpendicular to the QW layer they acquire energies characterized by size quantization quantum numbers. As a consequence of this confinement, the momentum conservation in the optical transition must be satisfied only in QW plane. This leads to the possibility of coupling the excitons in QWs with photons that have the same parallel to the plane wave vector $\boldsymbol{k}_{||}$ and an arbitrary transverse wave vector $k_{\perp}$. The exciton Hamiltonian accounting for the QW potential reads:

$$H = -\frac{\hbar^2}{2m_e}\nabla_e^2 - \frac{\hbar^2}{2m_h}\nabla_h^2 + V_e(z_e) + V_h(z_h) - \frac{e^2}{\varepsilon|\boldsymbol{r}_e - \boldsymbol{r}_h|}, \qquad (1.8)$$

where $V_e(z_e)$ and $V_h(z_h)$ are confinement potentials for the electron and the hole. The Schrödinger equation with this Hamiltonian can be solved numerically. One of the common simplified methods of solving this type of equations is the variational approach, which consists in minimization of energy over variational parameters, entering the trial wave function. In particular, it is common to take the trial wave function expressed in terms of the centre-of-mass and the relative motion coordinates [4]:

$$\Psi(\boldsymbol{r}_e, \boldsymbol{r}_h) = F(\boldsymbol{R})f(\boldsymbol{\rho})U_e(z_e)U_h(z_h), \qquad (1.9)$$

where $\boldsymbol{\rho} = \boldsymbol{\rho_e} - \boldsymbol{\rho_h}$ is the in-plane radius vector of electron and hole relative motion, $\boldsymbol{r} = (\boldsymbol{\rho}, z)$,

$$\boldsymbol{R} = \frac{m_e\boldsymbol{r}_e + m_h\boldsymbol{r}_h}{m_e + m_h} \qquad (1.10)$$

is the exciton centre-of-mass coordinate, $U_h(z_h), U_e(z_e)$ are the electron and hole wave functions in the direction perpendicular to the QW plane. If the QW width is smaller than the exciton Bohr radius, the function (1.9) can be factorized. After the substitution of function (1.9) into Eq. (1.8) and integration one can come to the form of equation similar to the conventional hydrogen atom problem, which is exactly solvable. In particular, for the exciton ground state one can find the binding energy of the 2D exciton and the Bohr radius:

$$E_B^{2D} = 4E_B^{3D}, \qquad a_B^{2D} = \frac{a_B^{3D}}{2}, \qquad (1.11)$$

with

$$a_B^{3D} = \frac{\hbar^2\varepsilon}{\mu e^2}, \qquad E_B^{3D} = \frac{\hbar^2}{2\mu a_B^{3D}}. \qquad (1.12)$$

In Chapter 4 we show an example of the variational approach application, finding the exciton ground state energy in TMDC monolayers.

If the characteristic distance between the excitons in a gas is much longer than the exciton Bohr radius, excitons can be considered as bosons. The increase of the exciton density leads to the increasing role of the screening effects, weakening electron-hole binding, and eventually it leads to a phase transition to an electron-hole plasma, also referred to as the excitonic Mott transition.

1.1.2 Microcavities

Optical microcavities (MCs) are essentially electromagnetic resonators that allow for the light confinement. In a system, where a QW is embedded into a resonator, the strong coupling regime can be achieved, that leads to the formation of new quasi-particles – exciton-polaritons. Such systems, depending on the type and quality of a MC, can exhibit unique optical properties, such as the Bose-Einstein condensation and polariton lasing, single-photon emission, and many others.

MC spectra are size-dependent: in a microscale cavity the resonant frequencies are sparser than in "macroscale" resonators [5]. The main characteristics of a MC are its quality factor, finesse, and field distribution. The quality factor Q is a measure of non-ideality of the cavity i.e. the rate at which the energy decays from the cavity via different processes such as photon scattering and leakage through the mirrors. Q^{-1} is the fraction of energy, lost in a single oscillation period of the cavity. Mathematically, the quality factor can be expressed as $Q = \omega_c/\delta\omega_c$, where $\delta\omega_c$ is a linewidth of a cavity mode. Finesse of a cavity is the ratio of the free spectral range to the linewidth of a cavity mode: $f = \Delta\omega_c/\delta\omega_c$.

Practical realisations of microcavities strongly vary [4, 5]. The conventional realisation is a planar MC, which is essentially a Fabry-Pérot cavity comprised of two plane mirrors, distributed Bragg reflectors (DBRs), separated by a distance of a few wavelengths of light. Most semiconductor lasers are based on this type of microcavities. Another type of cavities is the micropillar cavity, characterised by axial in-plane symmetry, which is widely used in semiconductor photonics. Spherical mirror MC allows the confinement of light in all three dimensions. An interesting example of the application of such type of resonator is introduced in Ref. [6], where the spherical cavity is coupled to an optical fibre, the initial pump excites the whispering gallery mode inside a cavity, which further propagates in a fibre as in a waveguide.

1.1.2.1 Propagation of light in layered structures

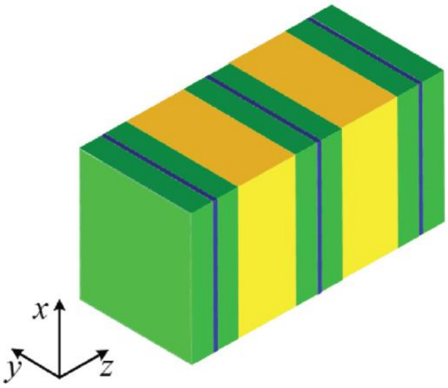

Figure 1.1: A schematic picture of a spatially periodic multilayered structure, consisting of alternating dielectric layers of different widths and refractive indices, with the layers of one type containing single QWs placed in their centres. Figure taken from Ref. [7].

In this subsection the propagation of light in planar microcavities (MCs) with embedded QWs is discussed.

The propagation of light in DBRs as well as in MCs can be modelled by solving Maxwell equations in each layer of DBR or MC and matching the solutions with boundary conditions. For real structures this method can be quite complicated and different techniques like FDTD method are used. However, for planar structures the solution of this problem can be simplified with the use of the transfer matrix method. Essentially planar DBR can be considered as a 1D periodic structure because its refractive index is homogeneous in the xy-plane and it is periodic in the z-direction. The transfer matrix method is a simple and efficient method of solving Maxwell equations in such structures [4, 8].

For simplicity, only the propagation, perpendicular to the layer plane is considered here. Let us define the transfer matrix across the layer of a multilayered structure as:

$$T_L \Phi|_{z=0} = \Phi|_{z=L}, \tag{1.13}$$

where L is a width of a single layer and

$$\Phi(z) = \begin{pmatrix} E(z) \\ cB(z) \end{pmatrix} = \begin{pmatrix} E(z) \\ -\frac{i}{k_0}\partial_z E(z) \end{pmatrix} \tag{1.14}$$

is a vector of amplitudes of electric and magnetic field of incident light, propagating in the z direction. Substituting the explicit form of solutions of wave equations for the amplitudes of electric and magnetic fields [8] into Eq.(1.13), one can express the transfer matrix across the layer:

$$T_L = \begin{pmatrix} \cos(kL) & \frac{i}{n}\sin(kL) \\ in\sin(kL) & \cos(kL) \end{pmatrix}. \tag{1.15}$$

Then the transfer matrix across a structure composed of p layers reads:

$$T = \prod_{i=p}^{1} T_i\,, \tag{1.16}$$

where i is a number of layer.

If a QW is embedded in between of layers, the transfer matrix of propagation trough the QW reads:

$$T_L = \begin{pmatrix} 1 & 0 \\ 2nr_{QW}/t_{QW} & 1 \end{pmatrix}, \tag{1.17}$$

where r_{QW} and $t_{QW} = 1 + r_{QW}$ are the reflection and transmission coefficients of the QW [4]:

$$r_{QW} = \frac{i\Gamma_0}{\omega_X - \omega - i(\Gamma_0 + \gamma)}. \tag{1.18}$$

Here ω_X is the renormalized exciton frequency which, in the approximation of infinitely thin QWs, may be put equal to the exciton frequency, Γ_0 is the exciton radiative decay rate, γ is the non-radiative broadening.

If a layered structure has a period D, then from the transfer matrix method one may derive the band structure for the infinite DBR by solving the equation:

$$\cos(KD) = \left|\frac{T_{11} + T_{22}}{2}\right|, \tag{1.19}$$

where K is a Bloch wave vector.

Figure 1.2 (left panel) shows the propagation of a single femtosecond pulse through the system, composed of three layers of alternating semiconductors with refractive indices n_1 and n_2, where the layer with the higher refractive index is embedded between two layers with lower refractive indices. The shape of the pulse is taken in the Gaussian form:

$$E(z,t) = E_0 exp\left(\frac{(t - t_0)^2}{2t_w^2}\right) exp(-i\omega_C t) exp(-ik_z z), \tag{1.20}$$

where ω_C is the central frequency of the pulse, t_w is a half-duration of the pulse.

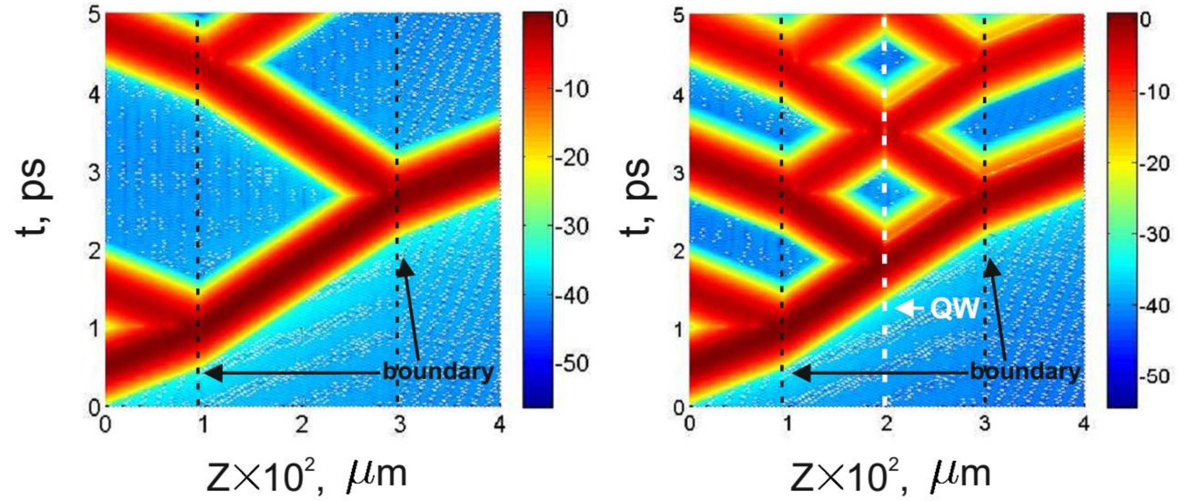

Figure 1.2: The simulation, illustrating the application of the transfer matrix method: the light propagation in altering semiconductor layers without (left panel) and with (right panel) a QW, embedded into the central layer. The intensity is shown in logariphmic scale for better contrast. The refractive index of the edge layers is $n_1 = 1.5$, refractive index of the middle layer $n_2 = 2.5$. The central frequency of the incident light pulse is $\hbar\omega_C = 1.5\text{eV}$. $\hbar\Gamma_0 = \hbar\gamma = 0.01\hbar\omega_C$. Dashed lines show the boundaries between layers and the embedded QW.

The right panel shows the propagation of the same pulse through the system with a QW embedded in the middle of the central layer. The central frequency of the initial wave-packet is chosen to be the resonant frequency of the embedded QW.

Let us now consider the structure schematically shown in Figure 1.1, which was first proposed in Ref. [9]. The structure presents a spatially periodic array of alternating dielectric layers of different widths and refractive indices, with the layers of one type containing single QWs placed in their centres. The presence of cylindrical symmetry in the system is assumed, so one can introduce the in-QW-plane radial coordinate. Here a GaN/$Al_{0.3}Ga_{0.7}N$ DBR with embedded thin $In_{0.12}Ga_{0.88}N$ QWs is considered as a model structure. The thicknesses of the layers and their refractive indices are taken as d_1= 64.8 nm, n_1 = 2.55, and d_2 = 115.3 nm, n_2 = 2.15; the period of the lattice $D = d_1 + d_2$ is 180.1 nm. For the given parameters the structure exhibits a second photonic band gap centred to $\hbar\omega_B \cong$ 3 eV in the QW-free case, see Figure 1.3(a). The QW exciton resonance energy $\hbar\omega_X$ is tuned close to the lower boundary of the second photonic band gap, $\hbar\omega_X \cong$ 2.95 eV. The QW non-radiative decay rate is taken as $\hbar\gamma =$ 0.1 meV. The radiative decay rate $\hbar\Gamma_0$ is a tunable parameter that strongly depends on the applied electric field. Figure 1.3(a) and Figure 1.3(b) demonstrate the dispersion of the light modes in a modified Bragg mirror structure without [Figure 1.3(a)] and with [Figure 1.3(b)] embedded periodically arranged narrow QWs characterized by the radiative decay rate Γ_0 = 2 meV. The presence of QWs leads to two principal changes in the dispersion of the eigenmodes. The first one is the appearance of four dispersion branches instead of the two branches of a QW-free structure due to the vacuum field Rabi-splitting stemming from the QW exciton-photon coupling.

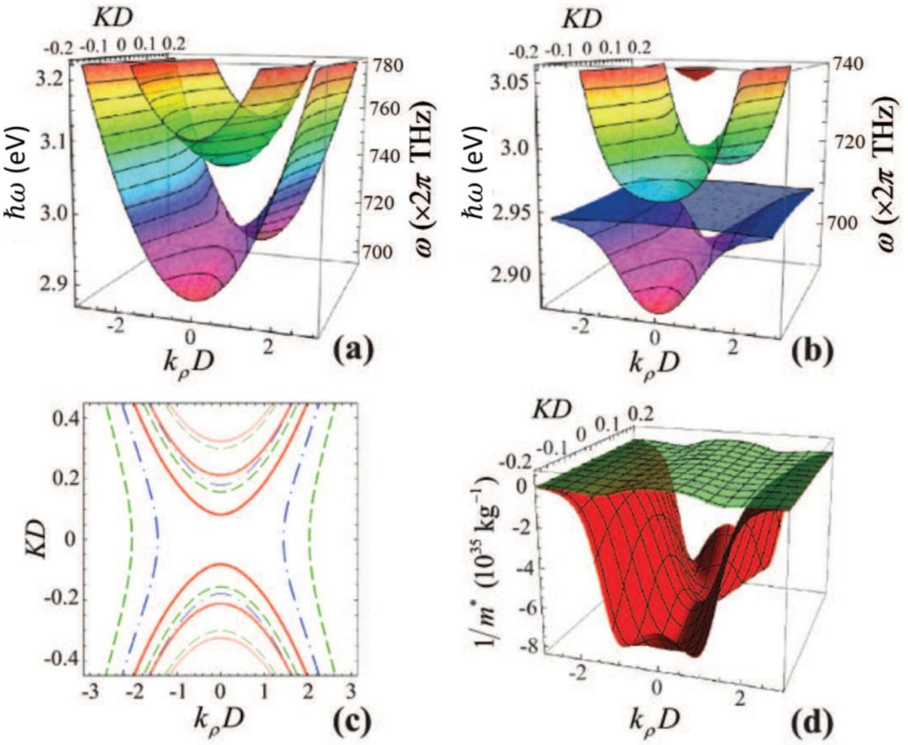

Figure 1.3: Dispersion of the photonic eigenmodes for the structure (a) without and (b) with embedded QWs. (c) Equifrequency contours in the reciprocal space showing the structure of eigenmodes belonging to the lowest dispersion band corresponding to the different values of Γ_0: Γ_0= 0 for the red (solid) curves, Γ_0 = 2 meV for the green (dashed) curves, and Γ_0 = 10 meV for the blue (dash-dotted) curves. Different thicknesses of the curves correspond to different energies ω (from the thickest to the thinnest): 2.94, 2.89, and 2.84 meV, respectively. (d) Inverse exciton-polariton effective mass tensor components in the structure. The red surface corresponds to the effective mass in the z direction, m_z^* (z being the growth axis of the structure), and the green surface corresponds to the in-plane effective mass m_ρ^*. The parameters used in the calculation are given in Ref. [7]. The QW radiative decay rate for (d) is taken as Γ_0 = 2 meV. Figure taken from Ref. [7].

The latter appears when QW exciton is resonant with an eigenmode of the photonic cavity structure. The resulting eigenstates of the system are exciton-polaritons. The other change is the formation of the three-dimensional polaritonic band gap [see Figure 1.3(b)]. It is necessary to mention that the presence of QWs pushes the lowest dispersion branch (LPB) to the lower energies and the higher the value of Γ_0, the greater is the shift. In the limit of weak coupling, the exciton and photon modes cross. In contrast, the strong coupling manifests itself in the anticrossing (avoided crossing) of the modes. The dispersion of the structure eigenmodes is neither photonic nor excitonic, but polaritonic. The increase of the exciton-photon coupling due to the increase of the exciton radiative decay rate results in the growing energy level repulsion.

Interestingly one can observe the dispersionless excitonic branch (Figure 1.3(b), blue surface), which appears when the excitonic resonance frequency is close to the boundary of the photonic band gap, so that the coupling with the closest branch leads to the formation of polariton, while the coupling with the distant photonic branch is very weak, so only exciton can be formed. The experimental observation of this mode in the Bragg crystal with embedded quantum wells is shown in Ref. [10].

Figure 1.3(c) demonstrates equifrequency contours (EFCs) in the (Kk_ρ) plane for a number of lower branch eigenenergies $\hbar\omega$ for different values of Γ_0. It is clearly seen that with the increase of Γ_0 opposite branches of EFCs approach each other until the gap in the K direction closes and the gap in the k_ρ direction opens.

Effective mass tensor is derived from the Equation (1.6):

$$m_{j,\alpha}^{*} = \hbar\left(\frac{\partial^2\omega_j}{\partial k_\alpha^2}\right)^{-1}, \; k_\alpha = K, k_\rho \,, \tag{1.21}$$

and is calculated numerically from the dispersions shown in Figure 1.3(b). The subscript j numerates dispersion branches. The analytical derivation of the effective mass tensor in the vicinity of the saddle point ($k_\rho = 0, K = 0$) is given in Ref. [9]. In the vicinity of the saddle point of the LPB, the effective mass tensor components $m_{\rho,z}^{*} = m_{1,\rho,z}^{*}$ have opposite signs. This is clearly seen in Figure 1.3(d) where the dependencies of the inverse in-plane (green surface) m_ρ^* and transverse (red surface) m_z^* effective masses on the position in the first BZ are shown. One can see that $m_\rho^* > 0$, while $m_z^* < 0$. It also should be mentioned that for the considered model structure the absolute value of m_z^* is at least one order of magnitude lower than m_ρ^*. For example, the ratio $\left| m_\rho^*/m_z^* \right|$ at the saddle point is about 20.1 for QW-free structure, 21.6 for the structure with embedded QWs with Γ_0 = 2 meV, and reaches 30.7 for the structure with Γ_0 = 10 meV. Such a difference introduces a strong anisotropy to the optical properties of the considered structure.

An interesting effect that can be observed is the possibility of light speed manipulation in such structures. The propagating light pulse is again taken in the form of Eq.(1.20). Here the wave packet with a spatial width ρ_w exceeding the in-plane structure size is considered.

The intensity of light is assumed to be uniformly distributed in the QW plane in each layer. The numerical calculations assume the normal incidence geometry. The parameters taken are t_w= 50 fs and t_0= 0.1 ps, $\hbar\omega_C$ = 0.95$\hbar\omega_X \cong$ 2.8 eV, $k_\rho = 0$.

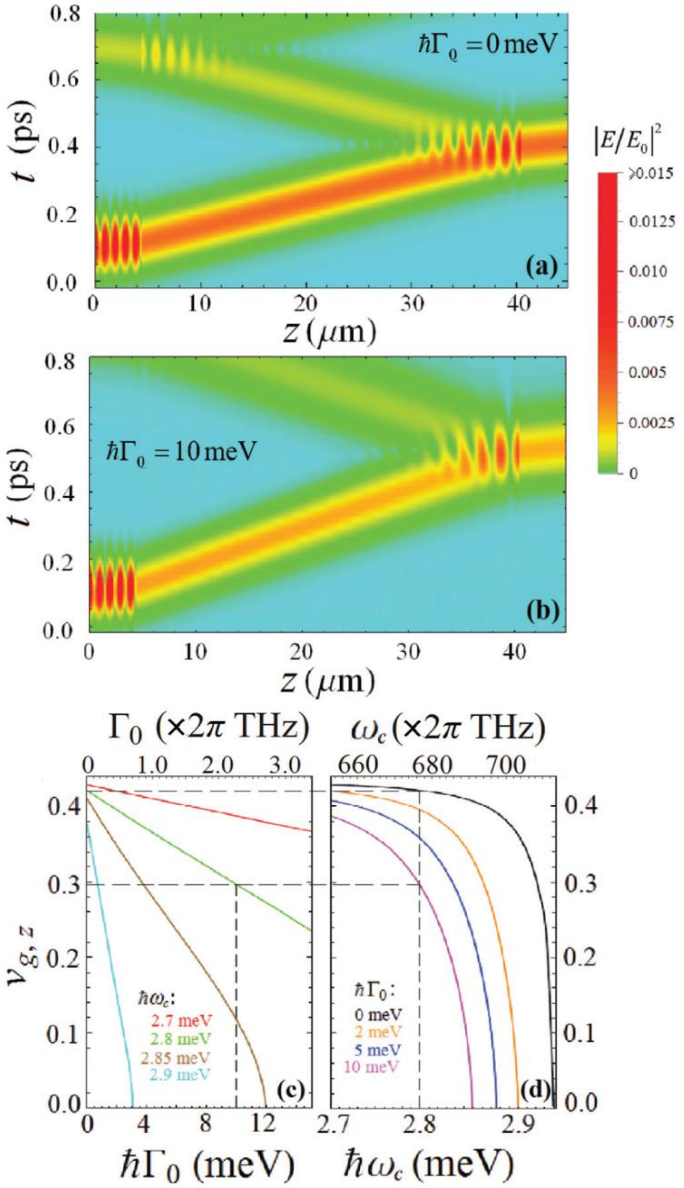

Figure 1.4: A femtosecond laser pulse propagation in the multilayer structure schematically shown in Figure 1.1. The parameter $\hbar\Gamma_0$is taken as (a) 0 meV (which is equivalent to the absence of QWs in the structure) and (b) 10 meV. The regular optical patterns shown in (a) and (b) panels describe the interference of the propagating pulse and the pulses reflected from vacuum-crystal and crystal-vacuum interfaces. Graphs (c) and (d) demonstrate the parametric dependencies of the group velocity of light in the z direction $v_{g,z}$, (a) on Γ_0 for a number of fixed values of the wave packet central frequency component ω_C and (d) on ω_C for different values of Γ_0 with k_ρ= 0. Values of $v_{g,z}$ are given in units of the speed of light in vacuum c. The vertical dashed lines correspond to Γ_0 in (c) and ω_C in (d) from (a) and (b). Horizontal dashed lines indicate the group velocities of the wave packet, with the considered values of Γ_0. Figure taken from Ref. [7].

Figure 1.4(a) and Figure 1.4(b) demonstrate light pulse propagation in the structure calculated for different values of Γ_0. In Figure 1.4(a) Γ_0= 0, which corresponds to the QW-free Bragg mirror. In Figure 1.4(b) the case of a Bragg mirror with embedded QWs characterized by a high radiative decay rate, Γ_0 = 10 meV, is considered. Propagation of light has been modelled in the system starting with a vacuum layer of width $25D$ on the left-hand side of the structure. In the middle part of the system there are 200 periods of photonic crystal, depicted in Figure 1.1 of width D each. The right-most part represents a $25D$ thick vacuum layer again. It is clearly seen that $v_{g,z}$ significantly decreases with the increase of Γ_0. It is also confirmed by Figure 1.4 (c) and Figure 1.4 (d) demonstrating the dependence of $v_{g,z}$ on Γ_0 for the fixed values of ω_C and its dependence on ω_C for several fixed values of Γ_0. Such a tendency can be qualitatively explained as follows. Once the parameter Γ_0 increases, the lowest branch moves down in energy, see Figure 1.3(a) and (b). Since in the vicinity of $K, k_\rho \cong 0$ the dependence $\omega(K)$ for the lowest branch is convex, to conserve energy the wave packet should reduce its wave vector and group velocity $v_{g,z}$, (see EFCs in Figure 1.3(c)). It is important to mention that this conclusion is only correct in a specific frequency range, namely, for $\omega_C < \omega_0$, where ω_0 is the frequency of the saddle point in the dispersion curve.

1.1.3 Quantum description of excitons and MC polaritons

As it was shown in the previous section, it is possible to describe the exciton and polariton modes in QW structures semi-classically, by solving Maxwell equations together with a relation between the electric field and displacement field. So each layer except the embedded QW can be modeled by frequency independent dielectric constant, while in QW the excitonic contribution depends on frequency. The transfer matrix method helps to solve Maxwell equations effectively and finally one can obtain the exciton and exciton-polariton dispersions as it is demonstrated in Figure 1.3(a) and (b). However, this description becomes insufficient for the effects, related to the Bose-Einstein condensation of these quasi-particles which is essentially a quantum effect. The quantum description of excitons, and MC polaritons, introduced in Refs. [4, 11], is discussed below. For simplicity the spin dependence is not taken into account.

1.1.3.1 Excitons

The Hamiltonian of an interacting electronic system reads:

$$\hat{H} = \int \hat{\Psi}^\dagger(\boldsymbol{r})\hat{H}_0(\boldsymbol{r})\hat{\Psi}^\dagger(\boldsymbol{r})d\boldsymbol{r} + \frac{1}{2}\int d\boldsymbol{r}d\boldsymbol{r}'\hat{\Psi}^\dagger(\boldsymbol{r})\hat{\Psi}^\dagger(\boldsymbol{r}')\,\hat{V}(\boldsymbol{r}-\boldsymbol{r}')\hat{\Psi}(\mathbf{r})\hat{\Psi}(\mathbf{r}'), \quad (1.22)$$

where $H_0(\boldsymbol{r})$ is the single electron Hamiltonian and $V(\boldsymbol{r}-\boldsymbol{r}')$ is the Coulomb interaction in the solid. The Fermi field operator can be expanded in the eigenfunctions of H_0 i.e.

$$\widehat{H}_0\psi_{k,j}(\boldsymbol{r}) = E^0_{k,j}\psi_{k,j}(\boldsymbol{r}), \tag{1.23}$$

where the single electron wave function can be expanded in terms of Bloch waves, and respectively the field operator can be expressed as

$$\widehat{\Psi}(\mathbf{r}) = \frac{1}{\sqrt{N}}\sum_{\boldsymbol{k};j=c,v} \hat{a}_{\boldsymbol{k}j}\, u_{\boldsymbol{k},j}(\boldsymbol{r})e^{i\boldsymbol{kr}}. \tag{1.24}$$

Here $u_{\boldsymbol{k},j}(\boldsymbol{r})$ is a Bloch wave-function, N is a number of unit cells in the lattice, $j = c, v$ denotes the conduction and valence bands and $\hat{a}_{\boldsymbol{k}j}$ and $\hat{a}^{\dagger}_{\boldsymbol{k}j}$ are the fermionic annihilation and creation operators with commutation relations: $\{\hat{a}_{\boldsymbol{k}j}, \hat{a}_{\boldsymbol{l}j}\} = 0, \{\hat{a}_{\boldsymbol{k}j}, \hat{a}^{\dagger}_{\boldsymbol{k}j}\} = \delta_{i,j}\delta_{\boldsymbol{k},\boldsymbol{l}}$. One can substitute the expression for the field operator into the Hamiltonian and simultaneously introduce creation and annihilation operators for the holes in the valence band:

$$\hat{a}_{k,v} = \hat{b}^{\dagger}_{-k,c}, \tag{1.25}$$

which means that the annihilation of a single electron with momentum $\boldsymbol{k}$ in the valence band is equivalent to the creation of a single hole with momentum $-\boldsymbol{k}$. The Hamiltonian, that neglects all number non-conserving terms, reads:

$$\begin{aligned}\widehat{H} = &\sum_{\boldsymbol{k}} E_e(\boldsymbol{k})\hat{a}^{\dagger}_{\boldsymbol{k}}\hat{a}_{\boldsymbol{k}} + \sum_{\boldsymbol{k}} E_h(\boldsymbol{k})\hat{b}^{\dagger}_{\boldsymbol{k}}\hat{b}_{\boldsymbol{k}} + \frac{1}{2}\sum_{\boldsymbol{k_1},\boldsymbol{k_2},\boldsymbol{k_3},\boldsymbol{k_4}} V^{c,\ c,\ c,\ c}_{\boldsymbol{k_1},\boldsymbol{k_2},\boldsymbol{k_3},\boldsymbol{k_4}}\, \hat{a}^{\dagger}_{\boldsymbol{k_1}c}\hat{a}^{\dagger}_{\boldsymbol{k_2}c}\hat{a}_{\boldsymbol{k_3}c}\hat{a}_{\boldsymbol{k_4}c} \\ &+ \frac{1}{2}\sum_{\boldsymbol{k_1},\boldsymbol{k_2},\boldsymbol{k_3},\boldsymbol{k_4}} V^{v,\ v,\ v,\ v}_{-\boldsymbol{k_1},-\boldsymbol{k_2},-\boldsymbol{k_3},-\boldsymbol{k_4}}\, \hat{b}^{\dagger}_{\boldsymbol{k_1}c}\hat{b}^{\dagger}_{\boldsymbol{k_2}c}\hat{b}_{\boldsymbol{k_3}c}\hat{b}_{\boldsymbol{k_4}c} \\ &- \sum_{\boldsymbol{k_1},\boldsymbol{k_2},\boldsymbol{k_3},\boldsymbol{k_4}} \left(V^{c,\ v,\ v,\ c}_{\boldsymbol{k_1},\boldsymbol{k_3},\boldsymbol{k_2},\boldsymbol{k_4}} - V^{c,\ v,\ c,\ v}_{\boldsymbol{k_1},\boldsymbol{k_3},\boldsymbol{k_4},\boldsymbol{k_2}}\right)\hat{a}^{\dagger}_{\boldsymbol{k_1}c}\hat{b}^{\dagger}_{\boldsymbol{k_2}c}\hat{b}_{\boldsymbol{k_3}c}\hat{a}_{\boldsymbol{k_4}c},\end{aligned} \tag{1.26}$$

where $V^{i,\ j,\ l,\ m}_{\boldsymbol{k_1},\boldsymbol{k_2},\boldsymbol{k_3},\boldsymbol{k_4}} = \langle \boldsymbol{k_1}i, \boldsymbol{k_2}j|\hat{V}|\boldsymbol{k_3}l, \boldsymbol{k_4}m\rangle$, E_e and E_h are the kinetic energies of an electron and a hole in the effective mass approximation introduced by the Eq.(1.5) with the band gap energy $E_S(0) = E_g$. The Schrödinger equation for the electron-hole pair reads: $\widehat{H}\varphi = E\varphi$ with

$$\varphi = \sum_{\boldsymbol{k},\boldsymbol{k}'} A_{\boldsymbol{k},\boldsymbol{k}'}\, \hat{a}^{\dagger}_{\boldsymbol{k}}\hat{b}^{\dagger}_{\boldsymbol{k}'}|0\rangle, \tag{1.27}$$

where $|0\rangle$ is a quasi-vacuum state i.e. an empty conduction band and full valence band. Direct substitution of the wave function leads to the following equation:

$$(E_e(\boldsymbol{k}) + E_h(\boldsymbol{k}') - E)A_{\boldsymbol{k},\boldsymbol{k}'} - \sum_{\boldsymbol{k},\boldsymbol{k}'}(V^{c,v,v,c}_{\boldsymbol{k},-\boldsymbol{l}',-\boldsymbol{k}',\boldsymbol{l}} - V^{c,v,c,v,c}_{\boldsymbol{k},-\boldsymbol{l}',\boldsymbol{l},-\boldsymbol{k}'})\, A_{\boldsymbol{k},\boldsymbol{k}'} = 0. \tag{1.28}$$

Bloch wave functions in Eq.(1.23) are orthogonal. If both the Coulomb potential and plane wave factors are slowly varying functions and practically do not change along the unit cell, which is valid for weakly bound pairs with small relative motion momenta and large separation between electrons and holes, one can neglect the exchange integral and simplify the Coulomb interaction:

$$V^{c,v,v,c}_{\boldsymbol{k},-\boldsymbol{l}',-\boldsymbol{k}',\boldsymbol{l}} = \frac{1}{N_{cell}^2}\int d\boldsymbol{r}d\boldsymbol{r}'\frac{e^2}{\varepsilon|\boldsymbol{r}-\boldsymbol{r}'|}e^{i(\boldsymbol{l}-\boldsymbol{k})\cdot\boldsymbol{r}+i(\boldsymbol{l}'-\boldsymbol{k}')\cdot\boldsymbol{r}'}, \tag{1.29}$$

Thus taking the Fourier transform of Eq.(1.28) with the simplified interaction potential one can obtain the Wannier equation for the exciton [2]:

$$\widehat{H}_{ex}\Phi(\boldsymbol{r_e},\boldsymbol{r_h}) = E\Phi(\boldsymbol{r_e},\boldsymbol{r_h}) \tag{1.30}$$

$$\Phi(\boldsymbol{r_e},\boldsymbol{r_h}) = \sum_{\boldsymbol{k},\boldsymbol{k}'} A_{\boldsymbol{k},\boldsymbol{k}'}\, e^{i\boldsymbol{k}\cdot\boldsymbol{r}_e+i\boldsymbol{k}'\cdot\boldsymbol{r}_h} = \frac{1}{\sqrt{V}}f_n(\boldsymbol{r})\cdot e^{i\boldsymbol{K}\cdot\boldsymbol{R}} \tag{1.31}$$

with $\Phi(\boldsymbol{r_e},\boldsymbol{r_h})$ being the two-particle wave-function, expressed in terms of the centre of mass and relative motion coordinates, that coincides with expression (1.3). $\widehat{H}_{ex}$ coincides with the Hamiltonian in Eq.(1.8) but with the only difference, that no confined potential is taken into account.

Eq.(1.27) with substitution of expression (1.31) allows introducing the new exciton creation and annihilation operators:

$$\hat{e}^{\dagger}_{\boldsymbol{K},n} = \sum_{\boldsymbol{k},\boldsymbol{k}'} \delta_{\boldsymbol{K},\boldsymbol{k}+\boldsymbol{k}'} f_n(\boldsymbol{l})\, \hat{a}^{\dagger}_{\boldsymbol{k}}\hat{b}^{\dagger}_{\boldsymbol{k}'}, \tag{1.32}$$

where $f_n(\boldsymbol{l})$ is a Fourier transform of $f_n(\boldsymbol{r})$ and $\boldsymbol{l} = (m_h\boldsymbol{k} - m_e\boldsymbol{k}')/(m_e + m_h)$. The commutation relations for the exciton operators are:

$$\left[\hat{e}^{\dagger}_{\boldsymbol{K}',n'}, \hat{e}^{\dagger}_{\boldsymbol{K},n}\right] = 0, \tag{1.33}$$

$$\left[\hat{e}_{\boldsymbol{K}',n'}, \hat{e}_{\boldsymbol{K},n,}\right] = 0, \tag{1.34}$$

$$\left[\hat{e}_{\boldsymbol{K}',n'}, \hat{e}^{\dagger}_{\boldsymbol{K},n}\right] = \delta_{KK'}\delta_{nn'} - O\left(n_{ex}a_B^d\right), \tag{1.35}$$

with d being the dimensionality of the considered system. The latter shows that excitons can be considered as bosons only in the low-density limit. In 2D case this means $n_{ex} \ll 1/a_B^2$.

1.1.3.2 Microcavity polaritons

The excitons in QWs can be created by optical excitation. The coupling of the exciton to a photon mode is normally weak which means the high probability for the exciton to emit a photon into the free space. However, if the QW, where the exciton is created, is embedded into a MC, the cavity mode can be tuned to be in resonance with the excitonic transition. Then it is possible to achieve strong coupling regime between the exciton and photon modes resulting in *exciton-polariton modes*. The quantum description starts with the Hamiltonian in the rotating wave approximation:

$$H = \sum_{\boldsymbol{k}_\parallel} E_X(\boldsymbol{k}_\parallel)\, \hat{a}^\dagger_{\boldsymbol{k}_\parallel} \hat{a}_{\boldsymbol{k}_\parallel} + \sum_{\boldsymbol{k}_\parallel} E_C(\boldsymbol{k}_\parallel)\, \hat{b}^\dagger_{\boldsymbol{k}_\parallel} \hat{b}_{\boldsymbol{k}_\parallel} + \sum_{\boldsymbol{k}_\parallel} \hbar\Omega\,(\boldsymbol{k}_\parallel) \left(\hat{a}^\dagger_{\boldsymbol{k}_\parallel} \hat{b}_{\boldsymbol{k}_\parallel} + \hat{a}_{\boldsymbol{k}_\parallel} \hat{b}^\dagger_{\boldsymbol{k}_\parallel}\right), \quad (1.36)$$

where $\hat{a}_{\boldsymbol{k}_\parallel}$ and $\hat{b}_{\boldsymbol{k}_\parallel}$ are the exciton and photon annihilation operators, $E_X(\boldsymbol{k}_\parallel)$ is the energy of the exciton transition, $E_C(k_\parallel)$ is the energy of the cavity mode, and Ω is the coupling strength between the exciton and the cavity photon. The criterion of the strong coupling regime is that the exciton-photon coupling must dominate over the exciton and photon decay rates i.e. $\Omega \gg \gamma_{ex}, \gamma_{ph}$, where Ω is the coupling strength and ${\gamma_{ex}}^{-1}$ and ${\gamma_{ph}}^{-1}$ are the exciton and photon lifetimes. In this limit, the Hamiltonian (1.36) can be diagonalized with the Hopfield transformation:

$$\hat{P}_{\boldsymbol{k}_\parallel} = X(\boldsymbol{k}_\parallel)\hat{a}_{\boldsymbol{k}_\parallel} + C(\boldsymbol{k}_\parallel)\hat{b}_{\boldsymbol{k}_\parallel}, \quad (1.37)$$

$$\hat{Q}_{\boldsymbol{k}_\parallel} = -C(\boldsymbol{k}_\parallel)\hat{a}_{\boldsymbol{k}_\parallel} + X(\boldsymbol{k}_\parallel)\hat{b}_{\boldsymbol{k}_\parallel}, \quad (1.38)$$

where

$$\left|X(\boldsymbol{k}_\parallel)\right|^2 = \frac{1}{2}\left(1 + \frac{\Delta(\boldsymbol{k}_\parallel)}{\sqrt{4\Omega^2 + \Delta^2(\boldsymbol{k}_\parallel)}}\right), \quad (1.39)$$

$$\left|\mathrm{C}(\boldsymbol{k}_\parallel)\right|^2 = \frac{1}{2}\left(1 - \frac{\Delta(\boldsymbol{k}_\parallel)}{\sqrt{4\Omega^2 + \Delta^2(\boldsymbol{k}_\parallel)}}\right), \quad (1.40)$$

with cavity detuning $\Delta(\boldsymbol{k}_\parallel) = E_C(\boldsymbol{k}_\parallel) - E_X(\boldsymbol{k}_\parallel)$. $X(\boldsymbol{k}_\parallel)$ and $C(\boldsymbol{k}_\parallel)$ are the exciton and the cavity photon Hopfield coefficients which can be understood as the fractions of exciton and photon in the polariton. Finally, the polariton Hamiltonian reads:

$$H = \sum_{\boldsymbol{k}_\parallel} E_{LP}(\boldsymbol{k}_\parallel)\, \hat{P}^\dagger_{\boldsymbol{k}_\parallel} \hat{P}_{\boldsymbol{k}_\parallel} + \sum_{\boldsymbol{k}_\parallel} E_{UP}(\boldsymbol{k}_\parallel) \hat{Q}^\dagger_{\boldsymbol{k}_\parallel} \hat{Q}_{\boldsymbol{k}_\parallel}, \quad (1.41)$$

with energies of new modes given as:

$$E_{UP,LP}(\boldsymbol{k}_\parallel) = \frac{1}{2}\left[E_X(\boldsymbol{k}_\parallel) + E_C(\boldsymbol{k}_\parallel) \pm \sqrt{\Delta(\boldsymbol{k}_\parallel)^2 + 4\Omega^2}\right]. \quad (1.42)$$

Figure 1.5 shows the polariton dispersion for three different detunings.

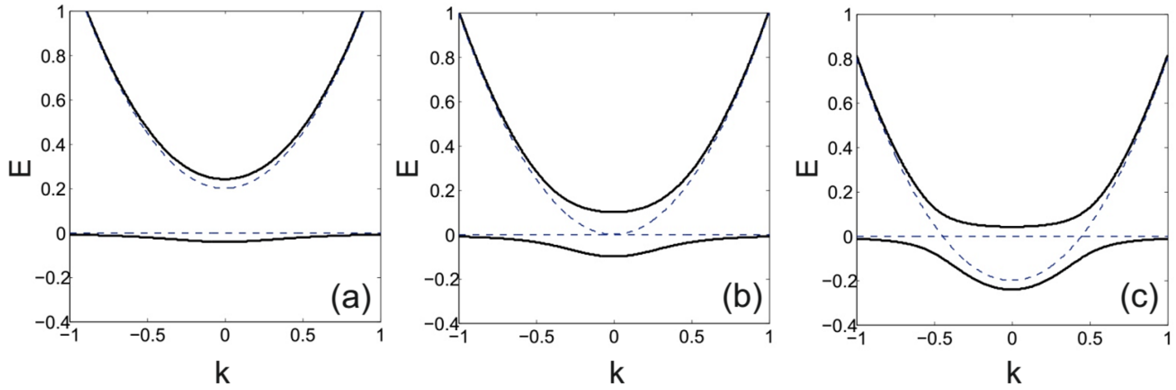

Figure 1.5: Polariton mode dispersion (black lines) plotted in arbitrary units for the different values of detuning: (a) $\Delta(\boldsymbol{k}_{\parallel}) = 0.2$ (b) $\Delta(\boldsymbol{k}_{\parallel}) = 0$, (c) $\Delta(\boldsymbol{k}_{\parallel}) = -0.2$. Dashed lines illustrate the photon and bare exciton modes.

The two polariton branches can be experimentally observed as two resonances in the reflection or transmission spectra. An example of such an experiment is given in Chapters 2 and 4.

One of the first observations of strong coupling regime in semiconductor microcavities was done by Weisbuch *et al*. [12] in 1992 at T=20 K and then shown at room temperatures by Houdré *et al*. in Ref. [13, 14]. The bosonic nature of exciton polaritons was demonstrated in the experiment, where the parametric amplification of the polaritonic emission in the state $\boldsymbol{k}_{\parallel} = 0$ was shown [15]. In this experiment, the pump beam created a population on the lower polariton branch in the inflection point of dispersion with $\boldsymbol{k}_{\parallel} = \boldsymbol{k_p}$. From this state polaritons could coherently scatter into the final states: $\boldsymbol{k}_{\parallel} = 0$ and $\boldsymbol{k}_{\parallel} = 2\boldsymbol{k_p}$. This scattering process conserves momentum and energy. The probe beam intensity at $\boldsymbol{k}_{\parallel} = 0$ was found to be amplified due to the stimulated scattering into this state, and the emerging probe power was found to be linear with the injected probe power.

1.2 Bose – Einstein Condensation of Polaritons

The phenomenon of Bose-Einstein condensation (BEC) is known since 1925 when Einstein predicted that the ability of bosons to accumulate unlimitedly in a degenerate state can lead to a new phase transition. The experimental realization of the atomic Bose-Einstein condensation was demonstrated in rubidium atomic gas in 1995 at a temperature of 170 nK [16] and later in sodium atoms at 2μK [17]. For these experiments Eric Cornell, Wolfgang Ketterle and Carl Wieman were awarded with the Nobel Prize in Physics in 2001. In this subsection the general theory of BEC is presented and properties of polaritonic BEC are discussed.

1.2.1 General description of Bose-Einstein condensation

The distribution of non-interacting bosons staying in the thermal equilibrium at a finite temperature *T* reads:

$$f(E) = f(k, T, \mu) = \frac{1}{e^{(E(k)-\mu)/k_B T} - 1}, \tag{1.43}$$

where μ is the chemical potential and k_B is the Boltzmann constant, E generally depends on the wave vector and is given by the dispersion relation. At high temperatures as well as in the low density limit the quantum Bose distribution transforms into classical Boltzmann distribution.

At high temperatures the chemical potential is defined by the temperature. However, when μ reaches the energy of the ground state at some critical temperature T_C, the macroscopic number of particles begin to occupy the ground state, that can be understood as the condensate formation.

Figure 1.6(a) shows the distribution function plotted for different values of the chemical potential increasing from -1.5$k_B T$ to -0.0001$k_B T$ (the graph is presented in semi-logarithmic plot) in the ideal 3D gas. The sharp nonlinear increase near $E = 0$ is observed when the value of the chemical potential approaches zero ($\mu \to 0^-$), while in semi-log scale the distribution remains linear (i.e. normal exponential dependence) when the chemical potential is of the order of $k_B T$. This increase at $E \to 0$ can be naively treated in a way that less energy is needed to add the particle to the ground state.

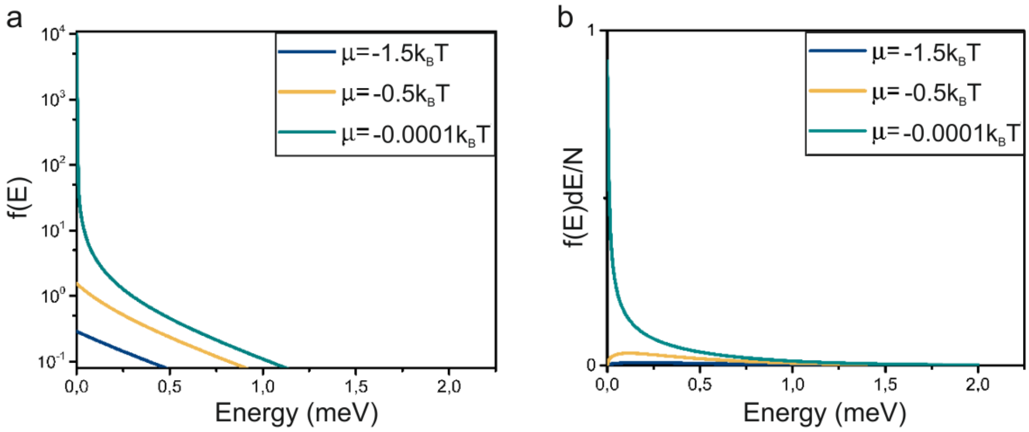

Figure 1.6: (a) The Bose – Einstein distribution function plotted for different values of chemical potential (b) the fraction of bosons, occupying different energy states in an ideal gas.

The value of the chemical potential is derived from the expression:

$$N(T, \mu) = \sum_k f(k, T, \mu), \tag{1.44}$$

where N is the fixed number of particles in the system. The value of chemical potential can be adjusted, so the probability for particles to occupy the ground state can be increased. Figure 1.6(b) shows the fraction of particles, populating the energy $E \sim E + dE$. At low chemical potentials and at finite temperatures the particles are mostly occupying states with non-zero energy, because the density of states decreases with energy, contrary to the distribution function. However, at high chemical potentials the probability to find a particle at zero energy drastically increases and the ground state population becomes dominant. This fact indicates the possibility of a phase transition.

In order to derive the critical temperature and the density of the phase transition in the 3D case one should first express the density of states for a free boson [18]:

$$g(E) = \frac{V}{4\pi^3}\left(\frac{2m}{\hbar^2}\right)^{3/2}\sqrt{E}. \tag{1.45}$$

Here V is the system volume and m is the mass of a boson. The total number of bosons in the system reads:

$$N(T,\mu) = N_0(T,\mu) + N_{ex}(T,\mu). \tag{1.46}$$

Here N_0 is the number of particles in the ground state and N_{ex} is the number of particles in all excited states. The Bose-Einstein condensation occurs when $\mu \to 0$, so that $N_0(T,\mu)$ is comparable with the total number of particles $N(T,\mu)$. The critical temperature can be calculated from the condition:

$$N_{ex}(T_c, \mu = 0) = N, \tag{1.47}$$

from which one can understand that the condensation is the saturation of excited states.

The critical density for the phase transition can be found as follows:

$$N_c = \int_0^\infty g(E)f(E)dE = \int_0^\infty \frac{g(E)}{e^{-E/k_BT} - 1}dE = N_{ex}(T_c, \mu = 0), \tag{1.48}$$

where $g(E)$ is the density of states given by Eq.(1.45) and $f(E)$ is the distribution function given by Eq.(1.43). The critical density can be found as follows:

$$N_c = \frac{V}{4\pi^2}\left(\frac{2mk_BT}{\hbar^2}\right)^{\frac{3}{2}}\Gamma\left(\frac{3}{2}\right)\zeta\left(\frac{3}{2}\right), \tag{1.49}$$

where $\Gamma(x)$ and $\zeta(x)$ are defined as:

$$\Gamma(x) = \int_0^\infty \xi^{x-1}e^{-\xi}\,d\xi, \tag{1.50}$$

$$\zeta(x) = \frac{1}{\Gamma(x)}\int_0^\infty \frac{\xi^{x-1}}{e^\xi - 1} d\xi. \tag{1.51}$$

In the 2D and 1D cases the integral (1.48) diverges because of the different energy dependence of the density of states. However, it is still possible to describe the condensation when the system is either finite sized or trapped in a confinement potential.

The detailed description of the BEC in confinement potentials is presented in Refs. [19, 18]. For the finite size systems of the lateral size L one can describe the BEC as follows. The particle density is given by:

$$N(T, L, \mu) = \frac{N_0}{L^2} + \frac{1}{L^2}\sum_{\boldsymbol{k}, k > \frac{2\pi}{L}} \frac{1}{exp\left(\frac{E(\boldsymbol{k}) - \mu}{k_B T}\right) - 1}, \tag{1.52}$$

where N_0 is the population of the ground state, $E(\boldsymbol{k})$ is the polariton kinetic energy, μ is the chemical potential, and k_B is the Boltzmann constant.

Defining N_c as the maximum number of particles that can be accommodated in all states but the ground state, one can write:

$$N_c(L, T) = \frac{1}{L^2}\sum_{\boldsymbol{k}, k > \frac{2\pi}{L}} \frac{1}{exp\left(\frac{E(\boldsymbol{k})}{k_B T}\right) - 1}. \tag{1.53}$$

Here μ is set to zero that allows to put bosons into the ground state without limitation, while the concentration of polaritons in the upper states is constant and equals to $N_c(L, T)$. The condensate density is thus equal to $N_0 = N - N_c$. The upper limit for N_c is assumed to be the Mott density, which is calculated by

$$N_{Mott} = \frac{A}{\pi a_B^2}, \tag{1.54}$$

where A is the normalization area of 1 cm^2 and a_B is the Bohr radius.

The phenomenon of BEC can be qualitatively understood as follows: if the thermal de Broglie wavelength is comparable with the distance between particles, the condensation occurs. Formally, in the 2D case it can be written as follows:

$$\lambda_{dB} = \left(\frac{2\pi\hbar^2}{mk_B T}\right)^{\frac{1}{2}} \approx n^{-\frac{1}{2}}. \tag{1.55}$$

Then the critical temperature may be estimated as:

$$T_C \approx \frac{2\pi n \hbar^2}{m k_B}. \tag{1.56}$$

This qualitative expression renders exciton-polaritons the best candidates for observation of BEC due to their extremely light mass.

In regard to the polariton condensation, it is instructive to introduce the difference between BEC and polariton lasing regime. The latter is the phenomenon of coherent emission from the macroscopically populated ground state. However, the macroscopic population is not enough to show BEC in the system. Polariton lasers are excited non-resonantly by generating an electron-hole cloud, from which excitons are formed. Excitons thermalize due to interactions with phonons and exciton-exciton scattering, settle along the lower polariton branch and then scatter into the ground state. At this point the particles do not have to be thermalized, which is essential for the formation of a true BEC. Experimentally, apart from thermal distribution of bosons the spontaneous vector polarization build-up and long-range spatial coherence are used as BEC criteria.

1.2.2 Experimental observations of polariton condensates and related phenomena

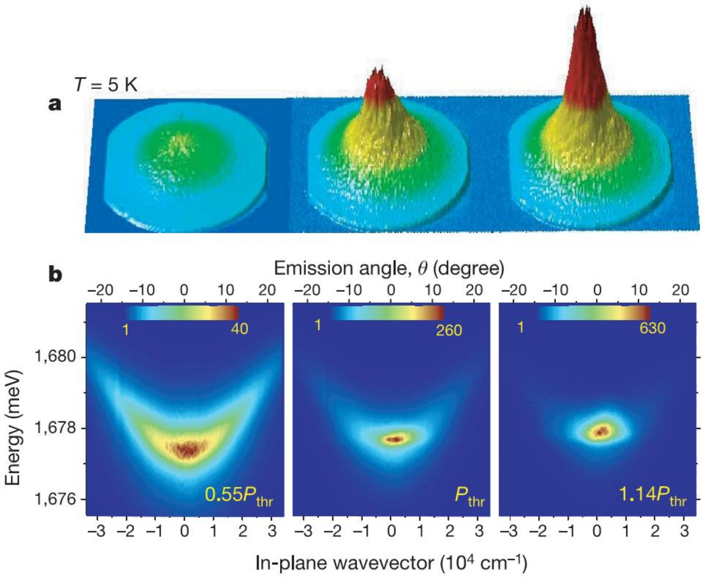

Figure 1.7: Far-field emission measured at 5 K below and above threshold, proving the formation of BEC. (a) With increasing excitation power, a sharp and intense peak is formed in the centre of the emission distribution,corresponding to the lowest momentum state $\boldsymbol{k}_{\parallel} = \boldsymbol{0}$. (b) Same data as in (a) but resolved in energy. Figure taken from Ref. [20].

The first experimental observation of the polariton condensation was shown by Deng and Yamamoto in GaAs multiple QW MC [21] and by Kaspzak et.al. in a MC based on a CdTe/CdMgTe QW [20], where the authors demonstrated the condensation into the ground state, the quantum coherence, indicated by the long-range spatial coherence, and sharpening of the temporal coherence of the emission. The experiment was carried out at T= 5 K. Observations of polariton condensation at room temperatures in different systems were demonstrated in Refs. [22, 23] . The evidence of non-equilibrium polariton condensates is shown in Ref. [24]. The coherent emission from macroscopic population of the ground state at room temperatures, the polariton lasing effect, is discussed in Refs. [25, 26, 27, 28].

1.2.3 Weakly interacting polariton condensates

Kinetics of a polariton gas may be described with a set of semiclassical Boltzmann rate equations, accounting for the bosonic nature of polaritons:

$$\frac{dn_{k,s}}{dt} = P_{k,s} + W_{k',s'}^{k,s} n_{k',s'}(1 + n_{k,s}) - W_{k,s}^{k',s'} n_{k,s}(1 + n_{k',s'}) - \gamma_{k,s} n_{k,s}. \qquad (1.57)$$

Here $n_{k,s}$ denotes the population of a state set by a wave vector k and a spin $s = \pm 1$, $P_{k,s}$ defines an external pumping rate related to binding of electrically or optically (non-resonantly) generated electron-hole pairs into excitonic particles, and $W_{k',s'}^{k,s}$ is the rate of spontaneous polariton scattering from the state k, s into the state k', s'. Eq. (1.57) is the most general form of the rate equations, which includes two generalized terms for the incoming polaritons and polaritons scattered away. It may account for various effects through the exact form of $W_{k',s'}^{k,s}$. In particular, it may describe emission and absorption of lattice phonons into and from the thermal phonon bath, or nonlinear polariton-polariton scattering processes. In the latter case $W_{k',s'}^{k,s}$ by itself depends on the populations of scatterers $n_{k,s}$.

As discussed above, although the formation of a true BEC is forbidden in the case of low dimensionality $d < 3$, a macroscopically populated state of a finite size can appear either in a confining potential, which removes the divergence in the expression for the critical density due to discreteness of the spectrum, or in the more experimentally relevant case of a finite size optical pumping spot. Depending on the relation between the characteristic rates of thermalization and decay, the steady state of a macroscopically populated polariton quantum state, or the polariton condensate, may follow either the behaviour of a Bose-Einstein condensate in the limit of fast thermalization, or the physics of polariton lasers in the opposite, completely non-equilibrium limit. The absence of a defined transition between the two limiting cases implies a crossover between polariton lasing and polariton BECs.

In both limiting cases, the formation of an interacting polariton condensate, typically for any second order phase transition, is related to the emergence of an order parameter, which has the meaning of the condensate wave function Ψ. If the thermalisation rate of a polariton gas is faster than the characteristic rate of polariton decay, typically given by the rate of photon escape from the cavity and the Hopfield coefficient, then the dissipative and nonequilibrium nature of the condensate is not important and its coherent evolution is given by the Gross-Pitaevskii equation (GPE):

$$\mathrm{i}\hbar\frac{\partial\Psi}{\partial t}=\left[-\frac{\hbar^2\nabla^2}{2m}+U(\boldsymbol{r},t)+\frac{\alpha}{2}|\Psi|^2\right]\Psi, \tag{1.58}$$

which accounts for contact polariton-polariton interactions, stemming from electron and hole exchange processes, and an external potential $U(\boldsymbol{r},t)$. The spinor version of GPE is applied when polarization effects are of importance:

$$\mathrm{i}\hbar\frac{\partial\Psi_\pm}{\partial t}=\left[-\frac{\hbar^2\nabla^2}{2m}+U_\pm(\boldsymbol{r},t)+\frac{\alpha_1}{2}\left|\Psi_\pm\right|^2+\frac{\alpha_2}{2}|\Psi_\mp|^2\right]\Psi_\pm+\beta\left(\frac{\partial}{\partial x}\pm i\frac{\partial}{\partial y}\right)^2\Psi_\mp. \tag{1.59}$$

Here the universal interaction nonlinearity constant α is replaced with a pair of interaction parameters $\alpha_{1,2}$, accounting for the anisotropy of polariton Coulomb interactions. The electron and hole exchange processes, which provide the major contribution to the polariton repulsion, are only allowed in the singlet configuration of polariton-polariton scattering, where the two quasi-particles are in the same spin state. On the contrary, in the triplet configurations, polaritons weakly attract due to second-order processes with dark excitons of spin ± 2 being the intermediate states [29]. The last term in the spinor GPE accounts for the TE-TM splitting of the planar cavity mode, which is responsible for the optical spin Hall effect [30].

To account for the dissipative nature of polariton condensates in steady states, which require either optical or electrical pumping, one has to supplement the GPE with non-Hermitian gain and loss terms:

$$\mathrm{i}\hbar\frac{\partial\Psi}{\partial t}=\left[-\frac{\hbar^2\nabla^2}{2m}+U(\boldsymbol{r},t)+\frac{\alpha}{2}|\Psi|^2+\frac{\alpha_R}{2}n+\frac{i\hbar}{2}(gn-\gamma)\right]\Psi. \tag{1.60}$$

Here both the gain term gn and the potential term $\alpha_R n/2$ are linear in the excitonic reservoir density n, and γ is the rate of polariton decay, which is typically defined by the rate of photon escape from the cavity. The classical excitonic reservoir, which typically stays in the vicinity of the inflection point of lower polariton dispersion branch because of the bottleneck effect [31], can in turn be described by a single semiclassical Boltzmann rate equation on the total reservoir density n:

$$\frac{\partial n}{\partial t}=P-\left[g|\Psi|^2+\Gamma\right]n\ +\ D\nabla^2 n. \tag{1.61}$$

Here P is the rate exciton pumping into the reservoir, Γ is the characteristic rate of exciton decay at the inflection point of the dispersion, and D is the rate of exciton diffusion in the reservoir.

1.2.4 Bogoliubov excitations of polariton condensates.

GPE is a classical field equation, as the wave function Ψ is the mean value of the polariton annihilation operator $a^\dagger(\boldsymbol{r})$ and has the physical meaning of the classical electric field value. It is therefore valid in the case of macroscopic occupation number of the condensate $N \gg 1$.

The elementary excitations of the condensate are related to the small fluctuations $\delta\Psi$ of the wave function. Since the nature of the fluctuations is quantum, they are described with the quantized form of GPE with the Hamiltonian, having the following form in the momentum space:

$$H = \sum_{\boldsymbol{p}} E_{\boldsymbol{p}}^0 \, \hat{a}_{\boldsymbol{p}}^\dagger \hat{a}_{\boldsymbol{p}} + \frac{\alpha}{2} \sum_{\boldsymbol{p},\boldsymbol{p}',\boldsymbol{q}} \hat{a}_{\boldsymbol{p}+\boldsymbol{q}}^\dagger \hat{a}_{\boldsymbol{p}'-\boldsymbol{q}}^\dagger \, \hat{a}_{\boldsymbol{p}} \hat{a}_{\boldsymbol{p}'}, \qquad (1.62)$$

where $E_p^0 = p^2/2m$ is the kinetic energy, or the single particle spectrum. The quantized condensate wave function is then expressed as $\hat{\Psi} = \Psi + \delta\hat{\Psi}$, where the fluctuation part is small compared to the classical one and conserves the total occupation number of the condensate N. Taking into account that both the ground state creation and anihilation operators may be replaced with their mean values $\sqrt{N}$, and keeping the second order in the perturbations, the interaction Hamiltonian may be rewritten:

$$H = \frac{\alpha N^2}{2} + \sum_{\boldsymbol{p} \neq 0} \left(E_{\boldsymbol{p}}^0 + \alpha N\right) \hat{a}_{\boldsymbol{p}}^\dagger \hat{a}_{\boldsymbol{p}} + \frac{\alpha N}{2} \sum_{\boldsymbol{p} \neq 0} \left(\hat{a}_{\boldsymbol{p}}^\dagger \hat{a}_{-\boldsymbol{p}}^\dagger + \hat{a}_{\boldsymbol{p}} \hat{a}_{-\boldsymbol{p}}\right). \qquad (1.63)$$

It may be diagonalized with the Bogoliubov transformation [32], introducing a set of new annihilation operators:

$$\hat{\alpha}_{\boldsymbol{p}} = u_{\boldsymbol{p}} \hat{a}_{\boldsymbol{p}} + v_{\boldsymbol{p}} \hat{a}_{-\boldsymbol{p}}^\dagger, \qquad \hat{\beta}_{\boldsymbol{p}} = u_{\boldsymbol{p}} \hat{a}_{-\boldsymbol{p}} + v_{\boldsymbol{p}} \hat{a}_{\boldsymbol{p}}^\dagger. \qquad (1.64)$$

In the new notation the interaction Hamiltonian reads:

$$H = \frac{\alpha N^2}{2} + \sum_{p \neq 0} E_p \, \hat{\alpha}_p^\dagger \hat{\alpha}_p - \frac{1}{2} \sum_{p \neq 0} \left(E_p^0 + \alpha N - E_p\right), \qquad (1.65)$$

where E_p^0 is the boson dispersion and the Bogoliubov excitation spectrum reads:

$$E_p = \sqrt{\left(E_p^0\right)^2 + 2\alpha N E_p^0}. \qquad (1.66)$$

In the low-energy limit the spectrum is linear with the group velocity $c = \sqrt{\alpha N/m}$. The Bogolon dispersion is plotted in Figure 1.8.

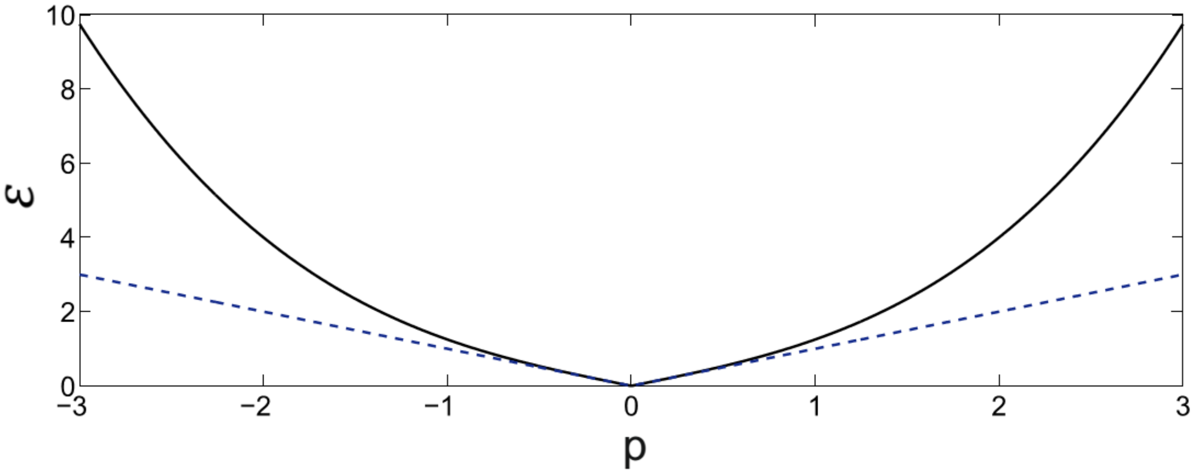

Figure 1.8: The spectrum of Bogoliubov excitations of an interacting condensate in dimensionless units $\epsilon = E_p/\alpha N$ and $\mathrm{p} = p/\sqrt{m\alpha N}$, linear dispersion with group velocity c is plotted with dashed line as a guide for the eye.

The excitations of a polariton laser, or a steady state of a coupled condensate-reservoir systems, characterized by a wave function Ψ_0 and a reservoir density n_0, are then obtained in a similar way with linearization of the coupled equations [33]:

$$\Psi = e^{-i\mu t}\Psi_0\left[1 + u_k e^{i(kr-\omega t)} + v_k^* e^{-i(kr-\omega t)}\right], \tag{1.67}$$

$$n = n_0\left[1 + w_k e^{i(kr-\omega t)} + w_k^* e^{-i(kr-\omega t)}\right]. \tag{1.68}$$

Excitations in this case are characterized by complex energy spectra. Positive imaginary parts of spectra correspond to exponentially growing fluctuations and their presence in a spectrum signifies a dynamical instability of the condensate-reservoir system. It appears in the case where the decay rates of the condensate and the reservoir are comparable and the reservoir strongly affects the condensate dynamics. Its physical origin is in polariton repulsion off the reservoir: a condensate density fluctuation, locally depleting the reservoir, creates a potential well, which in turn attracts the condensate and further increases its density. Spatially inhomogeneous condensates appearing from dynamical instabilities have been very recently observed in single shots observations of polariton condensation [34]. Typical spectra of a non-equilibrium condensate excitations in stable and unstable cases are shown in Figure 1.9. Thermally populated linear spectra of Bogoliubov condensate spectra were experimentally observed in Refs. [35, 36] (see Figure 1.10).

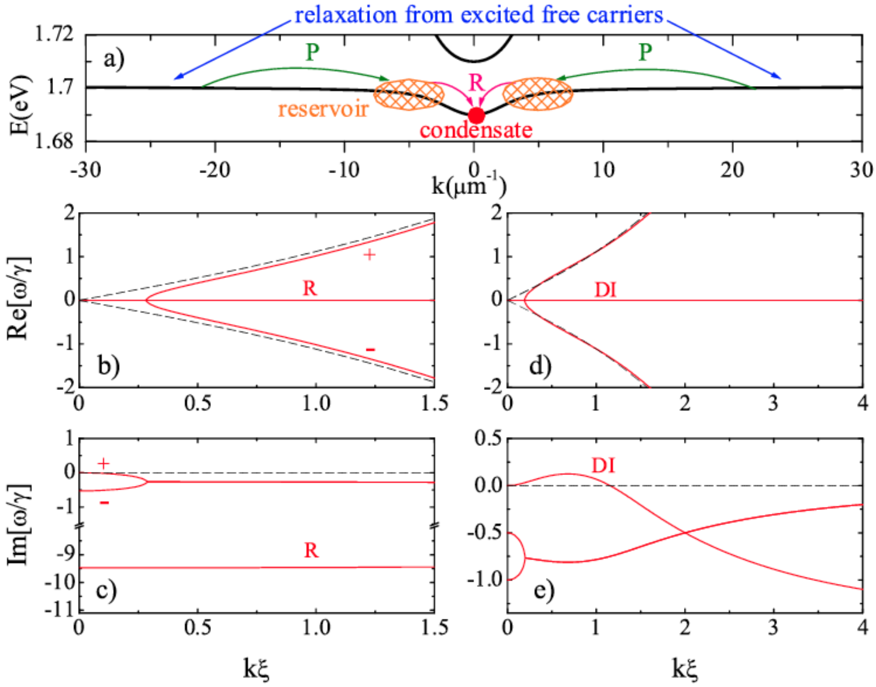

Figure 1.9: A scheme of nonequilibrium polariton condensation (a) and typical real (b,d) and corresponding imaginary (c,e) parts of the excitation spectra, obtained with two sets of parameters, corresponding to dynamically stable ($\Gamma \gg \gamma$) and unstable ($\Gamma \approx \gamma$) states of a nonequilibrium condensate. Reservoir diffusive excitation branch (R) transforms to the dynamical instability (DI) branch with the change of parameters. Figure taken from Ref. [33].

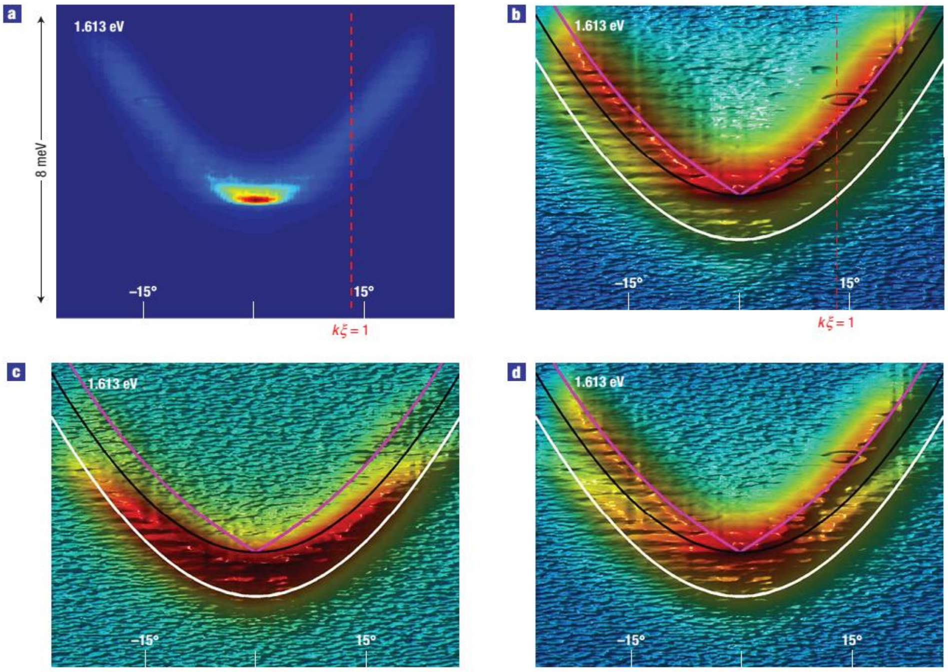

Figure 1.10: Polarization dependency of the excitation spectrum for an untrapped condensate system. (a) A linear plot of the intensity; (b)–(d) three-dimensional logarithmic plots of the intensity to magnify the excitation spectra. The theoretical curves represent the Bogoliubov excitation energy E_B (pink line), the quadratic dispersion relations E_{LP} (black line), which start from the condensate energy, and the non-interacting free-polariton dispersion relation E_{LP} (white line), which is experimentally determined by the data taken far below the threshold P= 0.001P_{th}. Figure and caption taken from Ref. [36].

1.3 Summary of the Thesis

In this Chapter I introduced the main properties of excitons and exciton-polaritons in semiconductors. The properties of these quasi-particles are further discussed in different systems.

The simulation of light propagation in layered structures described in Section 1.1.2.1 was demonstrated in Ref. [7], where the semiconductor layered crystal is shown to be suitable for controlling the group velocity and propagation direction of light as well as its spatial distribution.

The particular form of kinetic equations (1.57) is used to calculate the population of bosons on each level of the parabolic potential in order to reproduce experimental results and describe the relaxation processes in Chapter 2.

Bogoliubov excitations over the polariton condensate, demonstrated in section 1.2.4 are used in Chapter 3, where the light induced superconductivity is discussed.

Chapter 4 is devoted to the discussion of exciton and exciton-polariton properties in novel semiconductor structures, based on transition metal dichalcogenide monolayers. The variational approach was used to calculate binding energies of exciton and trions in monolayers of $MoSe_2$ in Section 4.3. The coupled oscillator approach was used to model the polariton dispersion which was first observed in WSe_2 based Tamm-plasmon structures in Section 4.4. Polariton condensation phase diagram was plotted for $MoSe_2$ monolayer with method discussed in Section 1.2.1.

Chapter 2: Bosonic Cascade Laser (BCL)

Recently the research of coherent light sources based on bosonic systems (known as bosers, or bosonic lasers) has seen a rapid boost [37]. In contrast to conventional lasers based on the phenomenon of stimulated emission, bosonic lasers are based on stimulated relaxation of bosons and on the formation of an exciton-polariton condensate [38]. This stimulated relaxation is triggered by the final state occupation of an energy level within a system, and serves as the principal tool for building up of a polariton population in a given energy state [39]. The coherence of boser radiation is the result of spontaneous emission of photons by the condensate after its occupation exceeds unity [20], making such a system ideal for a low-threshold lasing device. This Chapter builds upon the idea of the bosonic cascade laser (BCL) introduced by Liew *et al.* [40] that is capable of emitting terahertz (THz) radiation, a technologically underdeveloped range of the electromagnetic spectrum [41]. The BCL uses a cascade mechanism similar to that of the quantum cascade laser (QCL) [42, 43] in order to generate radiation. Unlike the QCL, which uses multiple adjacent QWs [44] as the cascade ladder, the BCL cascade [45] is formed by equidistant excitonic levels in a single parabolic quantum well (PQW) [46, 47]. Although intersubband polariton QCLs have been proposed [48], these rely upon the need for population inversion between adjacent subbands, analogous to the QCL. In the BCL, however, the amplification is due to the bosonic stimulation of radiative transitions between adjacent levels in a cascade. Both the QCL and a range of other proposed microcavity (MC) systems are capable of generating THz [49, 50], but the BCL uniquely offers increased amplification created by the final polariton state stimulation within the confines of a *single* PQW.

In this Chapter the main theory of the BCL and the results of the photoluminescence experiments in PQW are discussed. In these experiments the unusual pump-power dependencies of the photoluminescence (PL) in the PQW sample without the MC are shown, which is believed to be specifically due to the bosonic cascade relaxation mechanism. The relaxation dynamics of excitons in MCs with parabolic and rectangular QWs is investigated. The excitons are seen to relax in the PQW much faster than in a MC with a rectangular QW. Thus, accelerated relaxation in PQW might be an indication of stimulated relaxation in a bosonic cascade that is in agreement with the BCL model of Ref. [40]

2.1 Introduction

2.1.1 THz emitting sources:

The terahertz range of frequencies is considered to be from 100 GHz to 10 THz. This region of electromagnetic spectrum is very challenging in technical realisation and remains industrially underdeveloped in comparison to other wavelengths [51]. THz radiation importance stems from the possibilities of its applications: THz emission demonstrates ability to contrast against conductors and the emission is non-ionising, rotational and vibrational energies of many organic and inorganic molecules lie in the THz range, so it is highly essential in medicine and security. Currently THz devices are being developed for skin-cancer imaging, non-contact spectroscopy, detection of explosives, corrosion inspection, material characterisation, tomography and many others [51, 52]. In solid state physics THz radiation can provide additional information regarding carrier lifetime, carrier dynamics and densities, and electron ionisation in plasma. THz sources can be classified as broadband, narrowband, or incoherent thermal sources. Broadband radiation is generated in different materials by ultra-short laser pulses and is used for characterisation of electro-optic properties of materials; narrowband sources are crucial for high-resolution spectroscopy applications and will be of particular interest in this Chapter.

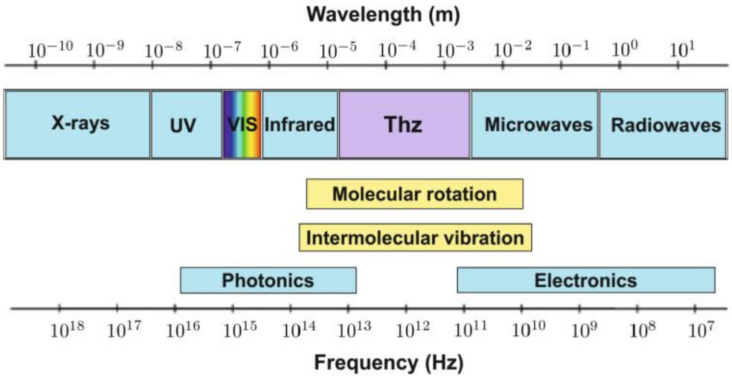

Figure 2.1: THz region that fills the gap between infrared and microwave region of electromagnetic spectrum.

2.1.2 Quantum cascade laser

In 1971 Kazarinov and Suris [44] proposed electromagnetic wave amplification by means of stimulated transitions of electrons between quantized subbands in two-dimensional QWs that could be obtained by growing atomically sharp semiconductor heterostructures.

As the transition energies are defined not by fixed material properties but rather by design parameters (particularly by layer thickness values of quantum wells), quantum cascade lasers can be designed for operating wavelengths ranging from a few microns to well above 10 µm, or even in the THz region. The first working QCL was demonstrated under cryogenic temperatures and in infrared frequencies with 4.3 µm wavelength by Faist *et al.* [42, 53] in 1994. The QCL implicates alternating levels of N asymmetric QWs that are stacked adjacently. THz emission occurs, when electrons, which are injected into the structure by an applied voltage, tunnel through the QWs in the active region of the structure, causing N identical photons to be emitted.

The laser emission is based on intersubband transitions in multiple QWs. During the cascade process each electron produces several tenth of photons, while it is passing through the structure. In 2001 this technology was realised in THz frequencies [54, 55]. A schematic illustration of the QCL is shown on Figure 2.2. Currently there are reports about room-temperature QCL THz generation, achieved by internal difference frequency generation [56]

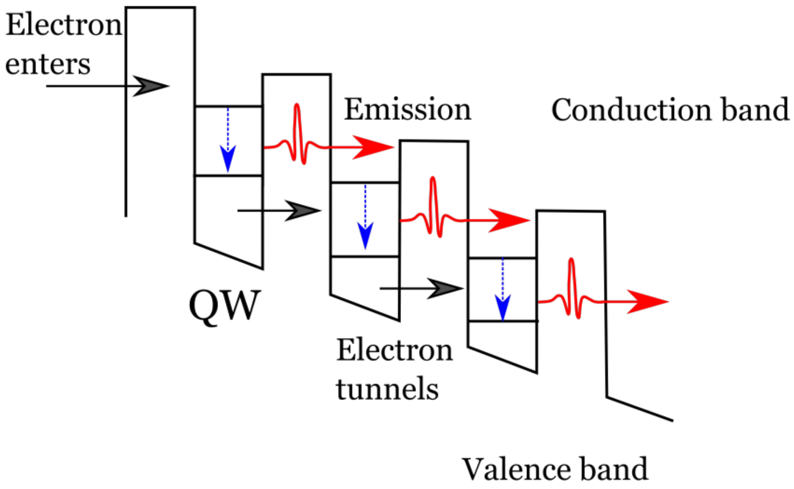

Figure 2.2: A schematic illustration of the QCL. In the first QW, an electron is injected resonantly into the upper energy subband, and can be stimulated to decay to a lower subband level, thereby emitting a photon. The lower-energy electron then tunnels to the next QW and causes another intersubband transition and the process continues along the ladder. Figure is taken from Ref. [57].

Despite all advantages of this type of laser the QCL operating regime has limitations: the electron thermalization rate should be higher than the rate of tunneling transition between QWs, so that the inversion population can occur. A technological drawback of QCLs is the inherently low total efficiency, because of the many possibilities that an electron in an upper state can lose its energy without emission of a photon. For example at high temperatures there is high probability that electron moves out of the quantum well without relaxation to the ground state. Currently the devices with efficiencies around 50% have been demonstrated only at cryogenic temperatures [58, 59]. Another problem is that the edge facet emission of most QCLs creates highly divergent output beams that are difficult to inject efficiently into small optics or fibres.

2.1.3 Vertical Cavity Surface emitting laser as a source of THz emission

The vertical cavity surface emitting laser (VCSEL) is a semiconductor laser diode that emits radiation in the direction perpendicular to the top surface, contrary to the edge-emitting lasers that emit from surfaces formed by cleaving the individual chip out of a wafer. First it was demonstrated in Tokyo by K. Iga *et al.* [60].

The laser resonator consists of two distributed Bragg reflectors with different reflectivity on the top and on the bottom and a QW in between. The structure can be integrated in a 2D array configuration; the low threshold currents enable high density arrays. VCSEL structures demonstrate high efficiency at low power and lower temperature sensitivity in comparison to edge-emitting laser diods. Figure 2.3 demonstrates the structural difference between conventional edge-emitting lasers and VCSEL.

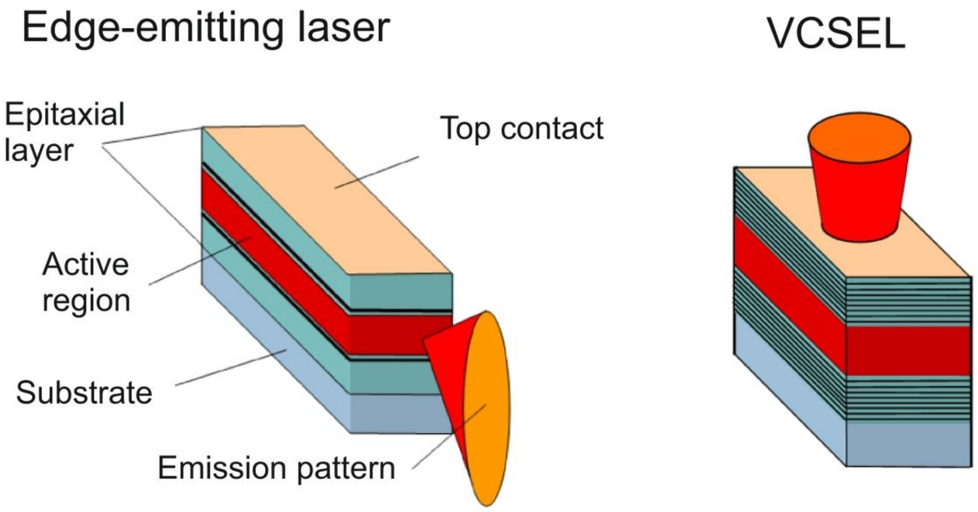

Figure 2.3: Schematic illustration of edge-emitting laser and VCSEL

The idea of THz VCSEL was proposed in Ref. [50] as an alternative to the model that uses the transition between the upper and the lower polariton branches in the polariton lasing regime. In this model THz emission is produced as a result of relaxation from the 2*p* exciton state to the lower polariton branch. The two-photon pumping is used to excite the 2p state [61, 62]. The direct transition from the 2p state with emission of a single photon is forbidden by the selection rules. However, the 2p exciton may relax radiatively to the lower polariton mode, that is composed of a 1s exciton and a cavity mode. This transition occurs with emission of a THz photon. This THz transition pumps the lowest energy polariton state that leads to polariton lasing effect that in turn stimulates THz transition due to macroscopic occupation of the lower polariton energy level. The VCSEL design allows operating with an optically allowed THz transition and it emits THz photons in vertical direction. Also, there is no need in a THz cavity. All these properties are significantly advantageous compared with the QCL or the model with transitions from the UPB to the LPB.

2.2 Theory of Bosonic Cascade Laser

2.2.1 The main proposal

The Bosonic Cascade Laser combines the advantages of QCLs and exciton-polariton lasers: the emission of multiple THz photons occurs with each injected electron; the threshold is very low and there is no need for THz cavity.

The first proposal of the BCL emitting in the THz range of frequencies was done by Tim Liew *et al.* in 2013 [40]. The exciton cascade is formed in a parabolic potential with equidistant excitonic levels. The most efficient transitions are allowed between the adjacent levels. The potential can be realized in different ways such as strain induced traps, optically induced traps and specially designed micropillars. One of the most promising designs is a parabolic QW embedded into a MC.

In the initial proposal the authors considered the weak coupling regime with the optical mode resonant with the m^{th} excitonic level for efficient pumping, while all other levels are supposed to be uncoupled from the cavity mode. This configuration benefits from the formation of the dark cascade with long radiative lifetimes. The radiation from the device is polarized in the direction normal to QW and propagates in the cavity plane in the wave guiding regime.

In order to determine the occupation numbers of the excitonic quantum confined states the following set of Boltzmann kinetic equations is used:

$$\frac{dN_m}{dt} = P - \frac{N_m}{\tau} - WN_m(N_{m-1} + 1) + W_1 N_{m-1}(N_m + 1), \tag{2.1}$$

$$\begin{aligned} \frac{dN_k}{dt} &= -\frac{N_k}{\tau} + W[N_{k+1}(N_k + 1) - N_k(N_{k-1+1})] + \\ &+ W_1[N_{k-1}(N_k + 1) - N_k(N_{k+1} + 1)], \ \forall\, 1 \le k \le m-1, \end{aligned} \tag{2.2}$$

$$\frac{dN_0}{dt} = -\frac{N_0}{\tau} + WN_1(N_0 + 1) - W_1 N_0(N_1 + 1), \tag{2.3}$$

where P is the initial pumping density, N_i is the occupation of i-th level, W and W_1 are the THz emission and absorption rates respectively, τ is the lifetime of cascade levels, which includes both radiative and non-radiative decay rates.

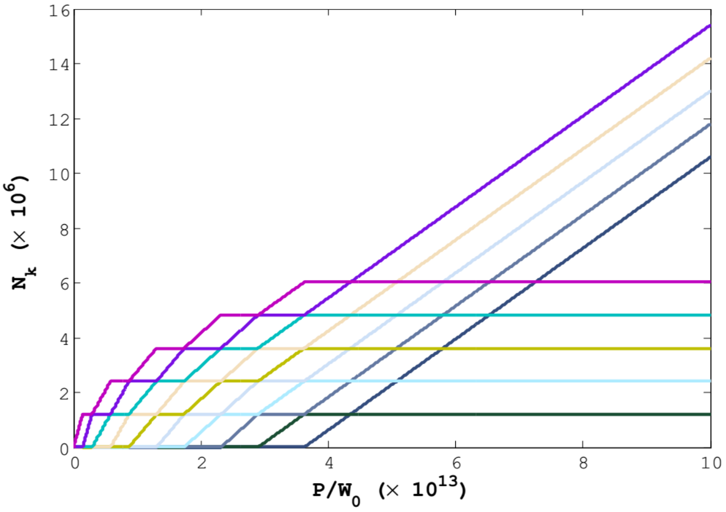

Figure 2.4: Dependence of the mode occupations in the absence of a THz cavity on pump intensity, calculated numerically from the kinetic equations (2.1)-(2.3).

Non-radiative lifetime includes losses due to phonon scattering to states with a non-zero in-plane wave vector. In the case where the THz cavity is presented, one more equation is added to the system:

$$\frac{dn_{THz}}{dt} = -\frac{n_{THz}}{\tau_{THz}} + W\sum_{1}^{m} N_k(N_{k-1}+1) - W_1\sum_{1}^{m} N_{k-1}(N_k+1), \qquad (2.4)$$

where n_{THz} is the THz mode occupation. In this model it is assumed that the matrix element of the THz transition is non-zero only for adjacent levels of the cascade and is uniform for all pairs of levels. Figure 2.4 represents the solution of the system of equations (2.1)-(2.3), in the case where $n_{THz} = 0$. In this model the energy levels are occupied by subsequent relaxations of excitons from the top.

2.2.2 The feasibility of THz transitions

To discuss the feasibility of THz transitions in the parabolic QW one should start from the two-particle Hamiltonian for an electron and a hole (Eq.(1.8) from section 1.1):

$$H = -\frac{\hbar^2}{2m_e}\nabla_e^2 - \frac{\hbar^2}{2m_h}\nabla_h^2 + V_e(z_e) + V_h(z_h) - \frac{e^2}{\varepsilon|\boldsymbol{r}_e - \boldsymbol{r}_h|}, \qquad (2.5)$$

This Hamiltonian consists of kinetic energy terms for an electron and a hole, potential terms and the Coulomb interaction. One can rewrite this Hamiltonian in terms of centre-of-mass and relative motion coordinates:

$$H = -\frac{\hbar^2}{2\mu}\nabla_{\boldsymbol{\rho}}^2 - \frac{\hbar^2}{2M}\nabla_{\boldsymbol{R}}^2 + V(z_e, z_h) - \frac{e^2}{\varepsilon\rho}, \qquad (2.6)$$

where $\mu = m_e m_h/(m_e + m_h)$, M =$m_e + m_h$, $\rho = |\boldsymbol{r}_e - \boldsymbol{r}_h|$. The QW potential is considered to have the form $(z_e, z_h) = C_e z_e^2 + C_h z_h^2$, which may be expressed in the coordinates of centre-of mass and relative motion:

$$V = (C_e + C_h)\mathcal{Z}^2 + \frac{(C_h m_e^2 + C_e m_h^2)z^2}{M^2} + \frac{2}{M}(C_h m_e - C_e m_h)\mathcal{Z}z. \qquad (2.7)$$

Here the last term mixes the internal and the centre-of mass degrees of freedom, provided that the pre-factor is not equal to zero. This term is extremely important because it allows the transitions between states, where the level index and orbital angular momentum are changed by 1 unit. Note that such transitions would be forbidden by selection rules in the absence of this term. From now on it is assumed that 2p state to 1s state transition energy is matched to the level spacing.

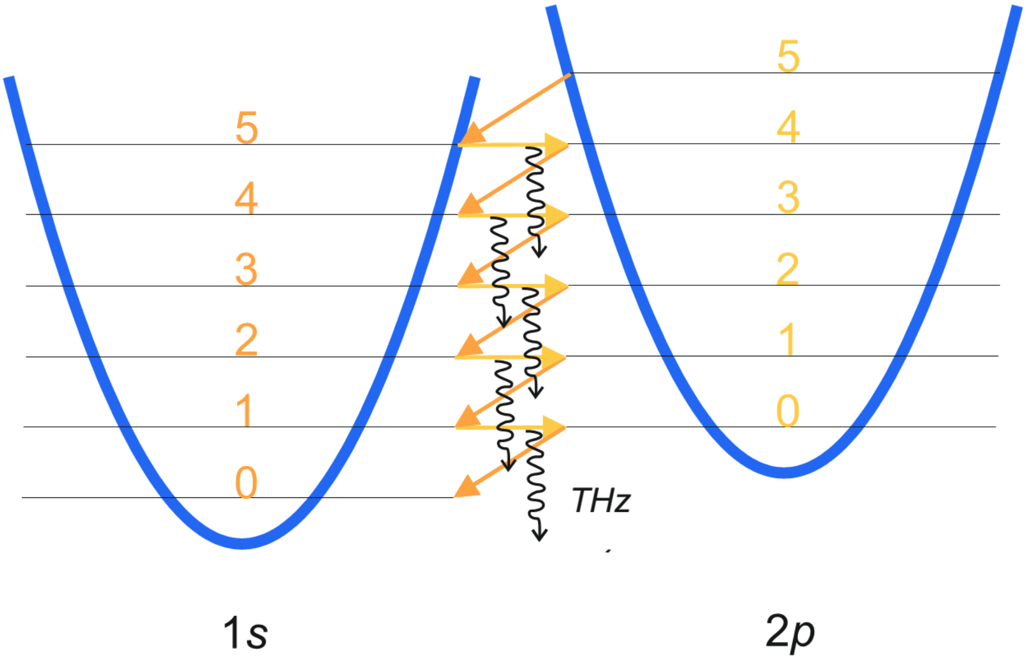

Figure 2.5: A schematic illustration of the cascade mechanism in parabolic potential: 2p exciton changes its angular momentum and transforms into 1s state with finite probability. After this process the radiative transition to the lower state occurs on a terahertz frequency.

Figure 2.5 qualitatively explains the relaxation process: the left parabolic ladder corresponds to energy levels of the 1s exciton and the right one corresponds to the energy levels of the 2p exciton. In general, there is always a probability that the 2p exciton transforms into the 1s exciton with the same energy (shown by orange arrow). At the same time the radiative transition from 2p to 1s state and back is allowed by selection rules. So, if the energy distance between levels is the same in both ladders, the relaxation can be described as follows: at first the exciton changes its orbital quantum number but stays at the same energy level and then decays to the lower state (yellow arrow in Figure 2.5) with emission of THz photon (black arrow). With the description above one can construct the wave function of the eigenstate of the cascade ladder, which is a mixture of 1s and 2p states (the notation of Ref. [40] is used):

$$|\pm, h\rangle = \frac{|1,0,0,h\rangle \pm |2,1,0,h-1\rangle}{\sqrt{2}}. \tag{2.8}$$

2.2.3 Steady state solutions and the comparison with the fermionic case

The analytical solutions of the system (2.1)-(2.3) can be obtained in the steady state regime in the absence of THz cavity, so $\frac{dN_k}{dt} = 0$ and $n_{THz} = 0$. Also, $N_i \gg 1$ and $W_0\tau \ll 1$. The steady state populations obtained from the rate equations read:

$$N_1 = \frac{N_0}{W_0\tau(N_0+1)} \approx \frac{1}{W_0\tau}, \tag{2.9}$$

$$N_k = \frac{N_{k-1}}{N_{k-1}+1}\left(\frac{1}{W_0\tau} + N_{k-2} + 1\right) \approx \frac{1}{W_0\tau} + N_{k-2}. \tag{2.10}$$

This leads to the general expression:

$$N_{2l} \approx N_0 + \frac{1}{W_0\tau}\ \forall\, 0 \le l \le \left\lfloor\frac{m}{2}\right\rfloor, \tag{2.11}$$

$$N_{2l-1} \approx N_0 + \frac{1}{W_0\tau}\ \forall\, 0 \le l \le \left\lceil\frac{m}{2}\right\rceil, \tag{2.12}$$

where $\lceil n\rceil$ denotes rounding up to the nearest integer and $\lfloor n\rfloor$ denotes rounding down. The populations of the pumped level and the ground level read:

$$N_m\left(\frac{1}{W_0\tau} + N_{m-1}\right) \approx \frac{P}{W}, \tag{2.13}$$

$$N_0 = \frac{2P\tau}{m+2} - \frac{m}{2W_0\tau}\quad \forall\, m \text{ even}, \tag{2.14}$$

$$N_0 = \frac{2P\tau}{m+1} - \frac{m+1}{2W_0\tau}\quad \forall\, m \text{ odd}. \tag{2.15}$$

From these equations the THz emission rate reads:

$$\frac{dn_{THz}}{dt} = W_0\sum_{1}^{m} N_k\,(N_{k-1}+1) = \frac{m^2+2m}{4\tau}\left(N_0 + \frac{2m-1}{6W_0\tau}\right)\quad \forall\, m \text{ even} \tag{2.16}$$

$$\frac{dn_{THz}}{dt} = \frac{(m+1)^2}{4\tau}N_0 + \frac{(m^2+1)(2m+3)}{24W_0\tau^2}\quad \forall\, m \text{ odd}. \tag{2.17}$$

In the case where $N_0 \gg 1$ the quantum efficiency can be expressed as:

$$\frac{1}{P}\frac{dn_{THz}}{dt} \to \left\lceil\frac{m}{2}\right\rceil > 1, m > 2.$$

The fermionic case is completely different from the bosonic cascade model, since the bosonic stimulation of the THz emission is not possible in the absence of a THz cavity. Rate equations (2.1)-(2.3) then are transformed into the following:

$$\frac{dN_m}{dt} = P - \frac{N_m}{\tau} - W_0 N_m, \tag{2.19}$$

$$\frac{dN_k}{dt} = -\frac{N_k}{\tau} + W_0(N_{k+1} - N_k) \quad \forall\, 2 \leq k \leq m-1, \tag{2.20}$$

$$\frac{dN_0}{dt} = -\frac{N_0}{\tau} + W_0 N_1. \tag{2.21}$$

In the steady state regime these equations yield:

$$N_0 = P\tau \left(\frac{W_0\tau}{1 + W_0\tau}\right)^m, \tag{2.22}$$

$$N_\mathrm{k} = \frac{P}{W_0}\left(\frac{W_0\tau}{1 + W_0\tau}\right)^{m-k+1} \forall\, 1 \leq k \leq m. \tag{2.23}$$

Figure 2.6 shows the dynamical population of energy levels, obtained by solving the kinetic equations (2.1)-(2.3) (bosonic case) and (2.19)-(2.21) (fermionic case). One can see that in the fermionic case all particles remain at the pumped level, while all other levels are nearly empty. This can be seen from the equation (2.23) where, if $W_0\tau \ll 1$, then $N_m \approx P\tau$. The THz emission rate is equal to $W_0 N_m$ and the quantum efficiency then is $W_0 N_m / P = \mathrm{W_0\tau} \ll 1$.

The description above was discussed in the case where the particle, which follows a sequence of transitions in the ladder, is an exciton. If the parabolic QW is embedded into a MC, so that the exciton levels are coupled with a cavity mode and the strong coupling regime is reached, the new polaritonic energy levels are not equidistant, so to create a polariton cascade laser one should alter the profile of the QW. However, in the weak coupling regime it is still possible to use a MC in order to enhance either the pumping level of the ladder, or, on the contrary, enhance the emission from the ground state. The last example is presented in the experiment discussion in Section 2.3.

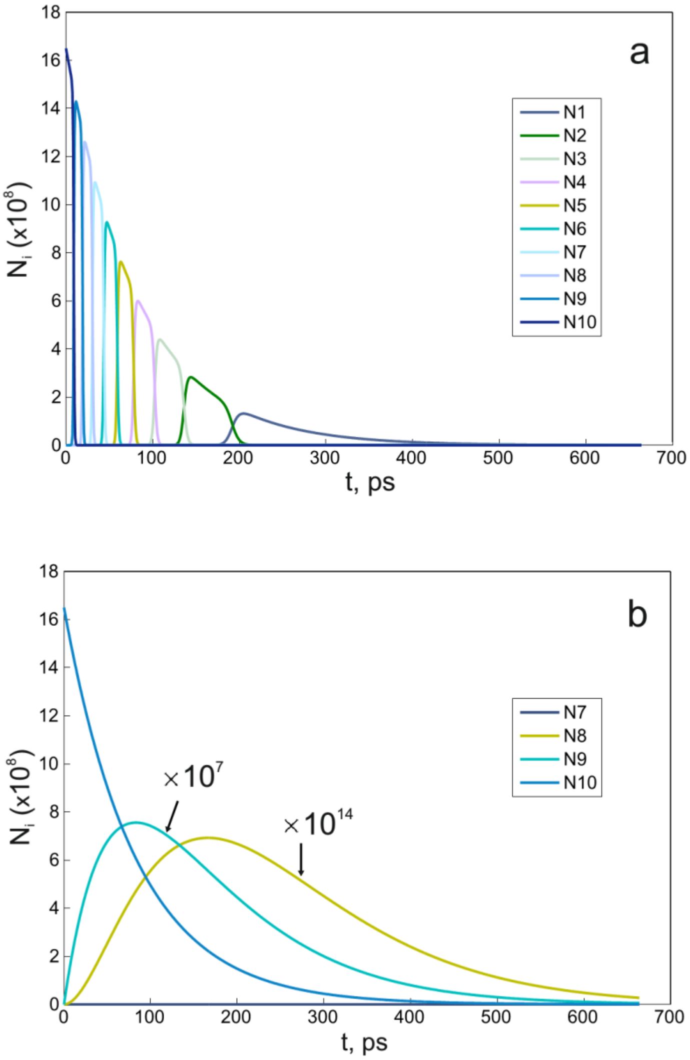

Figure 2.6: The time-dependence of energy level populations obtained by numerical simulation of a) Eqs. (2.1)-(2.3) – bosonic case, and b) equations (2.19)-(2.21) – fermionic case. W_0=1500 s^{-1}, P=10^6 W_0. The radiative decay time is constant and equal to τ =53 ps.

Figure 2.7 shows the quantum THz emission rate and the quantum efficiency of the BCL, calculated in the framework of the described model. From the data, shown in Figure 2.7(a) one can calculate the possible THz emission power that can be generated by the device: let us assume GaAs PQW with energy difference between levels equal to 6 meV. Thus, if there are 5 energy levels in the QW, for the number of initial pumped photons P =8×$10^{13}W_0$ the lasing power can reach about 0.3 mW, depending on the value of W_0. However these estimations are very rough: for the final power estimation the influence of phonon interaction should be studied carefully.

2.2.4 Double bosonic stimulation of the THZ emission

In general, the bosonic stimulation principle is equivalent to the statement that the probability of *N* bosons to be found in a single quantum state is equal to the probability to find distinguishable particles in the same state multiplied by *N*!. The more familiar statement is that for N bosons staying in the same state the probability of the N+1st boson to be found in the same state is

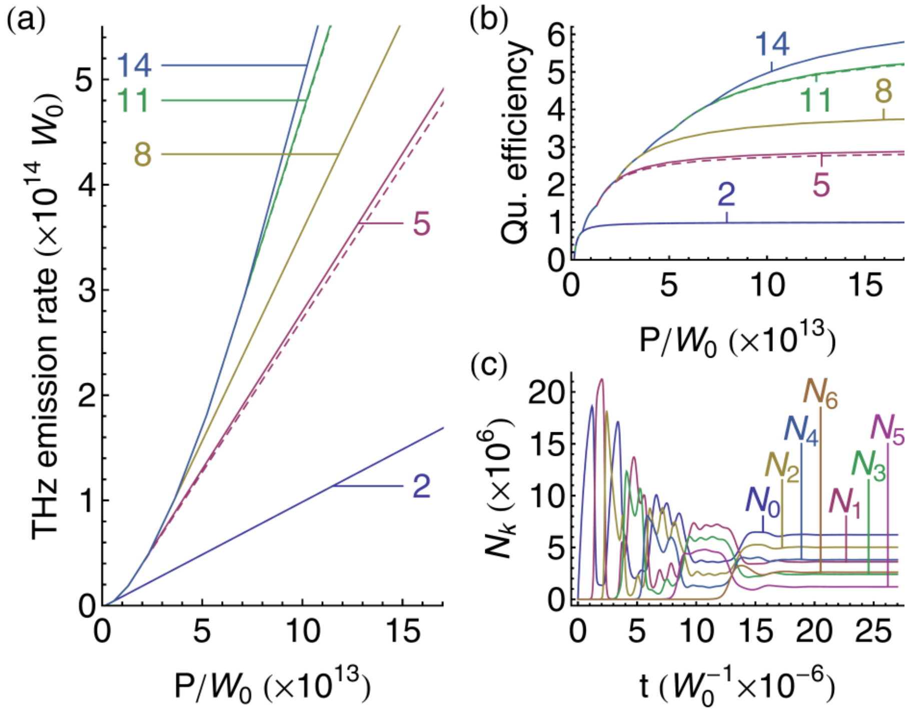

Figure 2.7: Dependence of the THz emission rate on pump intensity in the absence of a cavity for different numbers of modes in the chain (values of m are marked on the plot). Solid curves show results from numerical solutions of Eqs. (2.1)-(2.3). Dashed curves show the results of Eq.(2.4) with $W_1 = 0$, that are valid for high pump powers. (b) Dependence of the quantum efficiency on pump intensity [the values of m are the same as in (a)].
(c) Time dynamics for $m = 6$, $P = 3 \times 10^{13} W_0$. The parameters are $W_0 \tau = 8.3 \times 10^{-7}$ and $n_{THz} = 0$. Figure and caption taken from Ref. [40].

(N+1) × the probability for distinguishable particles. A nice proof of this statement is shown in Ref. [63]. The coefficient (N+1) is referred to as *the bosonic stimulation factor.* It has been already introduced in Eqs. (2.1)-(2.3).

Let us now consider the following structure: a QW is embedded into a MC, so that polaritonic energy levels are equidistant, and the whole system is placed into a THz resonator. The resonator increases the radiative lifetime of the THz photons and also increases the emission probability due to the Purcell effect. Then the system of Eqs. (2.1)-(2.3) should be solved simultaneously with the equation(2.4) describing the population of the THz mode, which will be non-zero in this case.

The emission of polaritons increases the population of the THz mode, which in turn increases the polaritonic stimulated emission transition rate between adjacent levels. So it can be treated as *double bosonic stimulation* in the system. It is essential to notice that Eqs.(2.1)-(2.4) do not include the interaction with a reservoir. In the case where bosons in the ladder interact with the reservoir, excitons may relax in energy down the ladder without emission of THz photons.

Ref. [45] provides a detailed analysis, including the equation for the reservoir population dynamics and the quantum efficiency dependence on the interactions with the reservoir. The next section shows that in real systems these interactions are not negligible, although the phonon relaxation is taken into account differently from Ref. [45].

2.3 Experimental study and modelling of relaxation processes in parabolic QWs

The experiment discussed below is intended to describe the exciton relaxation dynamics in bosonic cascades. Two parabolic QW samples with and without Bragg reflectors were explored in order to find the optimal structure characteristics for the Bosonic Cascade Laser. The PL spectra of a PQW MC sample was compared with that of a conventional MC with embedded QWs to demonstrate that the weak coupling lasing in a PQW sample can be achieved. The relaxation dynamics in a conventional QW MC and in the PQW MC was studied by the non-resonant pump-pump excitation method. A drastic difference in the relaxation characteristics between the two samples was found. The semiclassical Boltzmann equations similar to Eq.(2.1)-(2.3) were employed to reproduce the evolution of excitonic populations within the PQW as a function of the pump power and the output intensity evolution as a function of the pump-pump pulse delay. Fitting the PQW data has confirmed the anticipated cascade relaxation, paving the way for such a system to produce terahertz radiation.

2.3.1 Experimental methods:

PQW samples without and with DBRs (denoted S1 and S2 respectively) have been studied, and their relaxation and excitation characteristics have been compared to a planar MC sample with rectangular QWs (S3). All samples were fabricated with the molecular beam epitaxy. S1 contains an InGaAs/GaAs PQW of width ≈ 50 nm at the top of the potential well, and the parabolic profile was achieved by altering the indium concentration during the growth process from 2% at the InGaAs/GaAs interface to 6% in the middle of the QW (see inset in Figure 2.9(a)). Sample S2 was fabricated similarly with an $Al_xGa_{1-x}As/Al_{0.15}Ga_{0.85}As$ QW of ≈ 50 nm width, where the parabolic profile was achieved by altering the concentration of aluminium along the z-axis of the sample from 5% in the middle of the QW to 12% near the interface. The MC was formed with two DBRs, each with 17 and 22 $Al_{0.15}Ga_{0.85}As$/AlAs paired layers. The Q-factor of the MC is approximately 2000 and the PQW was placed in the middle of $3\lambda/2$ intracavity spacing. Finally a $5\lambda/2$ planar GaAs cavity, sample S3, consisting of 32 and 35 $Al_{0.15}Ga_{0.85}As$/AlAs DBR pairs and 12 rectangular QWs was studied. The Q-factor of this MC is approximately 12000.

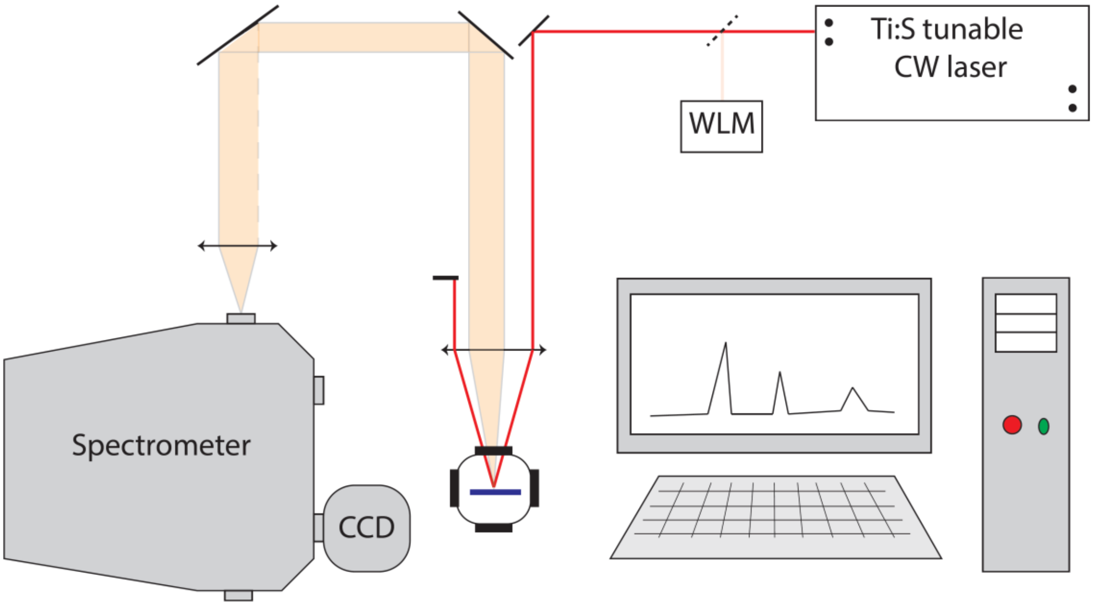

Figure 2.8: The schematic illustration of experimental setup for the charachterisation of sample S1 without PQW. The laser beam is collected on a lense in front of the sample, then the central part of the reflected beam is used for the PL analysis. WLM denotes wavelength meter.

The samples were mounted in a close-cycle cryostat to reach a temperature of roughly 5 K. Samples S2 and S3 were excited non-resonantly above the MC stopband by femtosecond pulses from a Ti:Sa laser. The laser spot size was approximately 50 µm. S1 was excited with a CW laser resonantly tuned to the exciton resonance in the barrier layers (to the 12th quantum confined excitonic state, see Figure 2.9). Such pump conditions allow creating excitons rather than electron-hole pairs. To study the exciton relaxation dynamics of S2 and S3 a pump-pump technique was used, whereby two pump pulses separated by a variable delay are used to excite a sample non-resonantly with great temporal resolution giving the time-integrated intensity of the PL as a function of the delay. The dynamics measured on a new MC sample containing a single PQW (S2) was compared with the data taken on a reference sample that is a state of the art strong coupling MC containing 12 embedded QWs and characterized by a Q-factor of 12000. Both sets of data may be described within the kinetic model that allows revealing the role of key parameters of microcavities, namely, the relaxation and radiative decay rates, the number of intermediate exciton subbands.

At first the bare parabolic QW (sample S1) was characterized in order to verify that equidistant exciton states had been achieved. In Figure 2.9 the modulated reflectance spectrum is presented (red curve) and subsequently fitted (solid black line) and up to 11 distinct excitonic states can be resolved. The energy spacing between the neighboring resonances is about 6 meV, or 1.45 THz. The inset in Figure 2.9(a) shows the potential profile for excitons in PQW (blue line) and the positions of equidistant quantum confined excitonic states (horizontal black lines), which creates the bosonic cascade ladder.

A simple analysis of the reflectivity spectrum is performed generalizing the theory developed in Refs. [64, 65] for the case of several exciton quantum confined states to fit the modulated reflection data. The modulation technique was used to reduce a noise and to stretch weak features connected to the excited quantum confined excitonic states. Following the non-local dielectric response theory [64], the amplitude reflection coefficient for a QW with several exciton resonances can be expressed in the form:

$$r_{QW} = \sum_{N=1}^{N_{MAX}} \frac{i(-1)^{N-1}\Gamma_{0N}e^{i\varphi_N}}{\omega_{0N} - \omega - i(\Gamma_{0N} + \Gamma_N)}. \tag{2.24}$$

Here ω_{0N} is the resonance frequency, Γ_{0N} and $\Gamma_N$are the radiative and nonradiative damping rates for a system of N levels. The phase φ_N in this equation takes into account a possible asymmetry of the QW potential. Reflectivity $R(\omega)$, from the structure with a top barrier layer of thickness L_b and a QW layer of thickness L_{QW}, is calculated using the transfer-matrix approach:

$$R(\omega) = \left|\frac{r_{01} + r_{QW}e^{2i\varphi}}{1 + r_{01}r_{QW}e^{2i\varphi}}\right|^2, \tag{2.25}$$

where r_{01} is the amplitude reflection coefficient from the sample surface. The phase is $\varphi = K(L_b + L_{QW}/2)$, where K is the photon wave vector in the heterostructure. The calculated derivative reflectivity spectrum is shown in Figure 2.9(a) (black curve). The peak integrated PL spectra of the sample S1 at different excitation powers has been measured (see Figure 2.9(b)). It was found that the power increase gives rise to the increase of PL intensity from the lowest exciton state followed by its saturation, contrary to the model set out in Ref. [40], where the highest level is seen to populate first, and the lowest level establishing a population last. Simultaneously, the intensity of the PL from the excited exciton states increases super-linearly with pump power and then also saturates. The similar behaviour of PL is observed for exciton states under further increase of the pump power. The full set of the PL data consisting of about 500 spectra was analysed by deconvolution of each spectrum into a set of Lorentzian resonances, corresponding to different exciton transitions. Such deconvolution fits the experimentally observed spectra, if the wavelength of excitation coincides with one of the exciton resonances in PQW or with the exciton resonance in barrier layers. In this case, the pump directly creates excitons rather than uncoupled electron-hole pairs, the relaxation of which differs from exciton relaxation. If electron-hole pairs are created by the non-resonant excitation, a broad structureless background appears in the PL spectra. It should be stressed that the observed behaviour of the time integrated PL intensities of resonant exciton peaks is a characteristic of PQWs. This is a clear indication that excitons created by resonant excitation relax via cascade between neighbouring energy levels. A reference rectangular QW of thickness of about 90 nm was studied by the same technique and found that no new exciton lines appear in the PL spectra with the pump power increase. To identify the ability of the PQW to act as a polariton laser [39] the PQW sample inside a MC was studied. Heterostructures acting as polaritonic lasers usually contain multiple thin QWs (of roughly 10 nm in width) to increase the oscillator strength of the excitonic transition in order to establish strong coupling. S2, however, contains only one PQW of about 50 nm width. The larger QW thickness and stronger overlap of the electron and hole wave functions in the PQW provides a sufficiently strong exciton-photon coupling to reach the strong coupling regime and polariton lasing possible [66].

Only the lowest energy exciton state in the parabolic QW is strongly coupled to the cavity mode in the low excitation regime. All other states are in the weak coupling regime due to the low overlap of exciton centre-of-mass wave-functions and the cavity mode. Figure 2.10(a) shows the dependencies of polariton mode energies on the laser spot position on the sample S2. One can see that the detuning between the exciton and photon resonances is dependent on the spot position. The anticrossing of polariton modes is clear evidence of the strong coupling regime. In the anticrossing range the reflectivity spectrum exhibits three distinct minima; these can be attributed to the coupling of the heavy-hole and light-hole excitons [67] to the cavity mode. The Rabi splitting of the relating polariton states is about 6 meV. The pump-power dependence of PL intensity for sample S2 is shown in Figure 2.10(b) (blue curve). The threshold-like increase of the intensity is clearly observed. The identification of the polariton or conventional laser threshold is questionable without additional experiments. What is important is that the PL intensity rises exponentially with pump power below the threshold. At the pulsed excitation this is an indication of the switching of the system to the lasing regime within a limited time window, which becomes longer as the pump power increase. The linewidth narrowing at the threshold pump power is clearly seen at in Figure 2.10(b) (red curve). This is considered as an indication that the stimulated relaxation occurs in sample S2.

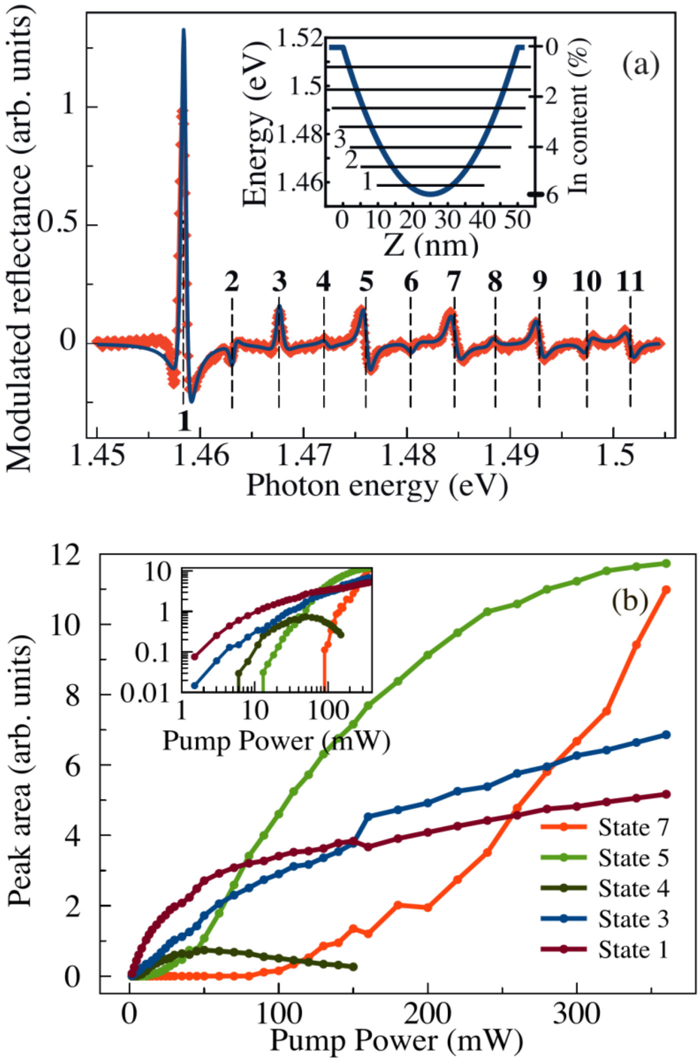

Figure 2.9: (a) λ-modulated reflectivity spectrum of sample S1 containing parabolic QW without MC (red curve) and modelled spectrum (black curve). Vertical dashed lines mark equidistant quantum confined excitonic states in the PQW. Inset: the potential profile for excitons (left axis) and distribution of indium content across the QW layer (right axis) are shown. (b) Pump power dependencies of integral PL from different quantum confined excitonic states. The pump wavelength was tuned to the exciton resonance in the barrier layer. The integral PL for each transition was obtained by deconvolution of the PL spectra into a set of Lorentzians.The inset presents the same curves plotted in logarithmic scale to show the low power region. Figure taken from Ref. [68].

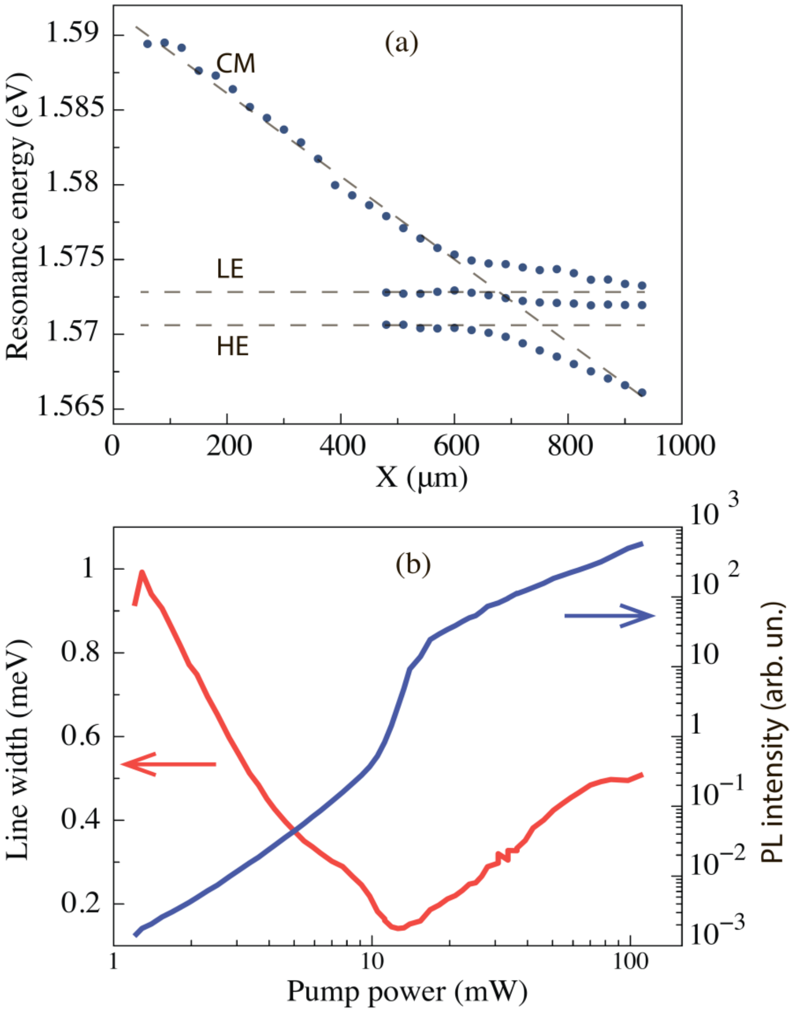

Figure 2.10: (a) The energy position of features in reflectance spectra of sample S2 as a function of the laser spot position on the sample (blue dots). Dashed lines marked as CM, LE, and HE are the energy positions of cavity mode, light-hole exciton and heavy-hole exciton respectively. Light-hole exciton is considered to be weakly coupled with the cavity mode. (b) Dependence of PL intensity (blue curve) and PL linewidth (red curve) on the excitation power; Figure taken from Ref. [68].

2.3.2 Pump – pump experiments

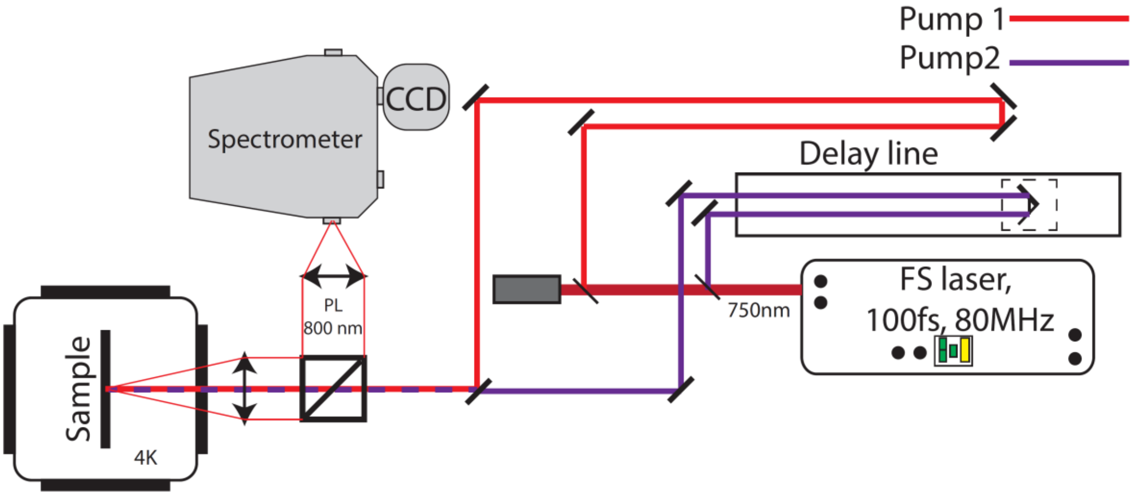

Figure 2.11: The schematic illustration of experimental setup for pump-pump experiment

The pump-pump method employed in the experiment allowed highlighting relaxation processes in the PQW within the MC that may be hidden for studies by the conventional time resolved spectroscopy methods due to the reflection from the DBRs [69]. The important property of the stimulated cascade relaxation is its strong dependence on population of the lower-lying exciton state [40]. In the pump-pump method, the first pulse creates an initial density of excitons and the delayed second pump pulse creates additional excitons at the pumped level. Relaxation of these excitons strongly depends on the population of lower energy excitonic levels created by the first pump pulse. If this population is large enough, the stimulated relaxation is triggered and accelerated. This acceleration should result in the nonlinear increase of the total PL signal excited by both pump pulses in the case of competing radiative and non-radiative channels of polariton recombination. The PL intensity should depend on the delay between two pulses; no nonlinear PL increase should occur at very large delays, where the excitons created by the first pulse relax and recombine before the second pulse arrives. The proposed method was employed for a comparative study of two samples S2 and S3. The samples were cooled down in a cryostat to 5 K and pumped by two femtosecond pulsed beams. The time integrated PL spectra were measured as functions of the delay between the pulses. Spatially broad pulses were intentionally used in order to reduce the effects of diffusion and lateral polariton drift. A detailed treatment of the formation dynamics of polariton condensates accounting for the drift and diffusion of photoexcited carriers and excitons is presented in the recent paper [70]. The goal of the present study is to reveal the specifics of momentum space relaxation in bosonic cascade structures, so the spatial dynamics of exciton clouds and polariton condensates in such structures is not taken into account.

Figure 2.13 shows the delay dependencies of time integrated PL spectra of sample S2 with PQW (a) and of sample S3 with multiple rectangular QWs (b) at the pump powers 0.25P_{th} + 1.7 P_{th}, where P_{th} is the threshold pump power for each the sample. P_{th} = 16mW for the sample S2 and P_{th}= 1.1mW for S3. The spectral diffusion as well as appearance of the additional spectral peaks are clearly observed at positive delays for both the samples. However, time scales for these processes are different. For sample S2 the second peak is developing from 30 to 50 ps, while for sample S3 it takes much longer delays, from 10 to 200 ps.

Figure 2.13shows the delay dependencies of the PL intensity measured for the samples S2 and S3 at different excitation powers of both pulses. The delay dependencies of spectrally resolved PL intensities are taken at the energies E = 1.5698 eV (left panel) and E = 1.5399 eV (right panel) corresponding to the peaks in the PL spectra. The pump powers are chosen close to the threshold of lasing. There are several peculiarities in these dependencies. Firstly, there is a strong increase of the PL at a relatively small delay. At the same time, the range of these delays is considerably smaller for PQW (150 ps) than that for rectangular QWs (several hundred ps). These means that the relaxation processes in the PQW is considerably faster than in the rectangular QWs. Secondly, additional features in these dependencies are observed. For PQW, a relatively narrow dip at zero delay is clearly seen. No such dip is observed for rectangular QWs. This is an indication of significant difference in relaxation processes in these two samples. Thirdly, some asymmetry of the dependencies for positive and negative delays is observed in both samples. It is caused by the difference in pump powers of first and second pulses. If the weak pulse comes first (negative delay), the exciton population is relatively s mall, consequently the bosonic stimulation is weak, and the relaxation of excitons created by the weak pulse is relatively slow. When the strong pulse comes first (positive delay), the stimulated relaxation is accelerated compared to the case of a weak pulse coming first. Finally, an additional peak of PL intensity is observed at the positive delay, if the power of the strong pulse is beyond the threshold. To understand the second peak at the positive delays one should discuss the time dependence of PL intensity.

In Ref. [71] the PL kinetics has been studied at different exciting powers for both below and above the threshold of polariton lasing P_{th}. It was found that when the power P < P_{th}, the PL intensity slowly rises and reaches its maximum at t_1≈ 100 ps. At later times the PL intensity slowly decreases with characteristic decay time t_2 ≈ 400 ps. When the pump power exceeds the threshold, a strong pulse of polariton laser emission appears at time t_1 with the 10-20 ps pulse duration. Such temporal behaviour of PL intensity allows assuming the following origin of the second peak in the pump dependencies shown in Figure 2.13. When the sample is pumped by two pulses and the first pulse power is above the threshold two maxima of the polariton laser emission may be seen. The reason is that the number of excitons remaining after the first pulse of polariton lasing peak and of excitons created by the second pump pulse is sufficient for the formation of the second peak of polariton laser emission. These effects with polariton lasing appearing twice are expected to be present in the sample S2 with PQW in MC as well as in the sample S3 with rectangular QW in MC. But the time delay and the width of the second peak strongly depends on the relaxation dynamics. Thus in the sample S2 the relaxation is faster than in the sample with a rectangular QW in MC.

2.3.3 Modelling

Exciton relaxation and dynamics in GaAs MCs has been extensively studied in conventional QWs [72, 73], particularly in what concerns the phonon mediated relaxation. In order to analyse the experimental data obtained for the PQW, the rate equations introduced by Liew *et al.* have been used by us with minor modifications. Let us consider m distinct excitonic levels in a PQW. The dynamics of population of each of the levels can be described by the following system of rate equations:

$$\frac{dN_m}{dt} = -\frac{N_m}{\tau_u} - \sum_{i=1}^{m-1} W_i N_m (N_{m-i}+1) + \\ + \frac{\alpha}{2} N_{m-1}^2 (N_m+1)(N_{m-2}+1) - \frac{\alpha}{2} N_m N_{m-2} (N_{m-1}+1), \tag{2.26}$$

$$\frac{dN_k}{dt} = P_k^1 + P_k^2 - \frac{N_k}{\tau_k} + \sum_{i=1}^{m-k} W_i N_{k+i}(N_k+1) - \\ - \sum_{i=1}^{k-1} W_i N_k (N_{k-i}+1) + \frac{\alpha}{2} N_{k+1}^2 (N_k+1)(N_{k+2}+1) - \\ - \frac{\alpha}{2} (N_{k+1}+1)^2 N_k N_{k+2} + \frac{\alpha}{2} N_{k-2} N_k (N_{k-1}+1)^2 - \\ - \frac{\alpha}{2} N_{k-1}^2 (N_k+1)(N_{k-2}+1) + \alpha (N_k+1)^2 N_{k+1} N_{k-1} - \\ - \alpha N_k^2 (N_{k+1}+1)(N_{k-1}+1), \qquad k = 2..m-1, \tag{2.27}$$

$$\frac{dN_1}{dt} = -\frac{N_1}{\tau_g} + \sum_{i=1}^{m-1} W_i N_{i+1}(N_1+1) + \\ + \frac{\alpha}{2} N_2^2 (N_1+1)(N_3+1) - \frac{\alpha}{2} N_1 N_3 (N_2+1)^2. \tag{2.28}$$

Here N_1 denotes to the occupation of the ground level of PQW, N_m is the occupation of the highest level, and N_k is the occupation of k-level with k = 2 . . . $m - 1$, α terms describe the exciton-exciton scattering in the system. Terms $P_k^1(0)$ and P_k^2 describe the initial two pulse excitation where the second pulse comes with a delay τ. Terms $-\frac{N_k}{\tau_k}$ for k = 2 . . . m describe both radiative and non-radiative decay rate of excitons at each level, where non-radiative decay describes losses due to phonon scattering to states with a nonzero in-plane wave vector, $k_{\parallel} \neq 0$. For the first level, only the radiative recombination is taken into account.

The model (2.26)-(2.28) neglects the absorption of THz photons in the bosonic cascades, which is valid in the absence of external THz cavity. These equations are similar to the system (2.1)-(2.3) but here one assumes that the population on each level depends on contributions from all levels, from which the transition is allowed. As was discussed in the previous section the optical transition is allowed only between levels with wave-functions of different parity. Matrix elements W_i describe the transition from any level k to any other level $k - i$ in the cascade. Transitions between adjacent levels may be mediated by the emission of THz radiation as suggested in Ref. [40]. Let us generalize this model and consider the transitions between all the levels, which is described in the above equations by summation over all levels. This generalisation can be made under two assumptions: firstly the actual profile of the potential may not be strictly given by the form of Eq.(2.7). Secondly the reservoir may be taken into account, assuming that phonon scattering allows for non-radiative transitions, and the final population can be described within the same model. In the modelling it was assumed that the pumping is centred at one of the middle levels of the cascade, k, meaning that upward scattering is possible from this level. The upward scattering due to exciton-exciton interaction populates all the levels up to the highest one labelled m. For the structure under study, the exciton-exciton scattering is found to change the amplitude of the PL signal, but does not affect the most important features of the exciton dynamics. The exciton-exciton scattering plays a minor role in our experiments and the corresponding terms in rate equations can be safely omitted.

In the experiment in the Section (2.3.2), the system is excited by femtosecond pulses which are relatively broad in energy and capable of pumping several energy levels of the cascade simultaneously. To account for the spectral broadening of the pulse in the model, it is assumed that polaritons are excited not only at the level k, but also at the nearest levels $k - 1$ and $k + 1$. In the numerical simulations, the cascade is considered to have the maximum number of occupied exciton levels m = 9 with the level k = 6 receiving the major part of input pulses power, $2P/3$, and levels k = 5, 7, receiving 1/6 of total input power each.

The following parameters are used in the calculations: W_1 = 1500 s^{-1} , W_2 = W_4 = 500 s^{-1}, W_3 = 100s^{-1}, W_5 = 2500 s^{-1}, τ_g = 11 ps, τ_p= 55 ps, and τ_u= 22 ps. where τ_g, τ_p, τ_u are the decay times for the ground level, pumped levels, and levels above the pumped one, respectively. Figure 2.12 shows the time evolution of exciton densities at each energy level in the QW, plotted for two different delays between the pulses. As seen from the figure, the population dynamics is quite complex. If the system is excited by a single pulse (solid lines in Figure 2.12), pumped levels 5–7 are populated and other levels are almost empty at the initial time interval (t < 10 ps) after the pulse. Due to the high exciton density at the level 5, $N_5 \gg 1$, the Bose-stimulated relaxation from the upper levels 6 and 7 is switched on and the population of this level dramatically increases.

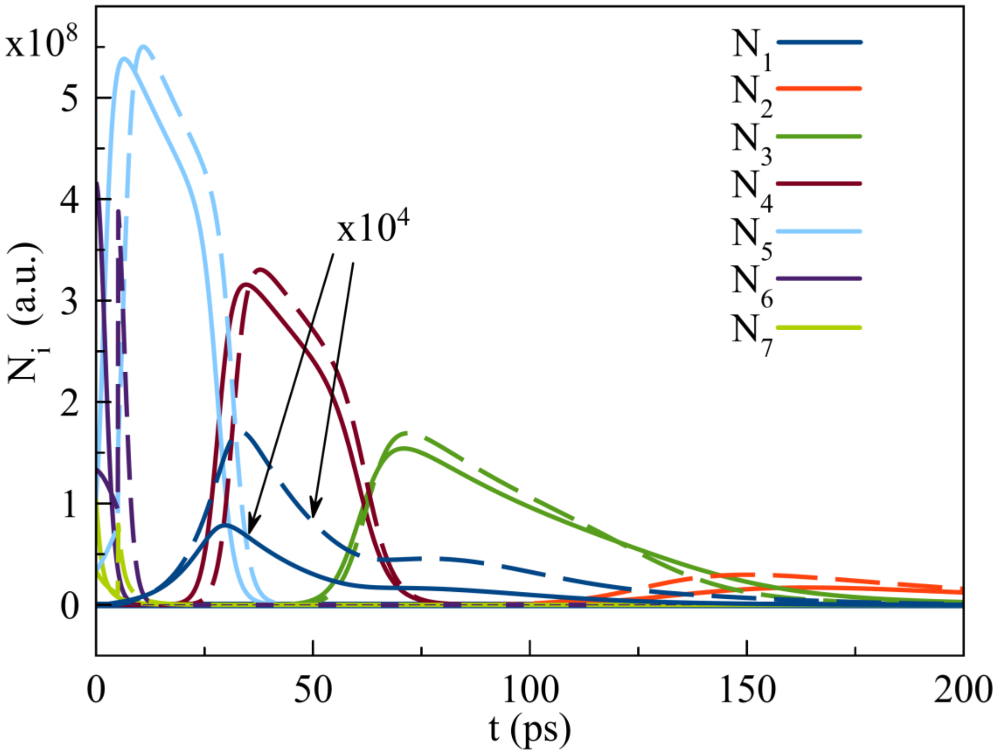

Figure 2.12: Time evolution of exciton densities at each level in the QW. Solid lines are calculated for zero delay between pulses and dashed lines show the same for $\tau_{\text{delay}} = -5$ ps. Figure taken from Ref. [68].

The population of level 5 reaches its maximum at t ≈ 5 ps, while levels 6 and 7 become empty. The low-lying levels, i = 4 ... 1, are slowly populated while the exciton density is not reached a critical value for Bose-stimulated relaxation. This critical value is achieved for the level 4 first because, in the framework of the model, the relaxation between adjacent levels is more efficient, so $W_1 > W_2..W_4$. This explains the threshold-like increase of population of the level 4 at time t ≈ 30 ps. Similarly, populations of levels 3 and 2 rapidly increase at time t ≈ 60 ps and t ≈ 120 ps, respectively (see respective curves in Figure 2.12). However, the population of the lowest exciton level 1, is not efficiently boosted via this pathway because of the low population of the adjacent level 2. Therefore, the model assumes that there is a direct relaxation of excitons from the pumped level 5 to the lowest level. As one will see below, this process explains the second maximum observed experimentally in pump-pump experiments (see Figure 2.13, left panel).

As discussed in the previous subsection, radiative transitions between levels, where the wave functions have the same parity, are forbidden. However, through the modelling process it was found that transitions W_2 and W_4 are essential to fit the second peak appearing at the 50 ps delay. So the possible explanation that is consistent with the theory of BCL are that the phonon transitions to k=0 state also play a role. So in this model these transitions are taken into account separately from the terms $-\frac{N_k}{\tau_k}$ that describes the phonon scattering to states with a nonzero in-plane wave vector, $k_\parallel \neq 0$. These non-radiative losses also compete with the relaxation processes. The integral magnitude of losses depends on the time, spent by excitons at the excited levels. This time can be drastically shortened and, respectively, the PL yield can be increased, if appropriate experimental conditions initiating the Bose stimulated relaxation are fulfilled, in particular, the excitation power, which should be close to the threshold power for polariton lasing [74, 75]. Separation of the excitation pulse in two pulses also helps controlling the population of different exciton levels (see Figure 2.12) and, hence, the non-radiative losses. Once the excitons created by the first pulse have relaxed to the fifth level (it takes about 5 ps), the excitons created by the second pulse delayed by τ = 5 ps rapidly relax from the sixth and seventh levels to the fifth one via Bose-stimulated process. This stimulation gives rise to the increased population of level 5 relative to that obtained for zero delay, as one can conclude comparing solid and dashed lines N_5 in Figure 2.12. The corresponding increase of population is observed also for other levels. In particular, a remarkable increase of population is observed for level 1, which is the key point for understanding of the dip in the delay dependence of PL intensity observed experimentally (see Figure 2.13, left panel). Figure 2.14 shows the integral PL intensity, I_{PL}, as a function of the delay between pulses, τ_{delay}, for two excitation powers with total power, $P_{(1)} + P_{(2)} < P_{th}$, where P_{th} is the threshold power for polariton lasing. Curves I_i represent the contribution of each transition term having form $W_{i-1}N_i\ (N_1 + 1)$ for i =2 ... 6, into the total PL. As one can see from the figure, the modelling predicts a dip in the PL intensity at the small delays. It is clear from the discussion above that the dip is due to the increase of PL intensity at the delay increases up to several picoseconds.

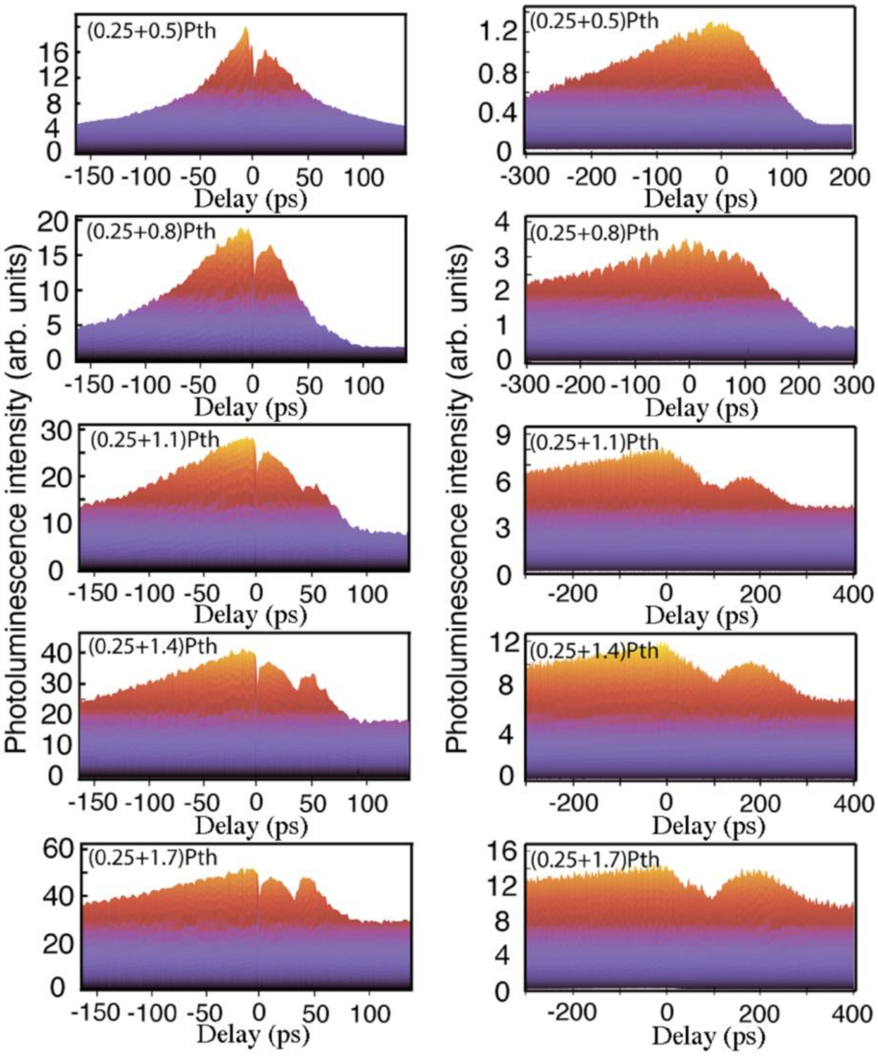

Figure 2.13: Experimental measurements discussed in the end of the subsection 2.3.2: PL spectra measured as a function of the delay between the pump pulses for sample S2 with PQW (left panel) and sample S3 containing multiple rectangular QWs in a MC (right panel). Figure taken from Ref. [68].

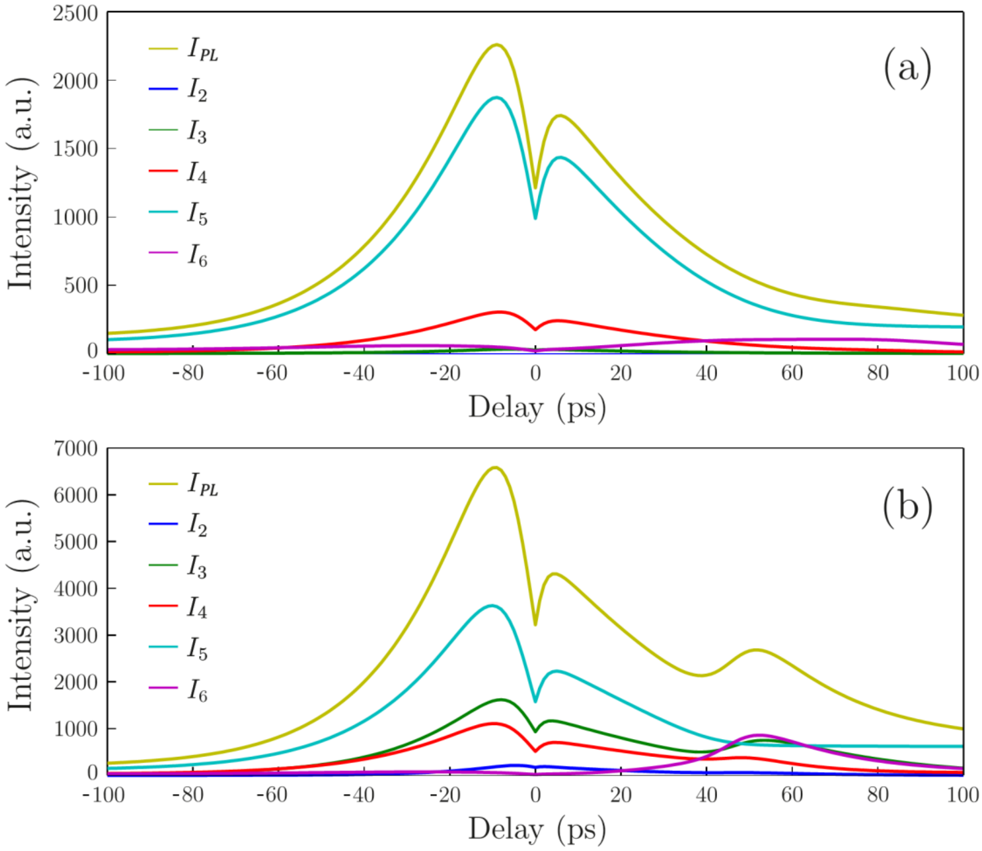

Figure 2.14: Modelling of pump-pump signal with use of rate equations: delay dependencies of total PL intensity I_{PL} from the ground exciton level, and separate contributions of each transition I_i= $W_{i-1}N_i$ (N_1 + 1) for i = 2 . . . 6, plotted for two different values of pump powers: (a) $P_{(1)}$= 0.3 × P_{Thr}, $P_{(2)}$= 0.25 × P_{Thr} and (b) $P_{(1)}$ = 0.7 × P_{Thr}, $P_{(2)}$= = 0.25 × P_{Thr}. Figure taken from Ref. [68].

The further increase of delay between the pulses gives rise to the depopulation of level 5 when the second pulse arrives. As a result the Bose-stimulated relaxation of levels 6 and 7 excited by the second pulse becomes less efficient and the non-radiative losses increase. This explains the decrease of PL intensity at delays τ = 10 ... 40 ps (see Figure 2.14(b)). However, when the delay τ > 40 ps, the population of the ground exciton level is so large ($N_1 \ll 1$) that the direct Bose-stimulated relaxation from level 6 described by term W_5N_6 (N_1+ 1) becomes an efficient pathway for the exciton relaxation to the ground level. Respectively, efficient depopulation of level 6 occurs that results in the decrease of non-radiative losses. These processes explain the appearance of a second peak at the delay dependence of PL intensity. The calculated behaviour of total PL intensities at weak and strong pumping qualitatively reproduces the experimental results (compared to Figure 2.13).

The PL intensity for the conventional rectangular QW can be modelled with the same set of equations (2.26)-(2.28). However due to the large separation of energy levels the initial pumping populates only single energy levels, while neighbouring levels stay empty. This leads to the disappearance of the dip in the PL profile as it is shown in the experiment (Figure 2.13, right panel).

2.4 Conclusions

Present experiments and modelling shed light on the exciton dynamics in bosonic cascades, the pump-pump method being a powerful tool for the study of the fast relaxation dynamics at the non-resonant pumping. When the only one pump pulse is used for excitation, the relaxation occurs via one pathway. Using the second pulse allows one to switch the relaxation between different pathways depending on delay between the pulses which is demonstrated experimentally and through modelling. The qualitative agreement was found between the theoretical model of a BCL in a PQW system and experimental results. Because the pump-pump method is based on strong nonlinearity of PL yield on the pump power, which is close to the threshold, the quantitative agreement of the theory and the experiment was not reached. However, the modelling showed that there are two different pathways for relaxation in the system. The first pathway is the relaxation via cascade transitions, where all levels are being filled, and the second pathway is the direct transition from the pumped level to the ground one. By taking these pathways into account, the model may be generalized for larger number of levels or for other initial conditions. Taking into account the fact that minimum in the PL at zero delay occurs only if polaritons are exited on at least two adjacent levels, it is possible to explain the difference in PL for PQW and bare QW shown in Figure 2.13 the levels in bare QW stand far from each other and polaritons are excited only at one energy level. Due to this there is no minimum at zero delay between pump pulses. Nevertheless, the relaxation process in the bare QW still may be described by the rate equations, but with different values of parameters.

The consequential continuation in the development of the BCL model would be implementing the phonon interactions into the theory and finding experimental structures, where phonon relaxation can be reduced.

In this work I have reproduced the results of the paper [40], plotted extra results for the fermionic case and provided modelling support for the relaxation dynamics in the experiment [68].

Chapter 3: Polariton – mediated superconductivity

The phenomenon of superconductivity is one of the most fascinating problems of modern physics. Since its discovery in metals in 1911 at cryogenic temperatures plenty of experimental developments were made, so now there are compounds acquiring superconducting properties at temperatures over 160K. However, there is no unified explanation of this phenomenon and the theoretical aspects of high-temperature superconductivity still have to be developed.

In this Chapter I discuss one of possible mechanisms of superconductivity – light induced superconductivity. This theory is built upon the conventional model of attractive electron-electron interaction, but the phonon mediation is replaced by the mediation by excitations of an exciton-polariton BEC. The structures that are proposed to be suitable for observation of the effect pertain to the class of hybrid Bose-Fermi structures – layered semiconductor crystals with embedded QWs, where the QW with BEC is adjacent to the QW with a 2D electron gas (2DEG). This structure is schematically shown in Figure 3.1.

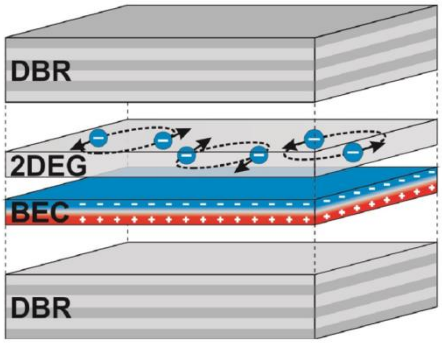

Figure 3.1: A schematic illustration of the hybrid Bose-Fermi structure, discussed in this Chapter. Figure taken from Ref. [76].

The two subsystems (BEC and 2DEG) exhibit different quantum effects as a result of their statistics. In Refs. [77, 78] the softening of polariton dispersion and transition of BEC into the supersolid phase are demonstrated. At the same time a 2DEG may exhibit superconducting and CDW state [79]. The last is an ordered quantum fluid of electrons where the electrons form a standing wave pattern.

This Chapter is devoted to the investigations on superconductivity in a 2DEG layer in the weak coupling regime, meaning that the electrons in the 2DEG QW are weakly coupled to the polaritons in the adjacent QW, and implying the validity of the Bardeen-Cooper-Schrieffer theory. In particular, the dependence of the critical temperature on the magnetic field and the densities of 2DEG and polariton BEC was investigated. Bearing in mind the recent appearance of new materials based on TMDC monolayers that exhibit unique excitonic properties, this type of superconductivity can possibly be observed in TMDC microcavities.

3.1 Introduction

One of the most gripping phenomena in the modern physics is the superconductivity. It was discovered in 1911 by the Dutch physicist H. Kamerlingh-Onnes, who observed an abrupt vanishing of the resistivity of solid mercury at T = 4.15 K. Later the same observations at different temperatures were done in lead, tin, thallium, uranium, and other metals. The investigations on the decay time of superconducting currents showed fascinating results: in 1963 J. File and R. Mills studied the decrease of the superconducting current in a $Nb_{0.75}Zr_{0.25}$ solenoid by measuring the magnetic field with the nuclear magnetic resonance method. The experiment showed that the characteristic decay time of the current is longer than 100000 years [80].

Superconductors exhibit unusual properties in the presence of magnetic fields. In 1933 W. Meissner and R. Ochsenfeld demonstrated that if a superconductor is cooled down below the critical temperature in the external magnetic field, the field lines are completely ejected from the bulk of a sample [81]. Such materials are called type I superconductors. Their superconducting properties completely vanish at the critical value of the magnetic field B_C. Type II superconductors exhibit a completely different behaviour: there are two critical values of magnetic field B_{C_1} and B_{C_2}. In the region below $B_{C_1}$the magnetic field stays at the surface of the superconductor, while in the region $B_{C_1} < B < B_{C_2}$ the magnetic field penetrates inside the bulk and superconducting vortices are formed. The metal still remains in the superconducting state, however, the magnetic field flux through it is not equal to zero. Typically $B_{C_2} \gg B_{C_1}$, which allows applications of these materials in engineering. Nowadays all superconducting magnets are based on the Type II superconductors.

Later in 1950s the isotope effect that is the dependence of the superconducting critical temperature on the nuclear mass was shown [82, 83, 84], proving the important role of the lattice and electron-phonon interactions in superconductivity. The explanation of the isotope effect was given by Fröhlich in Ref. [85], where the electron-phonon interaction was first theoretically described.

The theoretical investigations of superconductivity began in 1935, with the introduction of the London equations [86]. The main assumption of the London's model was that electrons in superconductors form circular currents that fully screen the applied magnetic field. By relating this superconducting current with the magnetic field the Meissner effect was described. This theory is purely phenomenological and has a few drawbacks, where the main one is the underestimation of the magnetic field penetration depth.

Later L. Landau and V. Ginzburg created a model that described the second order phase transition from metallic conductivity to superconductivity with a non-linear Schrödinger-like equation. The second order phase transition theory is based on the assumption that there exists an order parameter, which describes the loss of symmetrical properties of the system. The order parameter is zero at the normal state, and it deviates from zero continuously in the ordered state. In the description of superconductivity this order parameter was assumed to be proportional to the density of carriers of the superconducting current. The theory successfully described the Meissner effect and the distinction of the two types of superconductors. Later it was shown that the Ginzburg-Landau theory is the limiting case of the full microscopic model, valid at temperatures close to the phase transition temperature.

3.2 BCS approximation

The breakthrough in the investigations of the superconductivity phenomenon came in 1957 when John Bardeen, Leon Cooper, and John Robert Schrieffer published the seminal paper on the microscopic theory of superconductivity (BCS model) [87].

This work is based on two main previously established properties of the Fermi gases in solids. The first one is the existence of an effective attraction between two electrons that stems from the phonon mediation. Instead of using the realistic microscopic treatment of the interaction, Bardeen *et al.* used the toy “jellium” model, where the artificial and structureless background charge interacts electrostatically with itself and with the electrons. The electron-electron potential (Bardeen-Pines potential) in this model reads:

$$U_{BP}(\omega,\boldsymbol{q}) = \frac{e^2}{\varepsilon(q^2+q_{TF}^2)}\left[1+\frac{\omega_{ph}^2(\boldsymbol{q})}{\omega^2-\omega_{ph}^2(\boldsymbol{q})}\right], \tag{3.1}$$

where ε is the dielectric permittivity, q_{TF} is the dielectric screening constant, $\hbar\omega_{ph}$ is the phonon dispersion, $\hbar\omega$ is the exchanged (phonon) energy and $\boldsymbol{q}$ is the exchanged (phonon) wave vector. The Fourier transform of this potential is time-dependent that reflects the retardation effect.

The second development was done by L. Cooper. In 1956 he found that two electrons near the Fermi level are unstable towards the formation of a Cooper pair for an arbitrarily small attractive interaction and the energy of this bound state is lower than the energy of an unbound electron-electron pair on the Fermi surface [88]. So one would expect that the many body electronic system is unstable towards the formation of a new ground state, formed by Cooper pairs of electrons. This final step accounting for the collective nature of superconducting state completed the microscopic description of the superconductivity phenomenon.

The BCS Hamiltonian can be expressed in the form:

$$H_{BCS} = \sum_{\boldsymbol{k},\sigma} \xi_{\boldsymbol{k}} \hat{c}^{\dagger}_{\boldsymbol{k}\sigma} \hat{c}_{\boldsymbol{k}\sigma} + \sum_{\boldsymbol{k},\boldsymbol{k}'} \mathrm{V}_{\boldsymbol{k},\boldsymbol{k}'} \hat{c}^{\dagger}_{\boldsymbol{k}\uparrow} \hat{c}^{\dagger}_{-\boldsymbol{k}\downarrow} \hat{c}_{-\boldsymbol{k}'\downarrow} \hat{c}_{\boldsymbol{k}'\uparrow}, \tag{3.2}$$

where $\xi_{\boldsymbol{k}} = \epsilon_{\boldsymbol{k}} - \mu$, $\epsilon_{\boldsymbol{k}} = \hbar^2 k^2 / 2m^*$, μ is the chemical potential, $\hat{c}^{\dagger}_{\boldsymbol{k}\sigma}, \hat{c}_{\boldsymbol{k}\sigma}$ are the electron creation and annihilation operators. $\mathrm{V}_{\boldsymbol{k},\boldsymbol{k}'}$ is the interaction potential between the electrons with corresponding absolute values of momenta. This Hamiltonian can be rewritten in the mean field approximation, accounting for the term $\langle \hat{c}^{\dagger}_{\boldsymbol{k}\uparrow} \hat{c}^{\dagger}_{-\boldsymbol{k}\downarrow} \rangle \neq 0$, which corresponds to the Cooper pair wave function in superconducting state. Introducing the fermionic Bogoliubov transformation [89], that reads:

$$\hat{c}^{\dagger}_{-\boldsymbol{k}\downarrow} = u_{\boldsymbol{k}} \hat{\gamma}^{\dagger}_{-\boldsymbol{k}\downarrow} - v^*_{\boldsymbol{k}} \hat{\gamma}_{\boldsymbol{k}\uparrow}, \tag{3.3}$$

$$\hat{c}_{\boldsymbol{k}\uparrow} = u^*_{\boldsymbol{k}} \hat{\gamma}_{\boldsymbol{k}\uparrow} + v_{\boldsymbol{k}} \hat{\gamma}^{\dagger}_{-\boldsymbol{k}\downarrow}, \tag{3.4}$$

and after some math one can introduce the superconducting ground state wave function, which is the quasi-vacuum in the new basis of quasi-particles, called bogolons.

$$\hat{\gamma}_{\boldsymbol{k}\sigma} |\Psi_{BCS}\rangle = 0. \tag{3.5}$$

In terms of the initial electron creation and annihilation operators $|\Psi_{BCS}\rangle$ can be rewritten as:

$$|\Psi_{BCS}\rangle = \prod_{\boldsymbol{k}} (u_{\boldsymbol{k}} + v_{\boldsymbol{k}} \hat{c}^{\dagger}_{\boldsymbol{k}\uparrow} \hat{c}_{-\boldsymbol{k}\downarrow}) |0\rangle, \tag{3.6}$$

where $|0\rangle$ is the Fermi sea, $u_{\boldsymbol{k}}$ and $v_{\boldsymbol{k}}$ are the parameters, satisfying the condition $u^2_{\boldsymbol{k}} + v^2_{\boldsymbol{k}} = 1$. The minimization of the expectation value of the Hamiltonian (3.2) in the ground state allows determining these parameters and leads to the self-consistent condition:

$$\Delta_{\boldsymbol{k}} = \sum_{\boldsymbol{k}'} V_{\boldsymbol{k}\boldsymbol{k}'} \frac{\Delta_{\boldsymbol{k}'}}{2\sqrt{\xi^2_{\boldsymbol{k}'} + \Delta^2_{\boldsymbol{k}'}}}, \tag{3.7}$$

where $\Delta_{\boldsymbol{k}} \equiv 1/N \sum_{\boldsymbol{k}'} V_{\boldsymbol{k}\boldsymbol{k}'} \langle \hat{c}_{-\boldsymbol{k}'\downarrow} \hat{c}_{\boldsymbol{k}'\uparrow} \rangle$ is the gap function, that can be expressed in terms of $u_{\boldsymbol{k}}$, $v_{\boldsymbol{k}}$, and $E_{\boldsymbol{k}} = \sqrt{\xi^2_{\boldsymbol{k}'} + \Delta^2_{\boldsymbol{k}'}}$ is the quasi-particle excitation energy.

Assuming that the interaction potential $V_{\boldsymbol{k}\boldsymbol{k}'}$ is constant and attractive in the certain frequency range, i.e.

$$V_{\boldsymbol{k}\boldsymbol{k}'} = \begin{cases} -V, & |\xi_{\boldsymbol{k}}|, |\xi_{\boldsymbol{k}'}| < \omega_D \\ 0\,, & |\xi_{\boldsymbol{k}}|, |\xi_{\boldsymbol{k}'}| \geq \omega_D, \end{cases} \tag{3.8}$$

where ω_D is the phonon Debye frequency, the gap function is independent on the wave vector and it is constant in the region of the attractive potential. Then the gap equation (3.7) may be simplified to:

$$1 = \frac{V}{2}\sum_{\boldsymbol{k}} \frac{1}{E_{\boldsymbol{k}}}. \tag{3.9}$$

The summation in the Eq.(3.9) can be replaced by integration over energy, which leads to

$$1 = \mathcal{N}V \int_{0}^{\hbar\omega_D} \frac{d\xi}{\sqrt{\xi^2 + \Delta^2}}, \tag{3.10}$$

with $\mathcal{N}$ being the density of states at the Fermi surface in the normal state. If $\mathcal{N}V \ll 1$, that means the weak coupling condition being satisfied, then

$$\Delta \approx 2\,\hbar\omega_D e^{\left(-\frac{1}{\mathcal{N}V}\right)}. \tag{3.11}$$

At finite temperatures this equation may be generalized as follows:

$$\Delta(\xi, T) = -\int_{-\infty}^{\infty} \frac{U(\xi - \xi')\Delta(\xi', T)\, tanh\left(\frac{E(\xi')}{2k_B T}\right)}{2E(\xi')} d\xi' , \tag{3.12}$$

where $U(\xi - \xi')$ is an arbitrary potential, k_B is the Boltzmann constant. The critical temperature T_c of the phase transition is then determined as the temperature, at which the gap function turns to zero. Substituting the potential (3.8) into the Eq.(3.12) one can find T_c as:

$$k_B T_c = 1.13\,\hbar\omega_D\, exp\left(-\frac{1}{\mathcal{N}V}\right). \tag{3.13}$$

Qualitatively, the BCS mechanism can be understood as follows: a single electron, moving in the lattice of ions creates a distortion in the ion positions, producing the local uncompensated positive charge. Due to the difference in the electron and ion masses the lattice response is much slower, compared to the electron motion. So at a later time this charge attracts another electron, when the first one is away at a long distance, which can be of the order of 100 nm. At such distances the Coulomb repulsion does not affect these electrons, so that a bound state can b formed. Being composed bosons, the Cooper pairs are subject to the collective phenomena, similar to superfluidity. The superfluid current of Cooper pairs is responsible for the superconductivity.

3.3 Exciton-polariton mediated superconductivity

The typical transition temperature in superconducting metals is of the order of several Kelvin. In order to increase this temperature one may try to increase either the Debye energy or the interaction strength in Eq.(3.13).

The Cooper model predicted that the pair of electrons can be formed at any arbitrary attraction, independently on its nature and interaction strength. Hence, phonons are by no means a unique agent possibly providing for the electron-electron attraction. In the light of this, in 1964 the idea of exciton mediated superconductivity was first proposed by W. Little [90]. Then a further development to this proposal was done by V. Ginzburg [91] and D. Allender *et al.* [92], who considered layered metal-semiconductor structures as candidates for exciton-mediated superconductivity. The goal set by these authors was to increase the cutoff frequency by replacing the phonon mediation by the virtual exciton mediation. However, the experimental attempts to realize this idea faced two major obstacles: firstly, the energy cost of creating an excitation in the semiconductor layer is very high. Secondly, the retardation effect in such systems is suppressed, because the average speed of the exciton, created due to the interactions in metal and semiconductor is high in comparison to the speed of sound, which means that the resulting Cooper pairs would be small in size and the Coulomb repulsion cannot be neglected. Most likely for these two reasons, the exciton-mediated superconductivity was never observed. A significant development towards the implementation of the exciton-mediated superconductivity was made by Laussy *et al*. in Ref. [93], where the authors suggested that excitations in a BEC of exciton-polaritons can play the role of mediators of Cooper pairing. Accounting for the possibility of the room-temperature polariton BEC this mechanism potentially can lead to the formation of a superconducting state at room temperatures as well.

The proposed structure for the studies of exciton BEC-mediated superconductivity is shown in Figure 3.1. It consists of a pair of DBRs and two adjacent QWs placed at the maximum of the optical field confined in a MC. One QW contains a 2DEG which can be created by the doping. The neighbouring QW contains a BEC of exciton polaritons that can be pumped optically. It is essential, that in this model there is no difference if there is a thermal equilibrium or a driven-dissipative BEC in the QW.

3.3.1 Interaction Hamiltonian

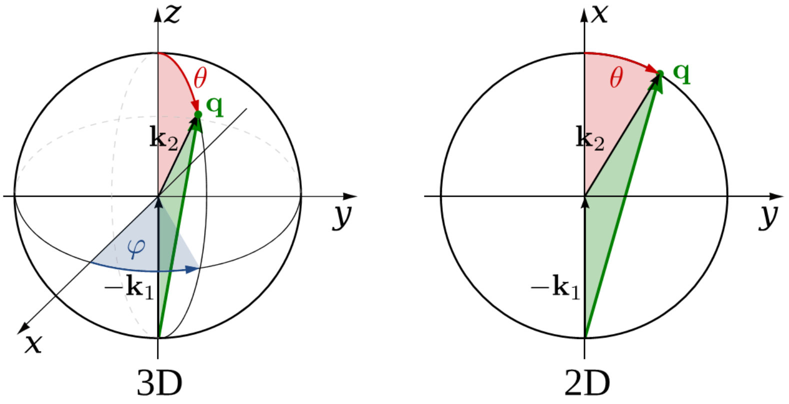

Figure 3.2: Fermi surface average in 3D and 2D case. Vectors $\boldsymbol{k_1}$ and $\boldsymbol{k_2}$ are the initial vectors of the two electrons lying on the Fermi surface. The vector $\boldsymbol{q}$ is the exchange wave vector between the interacting electron pair. Figure taken from the Ref. [94].

As in the BCS approach, here it is assumed that only the electrons that stay on the Fermi surface can form Cooper pairs. The model microscopic Hamiltonian, describing the interactions in the layered system reads [94]:

$$H = \sum_{\boldsymbol{k}} E_{pol}(\boldsymbol{k})\hat{a}^{\dagger}_{\boldsymbol{k}}\hat{a}_{\boldsymbol{k}} + \sum_{\boldsymbol{k}} E_{el}(\boldsymbol{k})\hat{c}^{\dagger}_{\boldsymbol{k}}\hat{c}_{\boldsymbol{k}} + \sum_{\boldsymbol{k_1},\boldsymbol{k_2},\boldsymbol{q}} V_C(\boldsymbol{q})\hat{c}^{\dagger}_{\boldsymbol{k_1+q}}\hat{c}^{\dagger}_{\boldsymbol{k_2-q}}\hat{c}_{\boldsymbol{k_1}}\hat{c}_{\boldsymbol{k_2}}$$
$$+ \sum_{\boldsymbol{k_1},\boldsymbol{k_2},\boldsymbol{q}} X^2 V_X(\boldsymbol{q})\hat{c}^{\dagger}_{\boldsymbol{k_1}}\hat{c}_{\boldsymbol{k_1+q}}\hat{a}^{\dagger}_{\boldsymbol{k_2+q}}\hat{a}_{\boldsymbol{k_2}} + \sum_{\boldsymbol{k_1},\boldsymbol{k_2},\boldsymbol{q}} \hat{a}^{\dagger}_{\boldsymbol{k_1}}\hat{a}^{\dagger}_{\boldsymbol{k_2+q}}\hat{a}_{\boldsymbol{k_1+q}}\hat{a}_{\boldsymbol{k_2}}, \quad (3.14)$$

where $E_{pol}(\boldsymbol{k})$ and $E_e(\boldsymbol{k})$ are the in-plane polariton and 2DEG dispersions, V_C and V_X are the electron-electron Coulomb interaction and the electron-exciton interaction respectively, U is the polariton-polariton interaction strength.

The ***electron-electron*** Coulomb repulsion in this model is given by the conventional Yukawa potential, which accounts for the 2DEG screening:

$$V_C(q) = \frac{e^2}{2A\varepsilon(|\boldsymbol{q}| + \kappa)}, \quad (3.15)$$

where κ is the screening constant, A is the normalization area.

The ***electron-polariton*** interaction in the Hamiltonian (3.14) is the most important part, because it essentially determines the shape of the interaction potential. The electron in a 2DEG QW interacts with the excitonic part of the polariton, so the interaction depends on the excitonic Hopfield coefficient. Taking into account only the direct interactions and eliminating the exchange interactions one can write the matrix element of electron-exciton interaction as:

$$V_X = \int \Psi_X^*(\boldsymbol{Q}, \boldsymbol{r_e}, \boldsymbol{r_h})\Psi^*(\boldsymbol{k}, \boldsymbol{r_1})V(\boldsymbol{r_1}, \boldsymbol{r_e}, \boldsymbol{r_h})\Psi_X(\boldsymbol{Q}, \boldsymbol{r_e}, \boldsymbol{r_h})\Psi(\boldsymbol{k}, \boldsymbol{r_1})d\boldsymbol{r_1}d\boldsymbol{r_e}d\boldsymbol{r_h}, \qquad (3.16)$$

where the electron wave function is a plane wave and the exciton is assumed to be in the 1*s*-state:

$$\Psi(\boldsymbol{k}, \boldsymbol{r_1}) = \frac{1}{\sqrt{A}}e^{i\boldsymbol{kr_1}}, \qquad (3.17)$$

$$\Psi_X(\boldsymbol{Q}, \boldsymbol{r_1}, \boldsymbol{r_2}) = \sqrt{\frac{2}{\pi A}}\frac{U_e(z_e)U_h(z_h)}{a_B}e^{i\boldsymbol{QR}_X}e^{-\frac{r_X}{a_B}}. \qquad (3.18)$$

R_X and r_X are the exciton centre of mass and relative motion coordinates, a_B is the exciton Bohr radius, $U_h(z_h), U_e(z_e)$ are the electron and hole envelop wave functions in the direction normal to the QW plane. Taking into account the dipole moment of the exciton in the direction perpendicular to the QW plane, the electron-exciton matrix element can be expressed as:

$$\begin{aligned} V_X(q) = {} & \frac{ede^{-qL}}{2\varepsilon A}\left[\frac{\beta_e}{[1+(\beta_e q a_B/2)^2]^{3/2}} + \frac{\beta_h}{[1+(\beta_h q a_B/2)^2]^{3/2}}\right] \\ & + \frac{e^2 e^{-qL}}{2q\varepsilon A}\left[\frac{1}{[1+(\beta_e q a_B/2)^2]^{3/2}} - \frac{1}{[1+(\beta_h q a_B/2)^2]^{3/2}}\right], \end{aligned} \qquad (3.19)$$

where $\beta_{e,h} = m_{e,h}/(m_e + m_h)$, $m_{e,h}$ are the effective electron and hole masses, L is the distance between the 2DEG and BEC QWs, d is the dipole moment [95]. One can see that the interaction can be enhanced by increasing the dipole moment of excitons, which in turn can be controlled by applying an external electric field.

The ***polariton-polariton*** interaction stems from the interaction of the excitonic parts of the polaritons. It is common to assume that this interaction does not depend on a wave vector and spin. The direct dipole-dipole interactions appear to be negligible in comparison to exchange interactions. Under these assumptions the polariton-polariton matrix element takes the form [96]:

$$U = \frac{6a_B^2 E_B X^4}{A}. \qquad (3.20)$$

Knowing the matrix elements of the interactions one can continue with reducing the Hamiltonian (3.14) to the form of the BCS Hamiltonian (3.2), in order to leave only the electron-electron interaction for the electron pairs. The main difference between the present and the BCS effective interactions is that in the case of polariton mediation the Coulomb repulsion cannot be neglected.

The Hamiltonian transformation starts from the mean field approach, applied to the polariton condensate i.e. $\hat{a}_{k+q}^\dagger \hat{a}_k \approx \langle \hat{a}_{k+q}^\dagger \rangle \hat{a}_k + \hat{a}_{k+q}^\dagger \langle \hat{a}_k \rangle$ and $\langle \hat{a}_k \rangle = \sqrt{AN_0}\delta_{k,0}$, where N_0 is the polariton density in the condensate. Then the diagonalisation of the Hamiltonian via the Bogoliubov transformation leads to the following form:

$$H = H_{el} + H_{bog} + H_C + H_{el-bog}, \tag{3.21}$$

where the Coulomb interaction and the free electron energy stay unchanged and

$$H_{bog} + H_{el-bog} = \sum_{\boldsymbol{k}} E_{bog}(\boldsymbol{k})\hat{b}^\dagger_{\boldsymbol{k}}\hat{b}_{\boldsymbol{k}} + \sum_{\boldsymbol{k},\boldsymbol{q}} M(\boldsymbol{q})\hat{c}^\dagger_{\boldsymbol{k}}\hat{c}_{\boldsymbol{k}+\boldsymbol{q}}\left(\hat{b}^\dagger_{-\boldsymbol{q}}+\hat{b}_{\boldsymbol{q}}\right), \tag{3.22}$$

with E_{bog} being the dispersion of elementary excitations of the condensate, $\boldsymbol{q} = \boldsymbol{k_1} - \boldsymbol{k_2}$, $q^2 = 2k_F^2(1 + cos\theta)$. Schematically the exchanged wave vector is shown on Figure 3.2. In the case of polariton BEC E_{bog} takes the form:

$$E_{bog}(\boldsymbol{k}) = \sqrt{\left(\tilde{E}_{pol}(\boldsymbol{k}) + 2AUN_0\right)\tilde{E}_{pol}(\boldsymbol{k})}, \tag{3.23}$$

with $\tilde{E}_{pol}(\boldsymbol{k}) = E_{\boldsymbol{pol}}(\boldsymbol{k}) - E_{\boldsymbol{pol}}(0)$. The renormalized electron-bogolon interaction reads:

$$M(\boldsymbol{q}) = \sqrt{AN_0}X^2V_X(\boldsymbol{q})\sqrt{\frac{E_{bog}(\boldsymbol{q}) - \tilde{E}_{pol}(\boldsymbol{q})}{2AUN_0 - E_{bog}(\boldsymbol{q}) + \tilde{E}_{pol}(\boldsymbol{q})}}. \tag{3.24}$$

Applying the Fröhlich transformation to the Hamiltonian (3.21) one can obtain the BCS-like form:

$$H_{eff} = \sum_{\boldsymbol{k}} E_e\hat{c}^\dagger_{\boldsymbol{k}}\hat{c}_{\boldsymbol{k}} + \sum_{\boldsymbol{k_1},\boldsymbol{k_2},\boldsymbol{q}} V_{eff}\hat{c}^\dagger_{\boldsymbol{k_1}}\hat{c}_{\boldsymbol{k_1}+\boldsymbol{q}}\hat{c}^\dagger_{\boldsymbol{k_2}+\boldsymbol{q}}\hat{c}_{\boldsymbol{k_2}}, \tag{3.25}$$

where V_{eff} is a sum of the Coulomb repulsion and the bogolon-mediated attractive part:

$$V_{eff}(\omega, q) = V_C(\boldsymbol{q}) + V_a(\boldsymbol{q}, \omega), \tag{3.26}$$

where

$$V_a(\boldsymbol{q}, \omega) = \frac{2M^2(\boldsymbol{q})E_{bog}(\boldsymbol{q})}{(\hbar\omega)^2 - E^2_{bog}(\boldsymbol{q})}. \tag{3.27}$$

One can see that this interaction is proportional to the density of particles in the condensate so V_a can be controlled by optical pumping.

By averaging over the Fermi surface one can obtain the energy dependent interaction potential. This averaging physically means that the interaction is isotropic:

$$U_0(\omega) = \frac{A\mathcal{N}}{2\pi}\int_0^{2\pi} (V_A(\omega, \boldsymbol{q}) + V_C(\boldsymbol{q}))d\vartheta. \tag{3.28}$$

In order to define the critical temperature of superconducting phase transition, the interaction (3.28) is used in the gap-equation (3.12) .

3.3.2 Modelling results

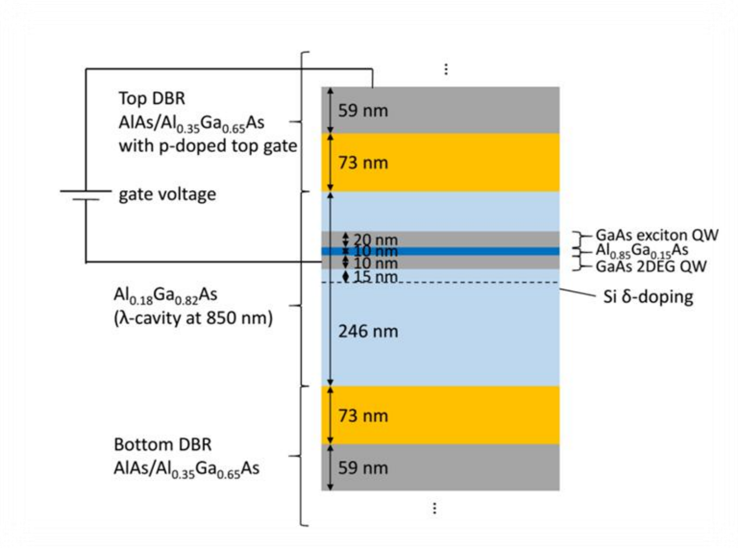

Figure 3.3: Schematic illustration of the GaAs MC design, proposed by T. Fink, S. Flt, and A. Imamoglu

In this section the described approach is used to model the effect in the real layered structure based on GaAs/AlGaAs QWs. The schematic illustration of the structure is shown in Figure 3.3. In order to induce a stationary exciton dipole moment, the polariton condensate is expected to be subject to an external gate voltage in the growth direction as shown in Figure 3.3. The parameters, used in the calculations are shown in Appendix A.

Figure 3.4 shows the characteristic values of the conduction and valence bands for different gate voltages. In order to calculate the dipole moment of the excitons in the condensate the normalized wave functions $\Psi_{\mathrm{e}}(\mathrm{z})$ and $\Psi_{\mathrm{h}}(\mathrm{z})$ were obtained for the electron and the hole, using the software nextnano, that implements finite difference methods to solve the k.p-Schrodinger-Poisson equation. The dipole moment is given by:

$$ed = e\int (|\Psi_e(z)|^2 - |\Psi_h(z)|^2) z dz,$$

In the right panel of the Figure 3.4 the exciton dipole moment dependence on the external gate is shown. One can see that the dipole moment reaches a maximum value of 13 nm before the external gate breaks the exciton. The total exciton density N_0 is also affected by the external bias, due to the thermal dissociation of weakly bound excitons. Therefore, the external gate will play an important role, since it affects simultaneously the exciton population and the dipole moment.

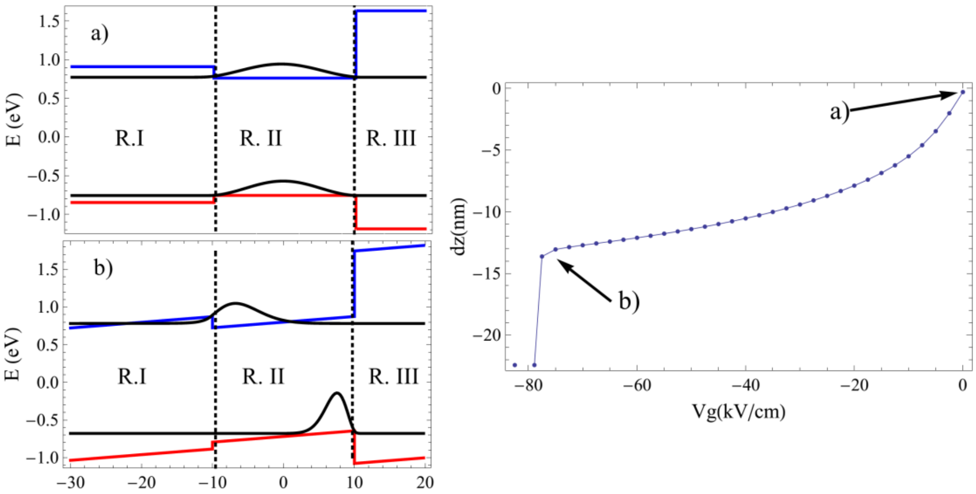

Figure 3.4: Exciton QW. The valence(red) and conduction(blue) band are divided in 3 subregions separated by dashed vertical lines. Region I (R.I) corresponds to $Al_{0.18}Ga_{0.82}As$, R.II corresponds to $GaAs$ and R.III is $Al_{0.85}Ga_{0.15}As$. The black lines show the electron $|\Psi_e(z)|^2$ and hole $|\Psi_h(z)|^2$ probability densities shifted to their respective eigenvalue for a) $V_g = 0$ and b) $V_g = -75\ kV/cm$. Right panel: Exciton dipole dz as a function of the external gate voltage V_g

Figure 3.5 represents the results of interaction potential calculations and the solution of the gap equation. As one can see from the Eq.(3.27) the magnitude of the interaction potential increases linearly with N_0. This is illustrated by Figure 3.5(a), where it is clear that the higher N_0 is, the higher is the magnitude and the broader is the attraction region. This effect is observed in a wide range of polariton density values. The only essential limitation to this mechanism of SC is the Mott transition from an exciton (exciton-polariton) condensate to an electron-hole plasma. On the contrary, Figure 3.5(b) shows that a high electron density leads to the decreasing magnitude of the negative part of the potential that corresponds to the attraction between electrons. The obtained result is important for designing microstructures exhibiting HTSC, as it demonstrates the advantage of fully semiconductor heterostructures over the metal-semiconductor heterostructures.

Taking into account the complexity of the interaction the gap equation (3.12) with substituted interaction (3.27) is solved numerically. Here I solve it using the iteration method. The example of solution is shown in Figure 3.5(c) and (d).

It is assumed that only the electrons on the Fermi surface form Cooper pairs. Here it means that only the point $\Delta(0)$ has a physical meaning. If $\Delta(0) > 0$, then Cooper pair can be formed. The critical temperature T_C can be defined as the temperature below which $\Delta(0)$ is not equal to zero.

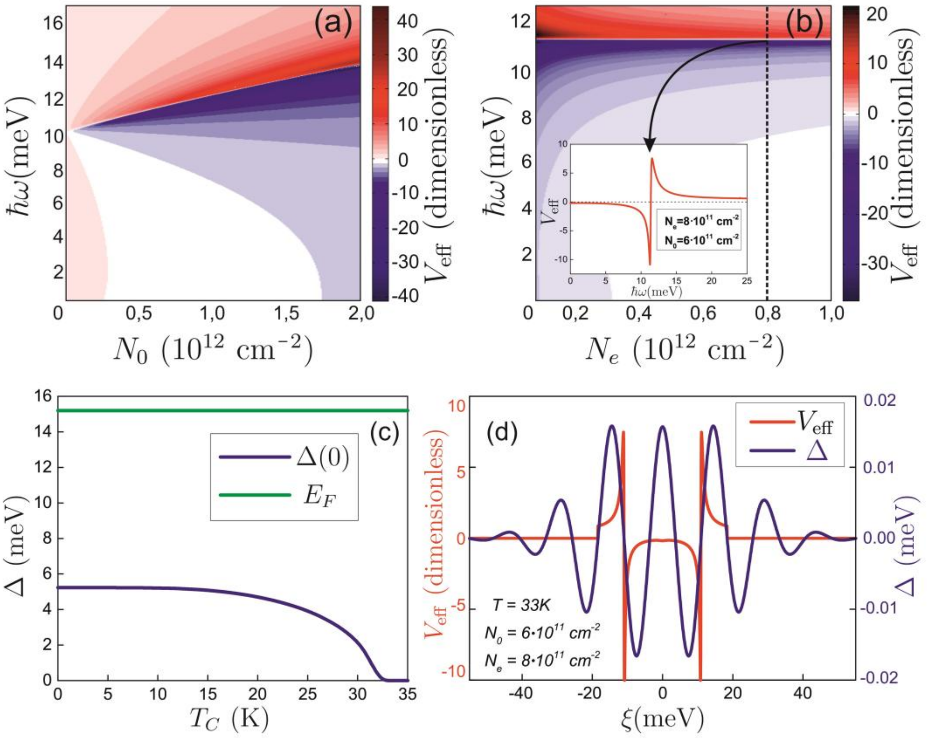

Figure 3.5: The magnitude of effective interaction potential as a function of (a)density of polaritons N_0 and (b) density of electrons in 2DEG QW.The color shows the magnitude in dimensionless units.Blue region corresponds to the effective attraction between electrons, red region represents the repulsion.The inset presents the profile of the potential at the particular concentration N_e. Graphs (c) and (d) show the solution of the gap-equation. (c): Δ(0) as a function of temperature. The critical temperature T_C in this case is equal to 33K. (d): solution of the Eq.(5) at $T = T_C$. The results are presented for the potential with $N_e = 8 \times 10^{11}$cm^{-2} and $N_0 = 6 \times 10^{11}$ cm^{-2}. Figure taken from Ref. [76].

Figure 3.6 represents the critical temperature of the superconductivity phase transition as a function of the electron density in a 2DEG QW. The green line shows the temperature that corresponds to the Fermi-energy, the other lines represent the dependencies of T_C on the electron density for different values of exciton-polariton density. One can see that the increase of the electron density N_e leads to the reduction of the critical temperature. The coloured area shows the range of parameters where the theory is applicable. The limitations for the theory are the following: firstly, the thermal energy of electrons at the critical temperature must be lower than the Fermi energy. Otherwise, one cannot assume that electrons forming the Cooper pairs are located at the Fermi surface. Secondly, the absolute value of the gap-energy must be lower than the Fermi energy. In

Figure 3.6 the area of validity of the discussed approach is limited by $E_F = k_B T$ line. The density $N_0 = 4 \times 10^{12}$cm^{-2} is apparently beyond the Mott transition threshold, therefore high T_C predicted by this line is unrealistic and is presented only for showing the tendency of T_C growth. On the other hand, the exciton-polariton density $N_0 = 4 \times 10^{11}$ cm^{-2} is achievable in realistic QW structures based on GaAs, so critical temperatures of the order of a few tens of Kelvin must be achievable in semiconductor structures. The superconducting currents may be observed in the considered structures until the critical current density is achieved.

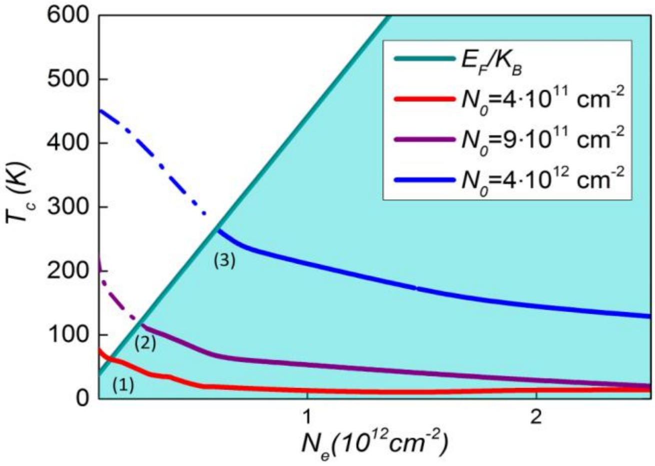

Figure 3.6: The dependence of TC on the concentration of electrons in 2DEG QW, plotted for three different polariton concentrations N0. Dashed parts of the curves show the region where the theory is not applicable. Curves 1 and 2 represent the parameters of the condensate that are achievable in a realistic GaAs-based semiconductor structures. Figure taken from Ref. [76].

It can be conveniently derived from the superconducting gap $\Delta(0)$ as in Ref. [97]:

$$j_C = \frac{eN_e\Delta(0)}{\hbar k_F}. \tag{3.30}$$

Figure 3.7(a) shows the critical current j_C, calculated as a function of the electronic density N_e and temperature. One can see that the highest current density corresponds to the lowest concentrations and the lowest temperatures on the graph, that fully agrees with the qualitative analysis.

Let us now discuss the behaviour of exciton-mediated superconductors in the presence of external magnetic fields. It is known that in bulk superconductors the Meissner effect exists until the critical magnetic field is achieved. This field is linked to the critical current. Namely, the critical field induces a surface current equal to j_C. Once the surface currents, providing a full screening of the magnetic field inside the superconductor, exceed the critical current, the superconductivity is suppressed. In Ref. [76] in 2D system the magnetic field direction perpendicular to the QW plane was considered. The superconducting layer is much thinner than the typical penetration length of the magnetic field into the superconductor, so the Meissner effect cannot be observed. The superconductivity is still suppressed by the magnetic field in this case, but the gap vanishes at the critical field B_{cr}. In order to find B_{cr} and the critical temperature the magnetic field in the gap equation is accounted for, using the condition $\Delta(0, T, B_{cr}) = 0$. The field reduces the density of electronic states in the 2DEG layer which leads to the increase of the radius of the Fermi circle. A minor effect is the modification of the electron-exciton interaction potential due to the shrinkage of the exciton Bohr radius.

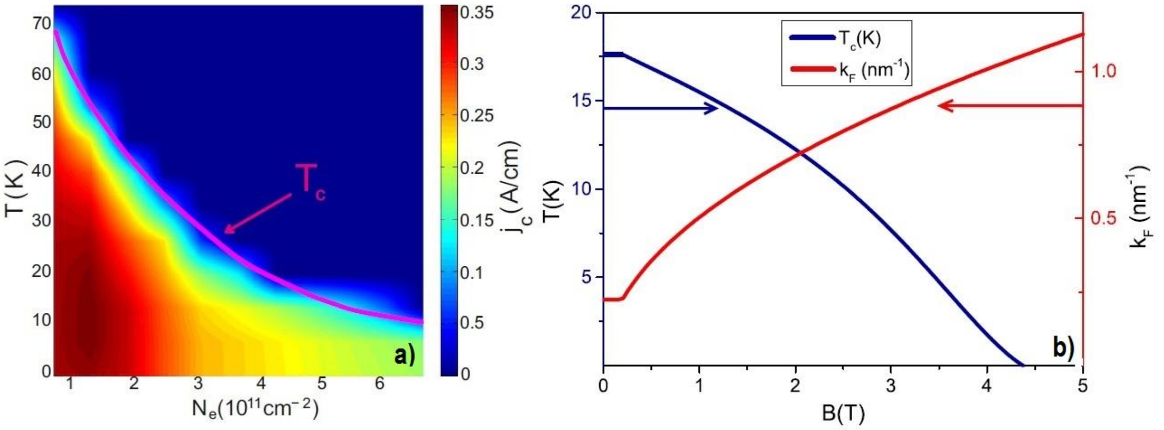

Figure 3.7: (a) The dependence of the critical current j_c on the temperature and electron concentration. (b)Fermi wave vector (red curve) and critical temperature(blue curve) as a function of magnetic field B. $N_e = 8 \times 10^{11}$ cm $^{-2}$.The Dingle broadening of Landau Levels Γ is taken to be 0.3 meV, that corresponds to the cyclotron energy $\hbar\omega_c$ at B=0.2T. Figure taken from Ref. [76].

To account for the magnetic field effect on k_F, the authors used the expression for the radii of the circles in the reciprocal space, that correspond to Landau levels in the quasi-classical approximation [98]:

$$k_p^2 = \left(p + \frac{1}{2}\right)\frac{2eB}{\hbar c}, p = 0,1,2 \dots . \tag{3.31}$$

Electrons may occupy quantum states in the Γ vicinity of these circles, where Γ is the Dingle broadening of Landau levels dependent on the structural disorder and scattering processes. The area occupied by electrons in the reciprocal space at each circle at zero temperature may be found as:

$$S_p = 2\pi k_p \delta k_p, \delta k_p = \frac{2m\Gamma}{\hbar^2 k_p}, \tag{3.32}$$

The Fermi wave-vector is expressed as $k_F = k_M$, where the index M can be found from the condition:

$$\frac{2}{(2\pi)^2}\sum_{p=0}^{M-1} S_p < N_e \leq \frac{2}{2\pi^2}\sum_{p=0}^{M} S_p \tag{3.33}$$

Figure 3.7(b) shows k_F and T_C as functions of magnetic field B for the fixed electron and polariton densities. All parameters are the same that were used for potential calculation for GaAs-structure. In this case $N_e = 8 \times 10^{11}$ cm^{-2}, $N_0 = 6 \times 10^{11}$ cm^{-2}, the Dingle broadening of Landau levels is taken to be to 0.3 meV. At low magnetic fields given by the condition $\hbar\omega_C < \Gamma$ it is assumed that

$k_F = k_F(B = 0)$, neglecting the weak oscillations of k_F due to the oscillating electron density of states [99].

3.4 Conclusions and perspectives

The modelling of the results reported in the previous section showed that fully semiconductor structures, combining doped and undoped QWs provide higher critical temperatures than metal-semiconductor structures. This can be explained by the fact that exciton mediated attraction weakens with the increase of the Fermi energy faster than the Coulomb repulsion does. In the absence of magnetic field this model yields the critical temperatures of the order of 50 K in realistic GaAs-based microcavities. Also, it is shown that magnetic fields may strongly affect the Fermi wave-vector k_F, which is why the critical temperature decrease and eventually vanishes at $B_{cr} =$ 4T. The increase of k_F accounts for the reduction of the effective area occupied by each electron in the real space due to the cyclotron motion. The used quasi-classical approximation is limited at strong quantizing magnetic fields. As long as the quantum Hall regime is not established and the number of filled Landau levels $N \gg 1$, the quasi-classical approach is applicable. In our case, the number of occupied Landau levels is over 10 even at $B\sim$ 4 T, which allows one to consider the quasi-classical result as a trustworthy approximation. Other effects which may influence B_{cr} include the electron Zeeman splitting and edge current effects. GaAs/AlGaAs QWs are characterized by low Lande factors $g\sim$ 0.01 depending on the actual heterostructure parameters. The electron Zeeman splitting in the considered range of magnetic fields $B\sim$4T is of the order of a few μeV and it is negligible with respect to other characteristic energy scales.

My contribution to this work includes reproduction of the results, obtained by Fabrice Laussy in Ref. [94] and calculating the critical temperature as a function of the electron and polariton densities. I also analysed the behaviour of the critical temperature as a function of magnetic field described in Subsection 3.3.2 and calculated the critical currents shown in Figure 3.7(a). The results of this work are published in a peer reviewed journal (see Ref. [76]).

All these calculations are done in the framework of the BCS approximation, which actually means that the interaction between electrons in 2DEG layer and the condensate is weak enough, $\mathcal{N}V \ll 1$. In particular, this implies that a small dipole moment d is induced. In addition, neither properties of the condensate, nor changes induced to the condensate wave function by the 2DEG are taken into account in the model. If the condition of weak coupling is not satisfied, the Migdal-Eliashberg theory should be preferential over our model in order to find the critical temperature. In Refs. [77, 78] the effect of the 2DEG on the condensate, which leads to the formation of the supersolid phase is discussed. The interplay between the condensate in the supersolid state and the 2DEG can break superconductivity and lead to the formation of charge density wave state in the 2DEG layer. The latter effect in hybrid Bose-Fermi structures is still not fully theoretically described and might be quite promising for investigations. The problem of the exciton-mediated superconductivity in the limit of the strong coupling regime becomes particularly interesting considering the appearance of a new material platform based on TMDC monolayers, that exhibit unique excitonic properties in comparison to the conventional semiconductors (see Chapter 4 for the discussion).

Finally, even within the BCS model there are still interesting problems left to be explored. In particular, in Ref. [92] the interplay between the exciton and phonon mediated superconductivity was discussed. It is shown that if the exciton mediation is considered simultaneously with the phonon one, the critical temperature is increased. In Ref. [100] it is shown that the presence of one mediation mechanism enhances the other, resulting in the resonant increase of the critical temperature. It would be interesting to find realistic parameters for the structure, where the BCS approach is applicable and construct the full picture of the critical temperature behaviour at different limits by finding the electron density in 2DEG layer, at which the phonon mediation becomes negligible in comparison to the exciton mediation.

Currently there are some reports, showing that a light-induced superconducting state can be found in some cuprates and fullerenes [101, 102]. However, there is no evidence of light-induced superconductivity in hybrid Bose-Fermi structures. The observation of this phenomenon in such systems at any temperature would be a significant breakthrough and will open new frontiers in polaritonics.

Chapter 4: TMDC monolayers as novel materials for Polaritonics

Inspired by the discovery of graphene, the field of two dimensional (2D) materials has rapidly extended to a larger variety of atomically thin materials. Within this field, the group of transition metal dichalcogenides (TMDCs) has attracted a great attention due to its unique physical properties. In this Chapter the recent experiments investigating the excitonic properties of TMDC monolayers are discussed and their theoretical description is presented.

4.1 Introduction

TMDC materials were well known since the early 60-s of the previous century [103]. These materials are characterized by strong covalent interatomic bonds in the plain of a single layer and weak Van der Waals forces between the neighboring atomic layers. This is the reason why they are used as dry lubricants in mechanical systems. The major interest in these materials arose in the last decade, after the discovery of graphene [104]. The subsequent research showed that the transition from 3D-crystals to 2D films dramatically changes the physical properties of the TMDC. Since 2010 2D films of TMDCs are subject to an intensive research. In this chapter we shall consider atomically thin TMDC. This means in particular, that the layer thickness is orders of magnitude thinner than the characteristic wavelength of light corresponding to the excitonic transitions involved. For TMDC monolayers the layer thickness is about several angstroms.

Different TMDC monolayers demonstrate either metallic or semiconducting properties depending on the metallic element constituting the compound. As discussed in review [105] compounds MoX_2 and WX_2 are semiconducting, while, for example, NbX_2 and TaX_2 are metallic. The main interest to semiconducting TMDC films arose when it was discovered that the band gap transition in the Γ-point, which is indirect for the bulk materials, changes to the direct one in a TMDC monolayer. The typical value for the energy gap lies in the optical range. For example, in MoS_2 $E_g \sim 2$ eV, that corresponds to the orange light.

A TMDC monolayer is a material characterized with a chemical formula MX_2, where M is a transition metal element and X is a chalcogen atom, typically these are S, Se and Te. In TMDC structures the layer of metallic atoms is gripped between two layers of chalcogens. Each metallic atom is connected to two chalcogens, so the elementary cell consists of three atoms. From the top the monolayer exhibits a graphene-like hexagonal structure, but with two different atoms in vertices. The example of such a structure is shown in Figure 4.1(a).

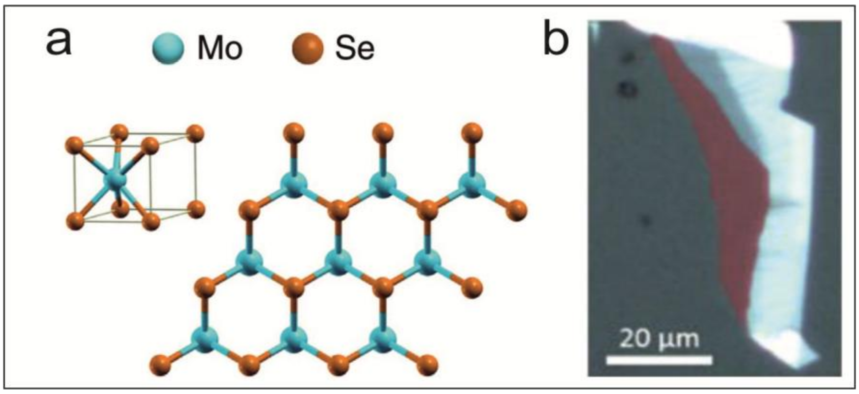

Figure 4.1: (a)Elementary cell and hexagonal structure of $MoSe_2$, picture taken from Ref. [106]. (b) False-color optical microscopy image of the WSe_2 flake, used in experiment discussed in Section 4.4 (monolayer in red shaded area). Figure taken from Ref. [107].

All ways to synthesize these materials can be divided into 2 groups: top-down methods and bottom-up methods. In top down methods the 2D film is isolated from the bulk material by application of an external force; in bottom-up processes atoms are deposited onto a substrate by chemical or thermal reaction in order to form the 2D film.

Among top-down methods the most widely used way to obtain the monolayers is the mechanical exfoliation, where the atomically thin films are peeled from the bulk crystal by micromechanical cleavage, using an adhesive tape. The advantage of this method is that it is a low-cost process that allows synthesizing high purity samples that can be used for fundamental research and for fabrication of devices. An exfoliated flake can be easily recognized by putting it on a substantially thick substrate that yields clear optical contrast between the wafer and the sample flake. The number of layers in the flake can be clearly recognized by the optical contrast. In 2012 the technique allowing for the laser reduction of the thickness of a TMDC sample down to a monolayer [108] has been established. However, this method does not allow for controlling the flake size and it is thus not suitable for large-scale applications. Figure 4.1 b shows the monolayer of WSe_2, obtained by exfoliation, that was used for the experiment in the Section 4.4.

Other top-down methods to produce 2D TMDC, that are widely used, are liquid phase preparations [109], ultrasonic and chemical exfoliation. These methods can be used for obtaining large quantities of exfoliated films.

Bottom-up techniques mainly include various chemical vapor deposition methods (CVD), that at first became widely used for graphene film synthesis and this method allowed for a large scale device fabrication and hydrothermal synthesis. Recently some CVD methods of the growth of TMDC monolayers have been reported ([110], [111], [112]).

4.1.1 Electronic properties:

For digital logic transistors, that are one of the most important applications of semiconductor materials, the most important properties are high conductivity, high charge carrier mobility, needed for fast operation, high ratio of on-state and off-state conductance and low off state conductance. The mobility of the carriers mostly depends on the Coulomb scattering that occurs at charged impurities in the monolayer, scattering on acoustic and optical phonons and on surface or interface phonons. All these mechanisms play a role at different temperatures. The room temperature mobility in semiconducting TMDC monolayers is limited to ~410 $cm^2 V^{-1} s^{-1}$. Presently, the on/off current ratio reaches up to 10^8 in MoS_2 monolayers. In Ref. [113] an example of the field effect transistor based on TMDC monolayer was demonstrated.

The future directions of TMDC electronics lie in the development of high performance flexible logical components. Another potential application is based on the TMDC monolayer analogue of high-electron-mobility transistors, that are conventionally fabricated from planar junctions of semiconductors of different band gaps [105]. In these devices the semiconductor that is characterized by a smaller band gap is highly doped, while the other one is left undoped. If the two layers are brought into contact the electrons from the doped layer move into the undoped layer and are free to move with minimum scattering from dopants. TMDCs can be adapted to this device architecture because the different TMDCs have a range of band gaps and similar lattice constants.

4.1.2 Excitonic properties:

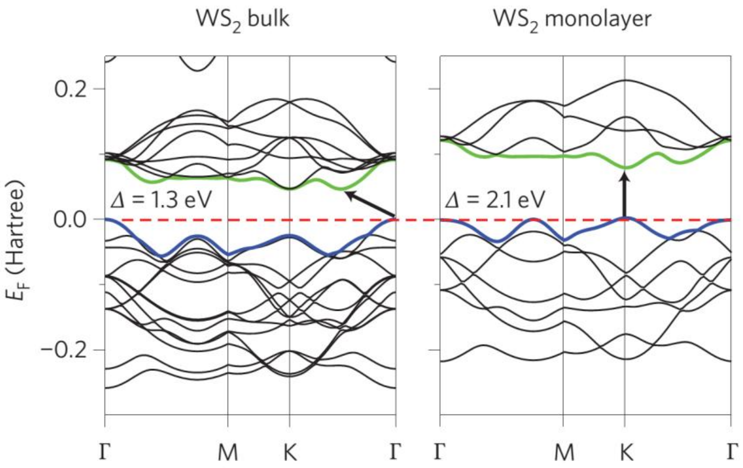

Figure 4.2: The band structures calculated from first-principles density functional theory (DFT) for bulk and monolayer WS_2. The horizontal dashed lines indicate the Fermi level. The arrows indicate the fundamental bandgap (direct or indirect). The top of the valence band (blue) and bottom of the conduction band (green) are highlighted. Figure taken from the Ref. [114].

The direct gap in semiconducting TMDC monolayers occurs due to the quantum confinement and the resulting change in the hybridization between p orbitals on chalcogenide atoms and *d* orbitals at the metal atoms [115]. Because of this transition from indirect to direct gap, the TMDC monolayers demonstrate a set of interesting optical properties. TMDC monolayers have band gaps in the optical range of frequencies (see Table 4-1). The simple Wannier–Mott model describing an exciton as a hydrogen-like atom yields the following value of the exciton binding energy E_b and the exciton Bohr radius a_B, respectively:

$$E_b = \frac{2\mu e^4}{\varepsilon^2 \hbar^2} \approx 0.5\, eV\, ;\; a_B = \frac{\varepsilon \hbar^2}{2\mu e^2} \approx 6\, \text{Å} \tag{4.1}$$

Such a high binding energy is achieved due to the heavy electron and hole masses that govern the reduced mass μ. Monolayer parameters taken for this calculation are tunable by a mechanical strain or an electric field, examples of the measured dielectric constants at a particular energy for different TMDC monolayers are given in the Table 4-1. Nevertheless, this does not change the fact that the exciton binding energy in these materials is orders of magnitude higher than in conventional semiconductors: for comparison, in GaAs the binding energy $E_b = 0.01$ eV, while the band gap $E_g = 1.5$ eV.

	WS_2	WSe_2	MoS_2	$MoSe_2$
E_g (eV)	2.05 Ref. [116]	1.66 Ref. [117]	1.88 Ref. [117]	1.58 Ref. [116]
ε	16	18	21	26

Table 4-1: Band gaps and real parts of the complex in-plane dielectric functions of monolayer MoS_2, $MoSe_2$, WS_2, and WSe_2, over photon energies of 1.5 eV. Imaginary part for this frequency is equal to zero. Proper measurements of dielectric functions are shown in Ref. [118]

In semiconducting TMDC monolayers the conduction and valence band edges are situated in two unequal K-points of the hexagonal Brillouin zone. The two valleys K and K' are separated in the momentum space. Due to the heavy atomic masses there is a strong spin-orbit coupling. However, unlike graphene, TMDC monolayer crystals do not possess inversion symmetry. As discussed in [119], this leads to a giant spin splitting of both valence and conduction bands. The splitting has opposite signs in the two valleys, which allows selective optical pumping of these valleys by controlling the polarization of light [120]. As a consequence, it is possible to create polarized LEDs in TMDC p-n junctions, where the electric field populates the carriers in the selected valley and the reversion of the field direction changes the polarization of the emitted light.

Finally, the strong Coulomb interaction allows for observation of trions in doped semiconducting TMDC monolayers. In comparison to conventional semiconductors these charged quasi-particles, combined either of two electrons and a hole or of two holes and an electron have high binding energies. They exhibit have valley selective optical properties and can be manipulated by electric fields.

4.1.3 Applications of semiconducting TMDC monolayers

Recently quite a few applications of 2D semiconducting TMDC materials were reported [121, 122, 123]. In Ref. [124] the authors report an observation of sharp emission lines at the edges of WSe_2, that reveal the effect of photon antibunching which is an attribute of single photon emitters.

By integration of WS_2 into a photonic microdisk cavity researchers from the Berkeley University demonstrated a monolayer excitonic laser [125]. The authors note that selective pumping in one set of two distinct valleys may lead to lasing in a confined valley that paves the way to the development of valley optoelectronics.

The demonstration of Schottky-diode-like solar cell is shown in Ref. [126]. In this experiment the monolayer of photoactive WS_2 was sandwiched between two graphene monolayers that played the role of electrodes. It was shown that the photocurrent strongly depends on illumination of the sample. Also, there are reports on the demonstration of ultrafast optical photodetectors [127].

The integration of 2D materials with external photonic structures allows enhancing light-matter interactions in monolayers. In particular, the use of optical cavities enables significant manipulation of optical density of states, which leads to the modification of emission and absorption properties. In Ref. [128] the authors integrate a graphene monolayer into a Fabry-Perot MC. This results in the 26-fold enhancement of light absorption. The use of intrinsic polaritonic resonances is another approach for enhancing the light-matter interaction. Plasmon-polaritons and phonon polaritons were demonstrated in graphene monolayer and in 2D hexagonal boron nitride. Exciton-polaritons were demonstrated in semiconducting TMDC monolayers. Recently, the physics of strong light–matter coupling between a single flake of MoS_2 and a cavity resonance in a Fabry–Perot resonator structure was discussed [129]. However, the comparably broad PL emission of the monolayer used for these findings (60 meV [129]), which was grown by chemical vapour deposition, render the unambiguous identification of the full characteristic polariton dispersion relation, in particular, in non-resonant PL experiments, challenging. The polariton formation with a single monolayer of $MoSe_2$ was subsequently demonstrated at cryogenic temperatures [130], enabled by its narrow linewidth (11 meV at 4 K and 35 meV at 300 K). Exfoliated WSe_2 monolayers exhibit comparable linewidths and have a strongly enhanced luminescence yield under ambient conditions [131], suggesting their suitability for room-temperature polaritonics. As discussed in Ref. [132], TMDC materials are good candidates to observe the room temperature Bose-Einstein condensate of exciton-polaritons, which is essential for technological applications. In the following sections a few experiments demonstrating exciton and polariton properties are reviewed.

4.2 Excitons in $MoSe_2$ monolayer

In this section the excitonic properties of $MoSe_2$ monolayers are considered in relation to three different photonic structures. Temperature dependent reflectivity measurements on a $MoSe_2$ monolayer are discussed in order to quantify the relevant temperature dependent parameters of the exciton resonance. In particular, the area of absorption resonance and the linewidth are studied in order to determine relative oscillator strength. In addition, these two parameters measured in the experiment are used to determine the strength of the exciton coupling with an optical mode in different optical structures, namely, open-cavities, Tamm-plasmon based devices and monolithic Bragg structures. All calculations are based on the coupled oscillator model and numerical transfer-matrix simulations. Finally, the polariton condensation phase diagram is calculated for $MoSe_2$ assuming the thermal equilibrium Bose-Einstein condensation in a finite size system, to elucidate the possibility of observing the polariton condensation at ambient conditions.

4.2.1 Experimental methods:

$MoSe_2$ monolayers were deposited onto 285 nm thermal oxide on Si wafers via conventional exfoliation from bulk $MoSe_2$ crystals. The SiO_2 thickness was chosen to be 285 nm to improve the monolayer contrast. Exfoliated MLs were characterized using Raman and P spectroscopy, and their thickness was determined via atomic force microscopy measurements. Micro-reflectivity spectra were taken under white-light illumination of a tungsten halogen lamp. The light source and setup cover a reliable spectral range from 1.5 to 2.2 eV. Following the convention of Refs. [133, 134] , the reflectance contrast $\Delta R/R$ was obtained according to $\Delta R/R = (R_{Sample} - R_{Substrate})/R_{Substrate}$ whereas R_{Sample} is the reflectivity of the monolayer on the substrate and $R_{Substrate}$ is the reflectivity of the uncovered substrate. The excitonic absorption manifests as Gaussian shaped signals in the reflectance contrast spectra. In order to deduce the energy, linewidth and amplitude of the absorption resonances, a background subtraction and fitting process was done. To ensure an appropriate background subtraction, transfer matrix calculations for the reflectivity background without excitonic absorption were carried out. Even though the acquired amplitude does not provide an absolute absorption value, the product of linewidth and amplitude is a quantity proportional to the exciton oscillator strength [120].

4.2.2 Theory

In order to calculate the Rabi splitting evolution with temperature ħΩ(T), two approaches were used. Firstly, the following equation, obtained with the coupled oscillator approach was used to account for the temperature-induced quenching of the Rabi-splitting via broadening of the excitonic resonance [135]:

$$\hbar\Omega(T) = \sqrt{V(T)^2 - \left(\frac{\Delta E_x(T) - \Delta E_c}{2}\right)^2}. \tag{4.2}$$

Here, $V(T)$ is the coupling strength, $\Delta E_x(T)$ is the exciton linewidth and ΔE_c is the cavity linewidth. $V(T)$ is a function of the oscillator strength $f(T)$, the effective cavity length L_{eff} and the effective number of individual monolayers in the cavity n_{eff}:

$$V(T) \sim \sqrt{\frac{f(T) * n_{eff}}{L_{eff}}}. \tag{4.3}$$

The initial values to carry on the simulation T = 4K for V= 36 meV and ΔE_c =1.6 meV were taken from reference [130]. Then, $\hbar\Omega(T)$ was calculated for higher temperatures using the measured relative values for $f(T)$ and $\Delta E_x(T)$. In addition, the visibility parameter ϑ was calculated according to:

$$\vartheta(T) = \frac{V(T)}{4(\Delta E_x(T) + \Delta E_c)}. \tag{4.4}$$

The value of $\vartheta(T)$ above 0.25 indicates that the strong coupling regime can be distinctively observed in transmission, reflectivity or PL spectra [136].

Secondly, the transfer matrix calculations were conducted for the reflectivity of a $MoSe_2$ monolayer, hypothetically integrated into the open cavity design described in Ref. [130]. The dielectric function $\varepsilon(\omega)$ of the $MoSe_2$ monolayer was modelled as a Lorentz oscillator:

$$\varepsilon(\omega) = \varepsilon_b + \frac{f(T)}{\omega_0^2(T) - \omega^2 - i\Delta E_x(T)\omega}. \tag{4.5}$$

Here ε_b is the background dielectric function and $\hbar\omega_0$ is the exciton energy. ε_b = 26 was taken from Ref. [137] and the initial value for $f(T)$ was adjusted to 0.4 to match the splitting calculated according to Eq.(4.2). The linewidth and the oscillator strength entering the expression for $\varepsilon(\omega)$ were adjusted for each temperature value according to the reflectivity results. The complex refractive index $\tilde{n}(\omega) = n + ik$ was derived from $\tilde{n}(\omega) = \sqrt{\varepsilon(\omega)}$ and used for the transfer matrix calculations. Finally, the reflectivity spectrum for each temperature is simulated with the respective refractive indices assuming a monolayer thickness of 0.65 nm. The splitting is deduced from the spectra and correlated with temperature.

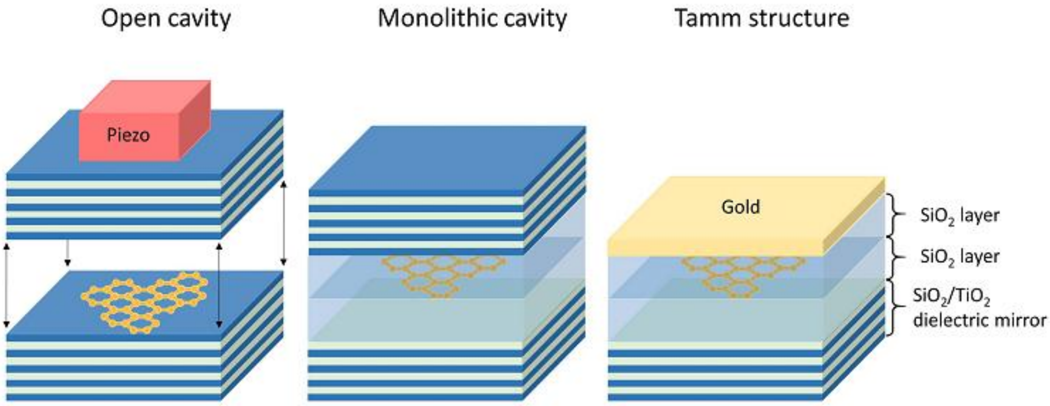

Figure 4.3: Schematic illustration of the open cavity design, a fully monolithic cavity and a Tamm plasmon structure. The cavity length can be adjusted in the open cavity approach by changing the vertical position of the top mirror indicated by the black arrows. Figure taken from Ref. [138].

In order to compare the open cavity design with other photonic architectures, the same dielectric functions were taken for additional transfer matrix calculations. All three considered photonic architectures are illustrated in Figure 4.3. The monolithic cavity mirrors consist each of eight TiO_2/SiO_2 layer pairs with $\frac{\lambda}{4n}$ thickness. The $MoSe_2$ monolayer is embedded between two $\frac{\lambda}{4n}$ SiO_2 layers, with thicknesses adjusted to tune the cavity mode in resonance with the exciton energy. The structure design that supports Tamm-plasmon modes consists of the identical bottom dielectric mirror, followed by a $SiO_2/MoSe_2$ ML/SiO_2 core and a 50 nm layer of gold on the top. Here again, the SiO_2 layer thicknesses were adjusted to ensure spectral resonance conditions. The resulting splitting was used to calculate the coupling strength V at 4K according to Eq.(4.2). Taking $f(T)$ into consideration, the visibility parameter evolutions $\vartheta(T)$ for the alternative cavity designs were calculated as well.

In order to check if the strong coupling regime could also lead to the polariton Bose-Einstein condensation, the approach discussed in Ref. [4] and in Section 1.2.1 was used to calculate a polariton phase diagram. The phase diagram provides an estimate of the critical polariton density N_C required for the polariton condensation at a given temperature T_C.

4.2.3 Experimental Results and discussion:

The micro-reflectivity spectra and their temperature evolution are the experimental basis for the following parameter deduction and calculations. Figure 4.4a presents a typical reflectance contrast spectrum of a $MoSe_2$ monolayer compared with its derivative for better feature identification. The peaks labelled A and B corresponding to excitons from the two spin-orbit split transitions at the K point of exciton are discussed.

The dependence of the A exciton feature on temperature is shown in Figure 4.4b. With increasing temperature, the distinct absorption at 1.653 eV shifts to lower energies, quenches in intensity and broadens. The evolution of energy, linewidth and amplitude with temperature are presented in Figure 4.5. The exciton energy decreases due to the thermal band gap narrowing, which is in good agreement with the PL temperature dependence [106], and it can be well fitted by the Varshni formula $E_g = E_0 - (\alpha T^2)/(T + \beta)$, where E_0 is the energy offset for T = 0 K and α and β are fitting parameters [139]. The fitting yields $E_0 = 1.653$ eV, $\alpha = 4.12 * 10^{-4}$ eV/K and β = 137.7 K, which is in a good agreement with previous results [140].

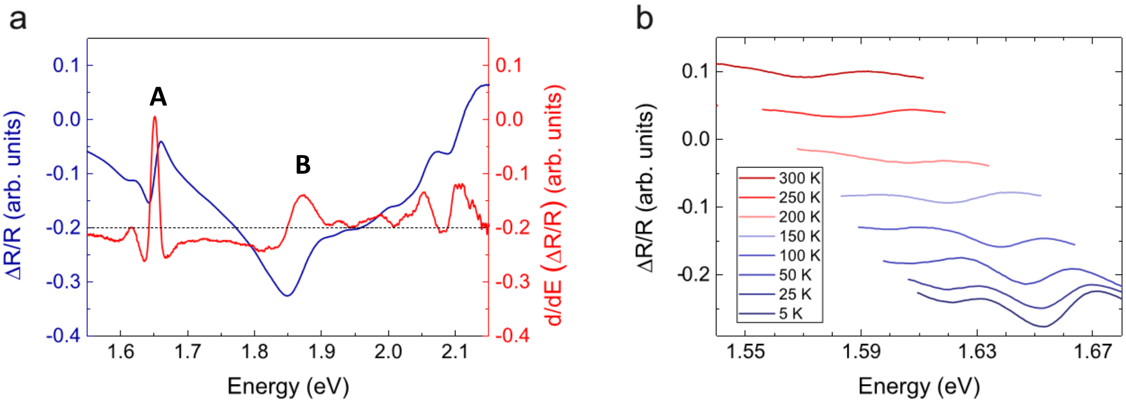

Figure 4.4: Reflectivity spectra of a $MoSe_2$ monolayer: (a) reflection contrast spectrum (blue) and its derivative (yellow). (b) reflection contrast spectra around the A exciton at various temperature between 5K and 300K. Figure taken from Ref. [138].

The linewidth exhibits a steady increase as a function of temperature, typical for the phonon-induced broadening mechanism. The initial linewidth at 4 K (19 meV) is broader than the one previously observed in PL (12 meV), whereas the linewidth at room temperature (33 meV) is in a good agreement with literature PL measurements (34 meV) [130]. However, as the linewidth depends on the substrate and charging condition of the monolayer, different observations are not necessarily in contradiction. Furthermore, the absorption linewidths were compared with PL linewidths that were taken from a smaller illumination area. Averaging over the larger illumination area of about 10 µm, potentially containing more defects or flake edges, can lead to absorption linewidth broadening. The linewidth broadening was fitted by

$$\Delta E_x(T) = \Delta E_{x,0} + \Delta E_{x,AP} * T + \Delta E_{x,OP} \frac{1}{e^{\frac{E_{LO}}{k_B T}} - 1} \qquad (4.6)$$

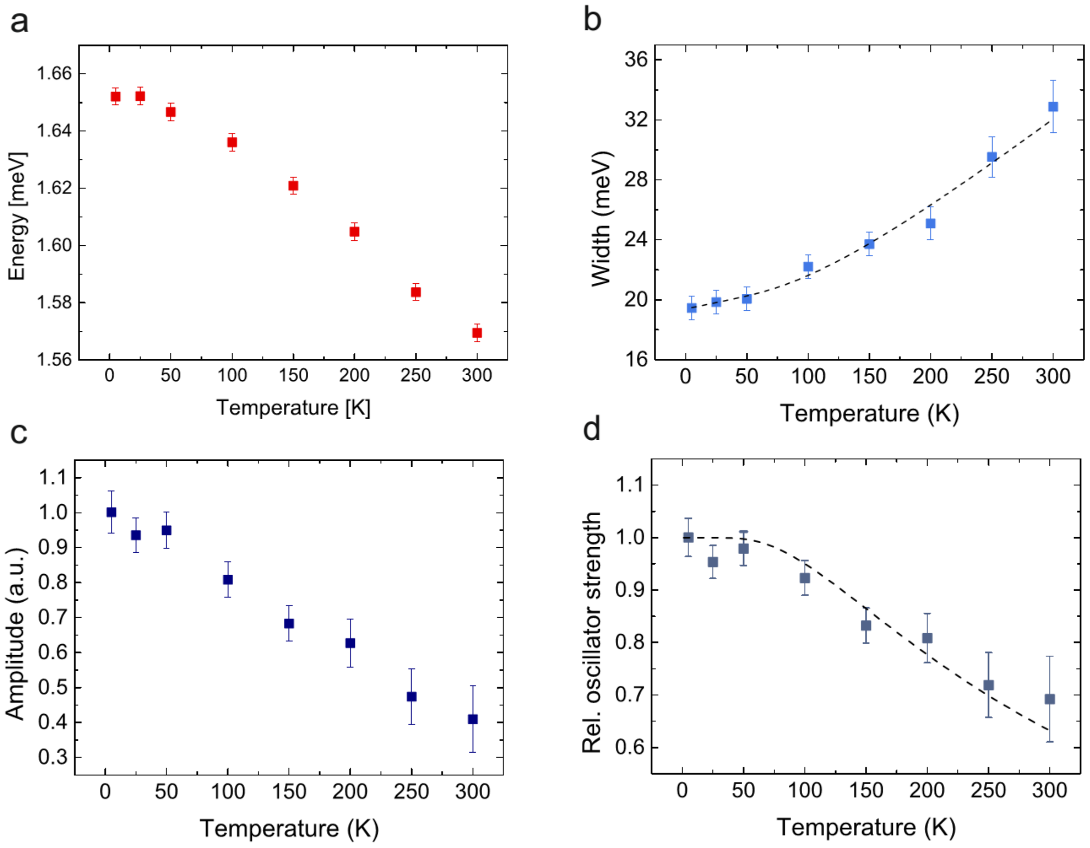

Figure 4.5: Temperature evolution of the deduced parameters energy (a), linewidth (b) and amplitude (c) and the normalized product of linewidth and amplitude (d), which were used in subsequent calculations. Figure taken from Ref. [138].

Here $\Delta E_{x,0}$ is the exciton linewidth at 0 K, $\Delta E_{x,AP}$ is the linear broadening constant attributed to the acoustic phonon dephasing [141], $\Delta E_{x,OP}$ is the optical phonon broadening constant and E_{LO} is the phonon energy of the longitudinal optical phonon. E_{LO} was fixed at 30 meV[44], which resulted in fitting parameters of $\Delta E_{x,0} = 19.4\, meV$, $E_{x,B} = 1.55 * 10^{-2} \frac{meV}{K}$ and $\Delta E_{x,OP} = 8.6\, meV$.

The amplitude drops almost linearly by 60% from 4K to 300K. This decrease is a natural consequence of the linewidth broadening. However, the product of amplitude and linewidth, a measure for the integrated absorption area, drops also steadily by 30% in the same temperature range, which suggests a temperature-induced decrease of the exciton oscillator strength. A comparable decrease in the oscillator strength with temperature has been observed in MoS_2 [120].

The oscillator strength of the exciton is determined by both the optical matrix element and the available bright exciton states. While the optical matrix element is not affected by the temperature, the available exciton states inside the light cone are functions of temperature. Therefore, the overall reduction of oscillator strength with temperature naturally follows from the reduced fraction of bright excitons at higher temperatures [142]. The remaining fraction occupies optically dark states. Excitons absorbed inside the light cone may thermalize and redistribute in the reciprocal space before being reemitted and thus contributing to the optical reflectivity. The temperature dependence of this effect stems from the temperature-induced decrease of the phonon scattering times in $MoSe_2$ monolayers [143]. The radiative decay rate Γ_0, which is proportional to the oscillator strength, enters the expression for the integrated absorbtion $\alpha = \frac{2\pi\Gamma_0\Gamma}{\Gamma+\Gamma_0}$ [135] and must be averaged over the exciton ensemble. Assuming the Boltzmann distribution of excitons, the radiative decay rate is estimated as $\Gamma_0(T) = \Gamma_0(T=0)[1 - \exp(-T_0/T)]$, where T_0 is the characteristic temperature dependent on the exciton frequency and effective mass [144]. The integrated absorption of light by excitons is linear in the averaged radiative decay rate provided that the radiative broadening is small compared to the non-radiative broadening. The last assumption is valid at temperatures above 100K [143]. Thus, the relative oscillator strength in Figure 4.5(d) can be fitted by the function $\Gamma_0 \sim 1 - \exp(-T_0/T)$, with $T_0 \approx 300K$. This is because the quantity plotted in Figure 4.5(d) is proportional to the radiative decay rate. Note that this temperature is significantly higher in $MoSe_2$ than those typical for large radii Wannier-Mott excitons in conventional semiconductor QWs [142].

The experimentally measured temperature evolution of the exciton linewidth and oscillator strength was used as an input for the Rabi splitting and the visibility calculations described in the theory section. The results of both these calculations, coupled oscillator approach (Eq.(4.2)) and the numerical transfer matrix simulation, are presented in Figure 4.6. The first approach results in low-temperature Rabi splitting value of 17.5 meV. This is in a good agreement with the experimentally acquired Rabi splitting of 20 meV from Ref. [130], which is not surprising as the input coupling strength was deduced from the experiment. The remaining difference is attributed to the broader exciton linewidth measured in our experiment and the negligence of the lateral mode confinement used in the reference cavity [130]. In the transfer matrix simulation, the oscillator strength (Eq. (4.3)) was adjusted in a way that the simulation result matches 17.5 meV. This procedure provides a realistic estimate for the exciton oscillator strength in monolayer $MoSe_2$, a requirement for the transfer matrix simulations. The Rabi splitting is consistent for both approaches up to 200 K. However, at higher temperatures the results obtained with the two methods deviate and the transfer matrix simulation yields the oscillator strength, which decreases more rapidly. This slight deviation stems from the simplifications in the coupled oscillator approach. The transfer matrix approach is more reliable, thus it is only used in the following calculations.

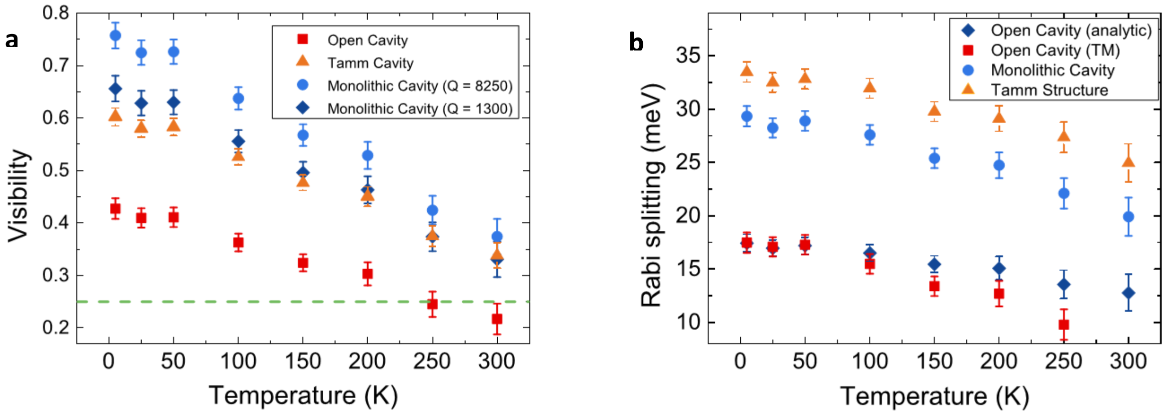

Figure 4.6: The temperature evolution of the visibility (a) and the Rabi splitting (b) for the open cavitiy design, the monolithic cavity and the Tamm plasmon design. a) The visibility evolution of a low Q monolithic cavity simulation is added (dark blue diamonds). The visibility limit of 0.25 is indicated by the green, dashed line. b)In addition, the analytic calculation for the open cavity design is presented (red squares). Figure taken from Ref. [138].

Yet, it should be noted that the calculated reflectivity spectrum for 250K does not exhibit two clearly distinguishable peaks anymore and the splitting can only be determined by fitting two Gaussian peaks to a broad reflectivity feature. For 300K no splitting can be determined from the simulated spectrum. Both observations are confirmed by the visibility parameter, which drops below 0.25. for temperatures above 250K. At lower temperatures the visibility remains well above 0.25, indicating that the system remains in the strong coupling regime.

The Rabi splitting for the monolithic cavity and for the Tamm plasmon sample is significantly higher (29.3 meV and 33.5 meV at 4K, respectively) and follows a similar decrease as for the open cavity (down to 19.9 meV and 25.0 meV at 300 K, respectively). The significant difference in monolithic and Tam cavities compared to the open cavity design is explained by a stronger mode confinement equivalent to a shorter effective cavity length (Eq. (4.3)). Although the monolithic cavity exhibits a lower Rabi splitting than the Tamm plasmon sample, the visibilities behave reversely (0.76 and 0.60 at 4 K, respectively) due to the narrower monolithic cavity linewidth of 0.2 meV compared to 8.4 meV for the Tamm plasmon structure. Nevertheless, the visibility evolutions of the Tamm structure and the monolithic cavity converge towards higher temperatures (0.34 and 0.37 at 300 K, respectively). In the Tamm plasmon design, the decrease in the oscillator strength does not affect the visibility to the same degree since it is strongly dependent on the cavity linewidth. Its broad linewidth can be also understood as the result of the comparatively low quality factor Q of the Tamm structure ($Q^{-1} = \frac{\Delta E_c}{E_{ph}}$, E_{ph} being the photonic mode energy), which is about 200 for the calculated structure. In contrast, the Q factors for open and monolithic cavity are 3600 (2050 [130]) and 8250, respectively. Despite of the large difference in Q-factor between the Tamm structure and the monolithic cavity, the visibility remains at a comparable level, because the cavity linewidth contribution is small for both structures compared to the higher excitonic linewidth contribution. In particular, at high temperatures, the latter contributes even more strongly, which reduces the difference between the Q factors even further. In order to illustrate the influence of the Q factor more clearly, the visibility of the monolithic cavity with a lower Q factor of 1300 is additionally simulated. This decrease stems from the reduction of the number of mirror pairs from ten to six. The resulting visibility evolution, plotted in Figure 4.6(a), shows a clear but small reduction in visibility. Overall, the calculated visibilities of the Tamm structure and the monolithic cavities reach comparable levels at room temperature, indicating that the mode volume is the more relevant parameter in this regime. This visibility level should be high enough to observe the strong coupling at room temperature. Nevertheless, the fabrication of both designs ensuring spectral resonance is more challenging than for the open cavity. The challenge lies in the overgrowth of the monolayer since conventional deposition methods such as sputtering can damage the monolayer. Nevertheless, this task appears achievable since TMDC monolayers have been successfully overgrown by dielectrics [145]. An additional step towards room temperature strong coupling could be the use of multiple, but distinctly separated monolayers as suggested by Dufferwiel et al., which increases the splitting by a factor of $\sqrt{N_{eff}}$.

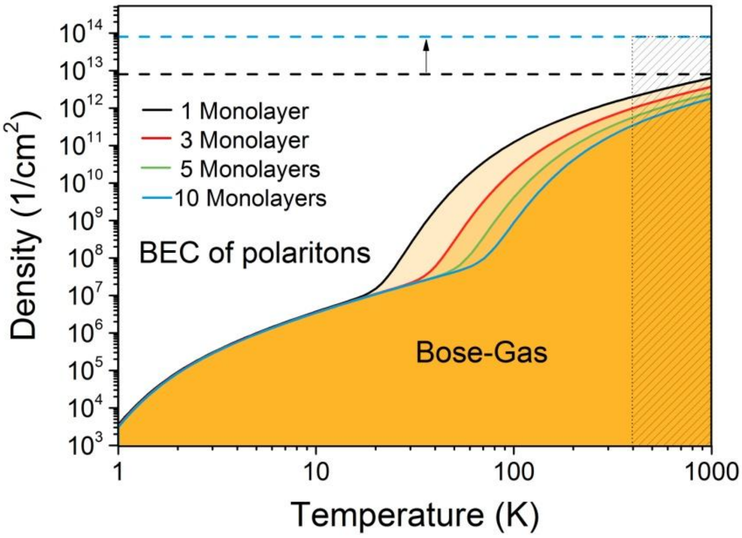

Figure 4.7: The phase diagram for a various numbers of $MoSe_2$ monolayers: Each solid line separates the Bose-gas regime from polariton condensation regime according to Eq.(1.53). The upper density limit for polariton condensation is given by the Mott density (dashed lines for one (black) and ten monolayers (blue), respectively). The upper temperature limit depends on the strong coupling requirements ($\vartheta > 0.25$), indicated by the shaded area above 400 K (estimated temperature limit for one monolayer). Figure taken from Ref. [138].

The calculated phase diagram is presented in Figure 4.7. It shows the critical polariton density for different numbers of $MoSe_2$ monolayers in the system. At T= 1K the density is as low as 3.5×10^{3} cm^{-2}, independent of the ML number. However, at room temperature, it is possible to decrease the critical density from 1.4×10^{12} cm^{-2} to 1.8×10^{11} cm^{-2} by varying from one to ten monolayers due to the increased Rabi splitting, which results in a reduction of the effective polariton mass. Simultaneously, the upper limit (Mott density) rises significantly from 8×10^{12} cm^{-2} for one ML and up to 8×10^{13} cm^{-2} for ten MLs. The comparably high Mott density is due to the small Bohr radius of 2 nm in our system. These calculations assume the following parameters: $m_{ph} = 10^{-5}\, m_e$, $\mu = 0.4\, m_e$, $L = 10\, \mu m$, $a_B = 2\, nm$. Rabi splitting for 1 monolayer is taken to be 20 meV. Even more importantly, the upper temperature limit is not defined by the exciton binding energy as for excitons in GaAs (on the order of 100 K), but only by the strong coupling conditions (the temperature for thermal exciton breaking can be expected to be above the decomposition temperature of the monolayer). It is shown that the strong coupling threshold depends on the thermal broadening of the exciton linewidth, the thermal decrease of the oscillator strength and the cavity design. Here a visibility value of 0.25 was used as an indicator for the strong coupling threshold, which yields 250 K for the open cavity design and 400 K (linear extrapolation of the visibility evolution) for both the monolithic cavity and the Tamm plasmon design. For multiple monolayers integrated into any of the structures this limit will further increase as indicated by the shaded area in Figure 4.7. As a result, the phase field for polariton condensation enlarges significantly. Most importantly, the critical polariton condensation density for one monolayer is only 9×10^{11} cm^{-2} at 300 K, which is well below the Mott density. For multiple monolayers the range between critical condensation density and Mott density increases even further. From these considerations, it seems feasible that polariton condensation may be observed at room temperature. It is essential to point out that additional parameters such as exciton lifetime, exciton quantum efficiency, exciton-phonon scattering rate will play a crucial role in achieving a critical polariton density.

4.3 The interplay between excitons and trions in a monolayer of MoSe$_2$

4.3.1 Experimental observations

Trions are charged quasi-particles, combined of two electrons and a hole (X^-) or two holes and an electron (X^+). At first these complexes were discussed theoretically in [146, 147] and observed experimentally in CdTe QWs. In conventional semiconductors trion binding energy that is defined as the energy, required to split the trion into a neutral exciton and an unbound electron or hole, reaches the value of several meV, while the exciton binding energy is several tens of meV. Recent experiments in TMDC monolayers showed that not only exciton binding energy increases significantly, but trion binding energy rises up to 30 meV.

In this section the influence of free carriers in the monolayer on exciton and trion binding energies is discussed. In the experiment monolayers of $MoSe_2$ were deposited onto 285 nm thermal oxide on Si wafers via conventional exfoliation from bulk crystals. PL spectra were recorded at 5 K, via non-resonant monolayer excitation. The excitation laser is utilized to create excitons and trions in the monolayer as well as to activate additional carriers in the heterostructure. The amount of photodoping was increased at cryogenic temperatures, using higher excitation powers and longer optical illumination times, which is a realistic configuration for polariton experiments in the non-linear regime. The changes in the trion dissociation energy of the order of several meV were observed, which reflects that both the exciton and the trion binding energies in $MoSe_2$ sensibly depend on the excess carrier density in the monolayer.

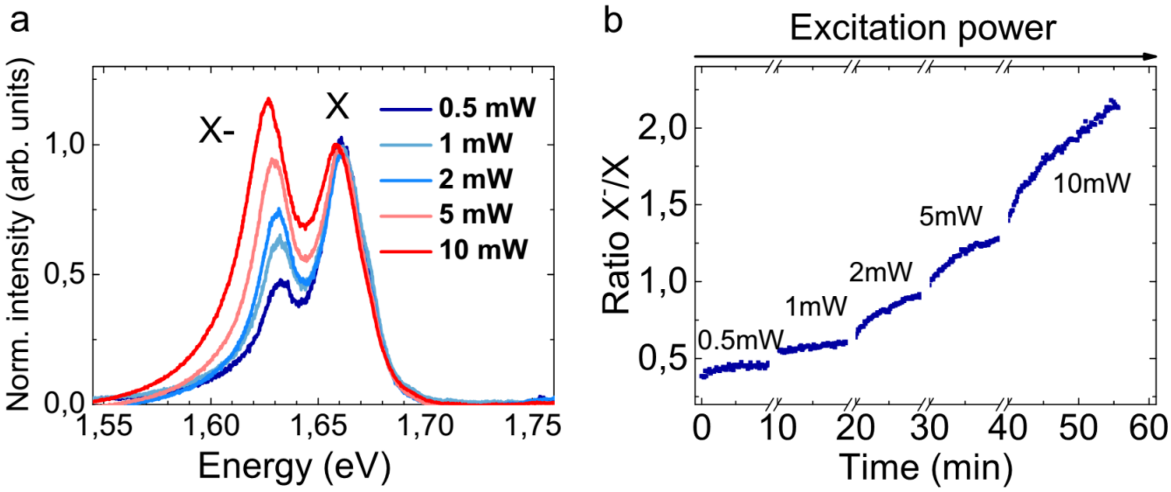

Figure 4.8: (a) Power series of PL spectra normalized to the excitonic resonance. (b) Ratio of integrated peak intensities as a function of time and excitation power.
Figure taken from [148].

Figure 4.8(a) shows the power dependent PL emission of the exciton and trion complexes. Each spectrum is normalised to the excitonic signal. One can see that the trion dominance increases with the excitation power and the non-resonant pump laser induces additional electrons in the sample, which favours the formation of trionic complexes. Another way to generate free carriers in the monolayer, which is more controllable, is the adjusting of illumination time of the monolayer. This method is rather effective, because the photoexcitation process of additional free carriers takes place on a very slow timescale. Figure 4.8(b) shows the ratio of integrated peak intensities as a function of time and excitation power. At the smallest excitation powers the exciton PL signal is still dominating the spectrum. However, even with constant pump power, the X^-/X fraction is already monotonously increasing with time, exhibiting a saturation behaviour. This indicates a self-limiting activation process, typical for the successive activation of a finite number of defect states. An increase in the pump power then leads to a further increase of this ratio, which serves as a proportional measure for the number of electrons per exciton in the system.

The evolution of the energies of both the exciton and the trion as a function of the exposure time are subject to a step-wise increase of the pump power shown in Figure 4.10(a). One can see that as the excitation power is increased, both the X and the X- signal experience a similar red-shift, resulting from the power-induced renormalization of the band gap of the monolayer. The contribution of the microscopic processes of this renormalization are not fully determined (dielectric screening vs. sample heating), however are of a minor importance in this study, since the energy scale is approximately two orders of magnitude smaller than the correlation energies of the excitonic complexes. Another effect, which can be directly observed in Figure 4.10(a) is the shift of both the X and X- signal as the pump laser intensity is kept at the same level. Here, the behaviour of both resonances is fundamentally different: as the pump intensity is kept constant and charges successively accumulate in the monolayer, the X feature is subject to a continuous blueshift in energy, whereas the X- feature is redshifted by a similar magnitude (hundreds of µeV up to one meV). The blueshift of the exciton in the presence of an accumulating electron gas is a signature of a renormalization of the exciton binding energy. In the presence of additional screening, the Coulomb coupling between electrons and holes is reduced and the excitonic emission energy eventually approaches the free carrier band gap.

Due to the pump powers, yielding exciton densities well below the Mott density in $MoSe_2$ monolayers (around 10^{13}-10^{14} carriers /cm^2, as was defined in Section 4.2) the shift of the exciton in the experiment is significantly smaller than the exciton binding energy

The redshift of the energy of the trion, on the other hand, is a strong indication that the trion binding energy is enhanced by the electron reservoir, which over-compensates the screening induced blueshift of the exciton. In order to directly correlate the trion dissociation energy with the approximate number of excess carriers per exciton, the energy $(E_X - E_{X^-})$ is plotted as a function of the X-/X ratio in Figure 4.10(b). One can see that trion dissociation energy appears to be linear function of the intensity ratio between X- and X, and thus of the number of electrons in the monolayer.

4.3.2 Theory

A qualitative explanation of the increase of the trion binding energy in QWs was given in Ref. [149] in relation to the experiments on the absorption of light in a CdTe QW, containing a 2DEG. The separation between trion and exciton peaks turned out to be linear in n_e: $E_X - E_{tr} = E_b^{tr} + cE_F$ with $c \approx 1$. Here E_b^{tr} is the trion binding energy, and E_F is the electron Fermi energy calculated from the bottom of the conduction band. An exciton is considered as an ionized trion. The energy that is needed to remove one electron from the trion is equal to E_b^{tr} in the limit

$n_e \rightarrow 0$ and $E_b^{tr} + E_F$ at finite electron densities, due to the fact that one electron should be moved up in energy to the Fermi level while all lower conduction band states are occupied. Thus, this effect stems from the combined effect of the Pauli exclusion principle and many-body interactions. Investigations done in Refs. [120, 150] confirm this linear dependence of the trion binding energy in TMDC monolayers with small differences in estimations of coefficient c. In this discussion, as in the experiment described above, it is assumed that the trion is negatively charged due to the residual n-type doping commonly observed in TMDC monolayers. The model [149] fails to describe the behaviour of the exciton-trion energy splitting in the limit of high concentrations of free electrons, where it predicts unphysical negative values. In order to reproduce the experimental data taken in a wide range of free electron densities one needs to go beyond the oversimplified model [149] and calculate separately the exciton and trion binding energies, see e.g. [120]. Here the variational approach is used for the calculation of exciton and trion states that has an advantage of simplicity and still captures the behaviour of the system both at low and high electronic densities.

4.3.2.1 The variational method

The variational approach is based on the minimization of a solution of Schrödinger equation with a trial wave-function that depends on a parameter.

The Schrödinger equation for the wave function $\Psi(\rho)$ of the electron-hole relative motion in the plane of the layer in cylindrical coordinates reads:

$$\left[\frac{-\hbar^2}{2\mu}\frac{1}{\rho}\frac{\partial}{\partial\rho}\left(\rho\frac{\partial}{\partial\rho}\right) - \int_0^\infty J_0(k\rho)V_C k dk - E_{ex}\right]\Psi(\rho) = 0, \qquad (4.7)$$

where $\mu = \frac{m_e m_h}{m_e + m_h}$ is the reduced mass of electron-hole relative motion, $J_0(k\rho)$ is the zeroth order Bessel function, V_C is the screened Coulomb potential.

Here the free carriers are described as a degenerate Fermi gas at zero temperature. The exclusion effect associated with the phase space filling is taken into account. All electronic states below the Fermi level are assumed to be occupied, which is why they cannot contribute to the exciton state. Taking into account this exclusion effect the trial function of the exciton can be written in the form [151]:

$$\Psi(\rho) = \int_0^\infty J_0(k\rho) f(k) k dk, \qquad (4.8)$$

$$f(k) = \frac{B}{(A + k^2)^{\frac{3}{2}}}\Theta(k - k_F), \qquad (4.9)$$

where $\Theta(k-k_F)$is the Heaviside function, $k_F=\sqrt{2\pi n_{2D}}$, n_{2D} is the density of free carriers, A is a variational parameter, inversely proportional to squared exciton Bohr radius. Formula (4.8) is the Hankel transform analogous to the Fourier transform in Cartesian coordinates. B can be found from the normalization condition:

$$2\pi\int_0^\infty \Psi(\rho)^2\rho d\rho=1. \tag{4.10}$$

In the limiting case of $n_{2D}=0$ the introduced wave function reduces to the hydrogen-like wave function:

$$\Psi(\rho)=\sqrt{\frac{2}{\pi}\frac{1}{a}}exp\left(-\frac{\rho}{a}\right), \tag{4.11}$$

where a is the exciton Bohr radius. Varying the parameter A the exciton binding energy can be found as the minimum value of E_{ex}, where:

$$E_{ex}=2\pi\int\limits_0^\infty \Psi(\rho)\left[\frac{-\hbar^2}{2\mu}\frac{1}{\rho}\frac{\partial}{\partial\rho}\left(\rho\frac{\partial}{\partial\rho}\right)-\int\limits_0^\infty J_0(k\rho)V_C k dk\right]\Psi(\rho)\rho d\rho. \tag{4.12}$$

4.3.2.2 Trion wave function

For the trion case the problem can be simplified: one can assume that the two electrons (We consider a negatively charged trion X$^-$ to be specific, while the X$^+$ case can be considered without loss of generality) are in the singlet state so that they are characterized by orthogonal spin functions and identical spatial wave functions. The trion binding energy may be found as the solution of the Coulomb problem with a hole of charge $+e$ and mass m_h and an electron pair of charge $-2e$ and mass $2m_e$. In this case the trion wave function can be expressed as a sum of two parts, corresponding to the electrons composed by the states that lie below and above the Fermi level respectively:

$$\Psi(\rho)=\int_0^\infty J_0(k\rho)f_{tr}(k)kdk \tag{4.13}$$

$$f_{tr}(k)=\frac{B}{(A+k^2)^{\frac{3}{2}}}\Theta(k-k_F)+\frac{C}{(D+k^2)^{\frac{3}{2}}}\Theta(k_F-k), \tag{4.14}$$

where A and D are variational parameters and B, C can be found from normalization conditions. Here the exclusion principle is taken into account for both electrons: the photoexcited electron can only be formed by free states, while the resident electron can only be taken from the states below the Fermi level. The good estimate for the trion binding energy is found in a similar manner as in Ref. [152] by minimization over both variational parameters A and D.

4.3.2.3 Screened Coulomb Interaction in thin films:

The standard screened interaction potential in 2D case reads:

$$\varphi_C(k) = \frac{e}{\varepsilon(k + \kappa_s)}. \tag{4.15}$$

here e is the electric charge, ε is the dielectric constant of the medium, κ_s is the screening constant, that is defined as $\kappa_s = \frac{2g_v m_e e^2}{\varepsilon\hbar^2}$, with g_v being the valley degeneracy factor and m_e being the electron mass.

However, two effects are not taken into account: firstly this expression yields an unphysical result that the screening is independent on the density of free carriers, which means that the electrons at low densities screen as effectively as at high density. Another effect that is not taken into account is the screening dependence on the thickness of the layer.

The screening dependence on the thickness of the layer was discussed in Ref. [153, 154]. It was shown that with the decrease of the thickness of a film, placed in between two media with dielectric constants, that are much lower that the dielectric constant of the film, the Coulomb interaction between holes and electrons significantly increases. In the case where the distance between two charges ρ is longer than the thickness of the layer, the interaction potential takes the form:

$$V_c(\rho) = \frac{\pi e e'}{\varepsilon d}\left[H_0\left(\frac{\varepsilon_1 + \varepsilon_2}{\varepsilon}\frac{\rho}{d}\right) - Y_0\left(\frac{\varepsilon_1 + \varepsilon_2}{\varepsilon}\frac{\rho}{d}\right)\right], \tag{4.16}$$

where ε is the dielectric constant of the monolayer, ε_1 and ε_2 are the dielectric constants of surrounding media, e.g. substrate and vacuum, d is the thickness of the layer. This potential takes into account the strong contrast in dielectric constants and is valid in the case where d is much shorter than the exciton Bohr radius and the dielectric constants of the surrounding media are much lower than the dielectric constant of the monolayer.

In the more general case, the interaction potential can be found by solving the Poisson equation in the reciprocal space, where the interaction potential takes the form:

$$\varphi_C(k) = \frac{e}{\varepsilon(k)k}, \tag{4.17}$$

where $\varepsilon(k) = 1 + 2\pi\chi_{2D}k$ is the dielectric function that is dependent on the wave vector in the 2D case, χ_{2D} - is polarizability of 2D layer. The Hankel transform of this potential results in the following interaction in the direct space:

$$V_{\mathrm{sc}}(\rho) = \frac{e^2}{4\chi_{2D}}\left[H_0\left(\frac{\rho}{r_0}\right) - Y_0\left(\frac{\rho}{r_0}\right)\right], \tag{4.18}$$

where the parameter $r_0 = 2\pi\chi_{2D}$ has the dimensionality of length and depends on the polarizability of the system, H_0 and Y_0 are Struve and Neumann functions, respectively.

The asymptotic properties of Struve and Bessel functions allow representation of the interaction (4.18) in the form:

$$\lim_{\rho\to\infty} V_{sc}(\rho) \sim \frac{1}{\rho}, \tag{4.19}$$

$$\lim_{\rho\to 0} V_{sc}(\rho) \sim -\frac{1}{r_0}\left[\ln\left(\frac{\rho}{2r_0}\right) + C\right], \tag{4.20}$$

where $C \approx 0.577$ is the Euler constant. The interaction that takes into account both asymptotic forms reads:

$$V_{sc}'(\rho) = -\frac{1}{r_0}\left[\ln\left(\frac{\rho}{\rho + r_0}\right) + (C + \ln 2)e^{-\frac{\rho}{r_0}}\right]. \tag{4.21}$$

In the limit $\rho \gg r_0$ the effective potential acts as an unscreened 3D Coulomb potential, while in the opposite limit $\rho \to 0$ it weakens logarithmically.

Also, one can see that the logarithmic divergence in the expression (4.21) weakens with the increase of polarizability, which means that the screening is more effective for highly polarisable systems.

In order to take into account the presence of free carriers in the system, one should modify the dielectric function $\varepsilon(k)$. For simplicity it is instructive to discuss its modification in the reciprocal space. In general, in the system, where the layer with electrons is sandwiched between an insulator and a semiconductor, the polarizability χ_{2D} becomes intrinsically dependent on the wave vector [155] and the dielectric function becomes nonlocal and takes the form of a dielectric tensor [156, 157]. This modification affects the parameter r_0 in the formula (4.18) and the total expression for the interaction becomes relatively cumbersome. However, in the case where the doped semiconductor is placed into homogeneous media with homogeneous dielectric constant, the expression for the dielectric tensor can be simplified. To be explicit the dielectric function can be taken in the form [155]:

$$\varepsilon(k)=\begin{cases}\varepsilon\left(1+\dfrac{\kappa_s}{k}\right), & k\leq 2k_F\\ \varepsilon\left(1+\dfrac{\kappa_s}{k}\left[1-\left[1-\left[\dfrac{2k_F}{k}\right]^2\right]^{1/2}\right]\right), & k>2k_F,\end{cases}\qquad(4.22)$$

It can be seen, that for small wave vectors the screening remains the same, while at k >2k_F the screening effect falls off much more intensively. As k_F tends to zero with the density of free carriers, the screening affects smaller range of wave vectors k. The modified screened Coulomb interaction V_C in the reciprocal space, that takes this modification into account, reads:

$$V_C=\frac{e^2}{\varepsilon' k\left(1+\left(\frac{\kappa_s}{k}\right)\right)\left(1-\Theta(k-2k_F)\sqrt{1-(2k_F/k)^2}\right)},\qquad(4.23)$$

Here ε' is the mean dielectric constant that takes into account the substrate. In this expression the direct layer thickness dependence is disregarded.

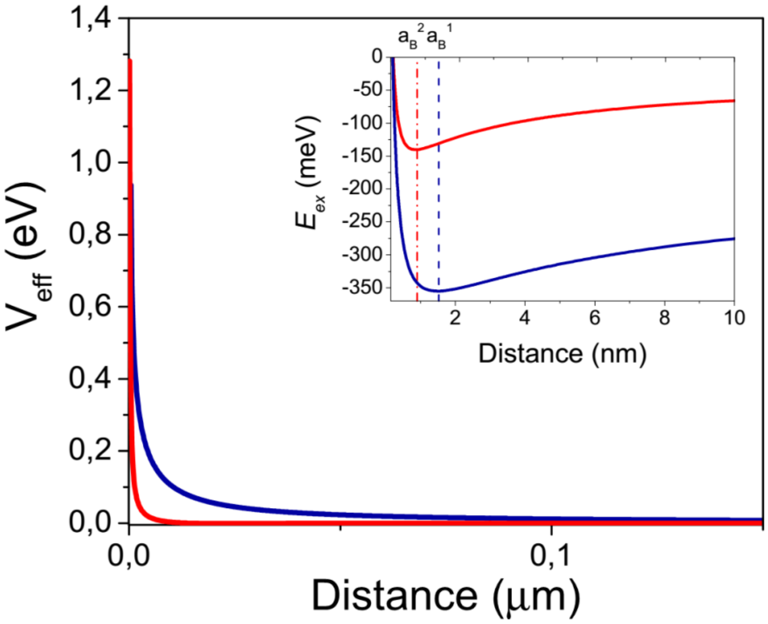

Figure 4.9: The comparison of interaction energies given in the form (4.16) (blue curve)and Hankel transform of formula (4.23) (red curve). The free carrier density, used in the calculation is n_{2D}=10 cm. The inset demonstrates the exciton energy (4.12) calculated by variational approach, where the minimum represents exciton binding energy. The corresponding coordinate is exciton Bohr radius.

Figure 4.9 shows the screened Coulomb interaction in the form of the potential (4.18), that takes into account only the thickness of a monolayer (red curve), the Hankel transformation of interaction (4.23) (blue curve), and corresponding exciton energies, calculated by the variational approach. As discussed above, to define the interaction, that accounts for both effects simultaneously, one should separately calculate the polarizability and use the formula (4.18), or, alternatively, use r_0 as a fitting parameter. One can see from the inset of Figure 4.9, that in the absence of free carriers the variational approach yields the value of exciton binding energy E_B =

350 meV, that is slightly below the generally accepted value of ~ 400 meV. This discrepancy may stem from the drawbacks of the computational technique.

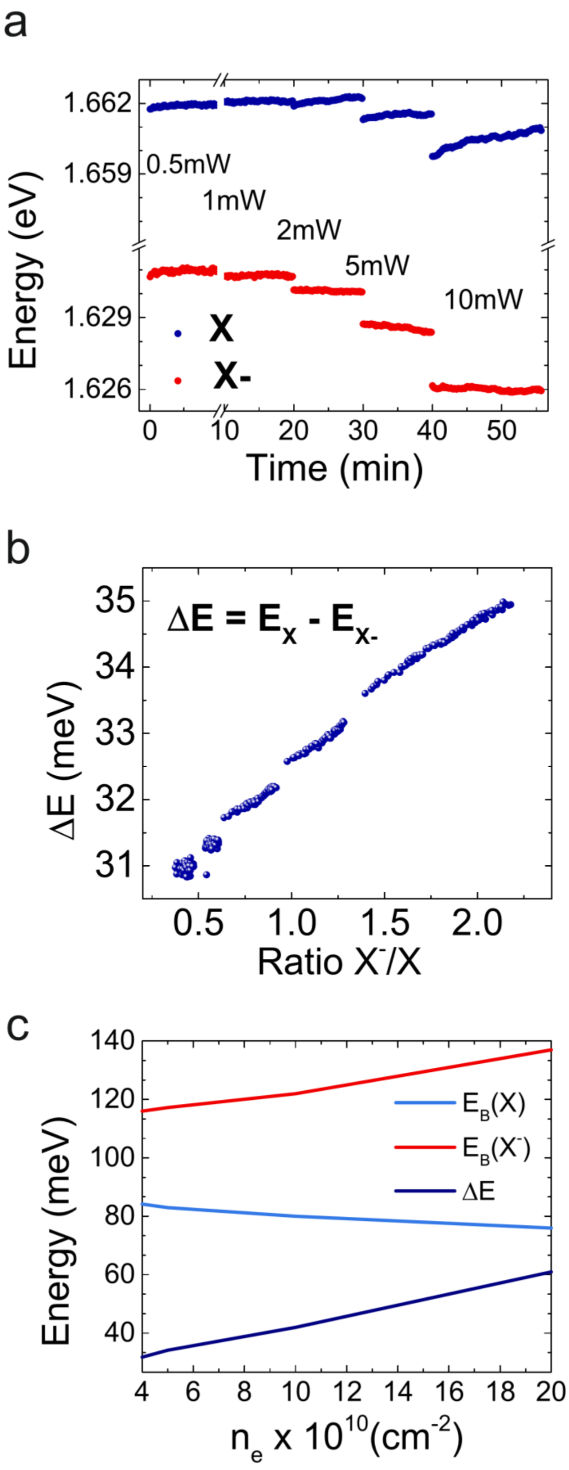

Figure 4.10: (a) Evolution of excition and trion energy with illumination time and excitation power. (b) Trion dissociation energy as a function of X-/X ratio. (c) Calculated binding energy of X and X- modelled with the variational approach. $E_B(X)$ is he exciton binding energy, $E_B(X^-)$ is the trion peak energy calculated from the bottom of conduction band. The difference ΔE is the trion binding energy. Figure taken from [148].

4.3.3 Experimental results and discussion

The described method was used to estimate the exciton and trion binding energies in a $MoSe_2$ monolayer. The following parameters were used in the calculations: $m_{el} = 0.7m_0$, $m_h = 0.5m_0$, $\varepsilon = 11$, that averages monolayer dielectric constant and the substrate dielectric constant. In the experiment it is essential to take the presence of free carriers into account, so the interaction (4.23) is used in calculations. The results for exciton and trion binding energies at different electron densities calculated with the described model are shown in Figure 4.10(c). Trion binding energy changes linearly with the density. It can be seen that the binding energies in the presence of free carriers calculated with this approach are somewhat lower than the experimental values for $MoSe_2$. However, the model qualitatively agrees with experiment.

4.3.4 Perspectives

The described model of variational approach that is used to calculate the trion binding energy has its advantages, because it takes into account the phase space filling. However, in general the discussed model is oversimplified, because it is built on the assumption that for a singlet spin configuration two electrons in a trion can share the same coordinate-dependent wave-function like in He atoms, or double charged quantum dots. The major drawback of the model is that the effective exciton approach does not take into account correlations between two electrons in the trion, as well as Coulomb repulsion.

Commonly, the full trion Hamiltonian in real space reads:

$$H_{tr} = -\frac{\hbar^2}{2\mu}\left(\nabla^2_{\boldsymbol{\rho}1} + \nabla^2_{\boldsymbol{\rho}2}\right) - \frac{\hbar^2}{m_h^*}\nabla_{\boldsymbol{\rho}1} \cdot \nabla_{\boldsymbol{\rho}2} - V_C(\rho_1) - V_C(\rho_2) + V_C(|\boldsymbol{\rho_1} - \boldsymbol{\rho_2}|), \quad (4.24)$$

where $\boldsymbol{\rho}_1 = \boldsymbol{\rho}^1_{el} - \boldsymbol{\rho}_m$, $\boldsymbol{\rho}_2 = \boldsymbol{\rho}^2_{el} - \boldsymbol{\rho}_m$, m_h^* is a single hole effective mass [158]. In Refs. [159, 160, 161] the authors calculate the excitonic spectrum and trion binding energy within this model with the interaction potential (4.18). However, the screening is introduced only as a free parameter $r_0 = 2\pi\chi_{2D}$, where χ_{2D} is the polarizability of the system. In general, the screening in TMDC monolayers is dynamical and there is no simple way to take it into account.

So finally there is a room for further development of the theory, for example it will be instructive to provide the comparison between two models and to develop the approach, which allows for correct estimation of screening effects.

The possible experimental applications would be the development of lasers based on trion or trion-polariton modes. For example, under applied magnetic field it is possible to create the equidistant ladder of energy levels for trion-polaritons, which, in principle, can be used for the creation of the THz cascade laser.

4.4 Polaritons in WSe_2 monolayer

In this section the experiment on observation of plasmon-polaritons in a Tamm-plasmon structure is discussed. In order to demonstrate the strong coupling regime at ambient conditions the WSe_2 monolayer was embedded in a compact Tamm-plasmon photonic microstructure, composed of a dielectric distributed Bragg reflector (DBR), a polymer layer and a thin gold cap. In this experiment the characteristic energy–momentum dispersion relations of the upper and the lower polariton branch at ambient conditions are mapped out by angle-resolved PL and reflection measurements. This is the first observation of the strong coupling regime in WSe_2 monolayer.

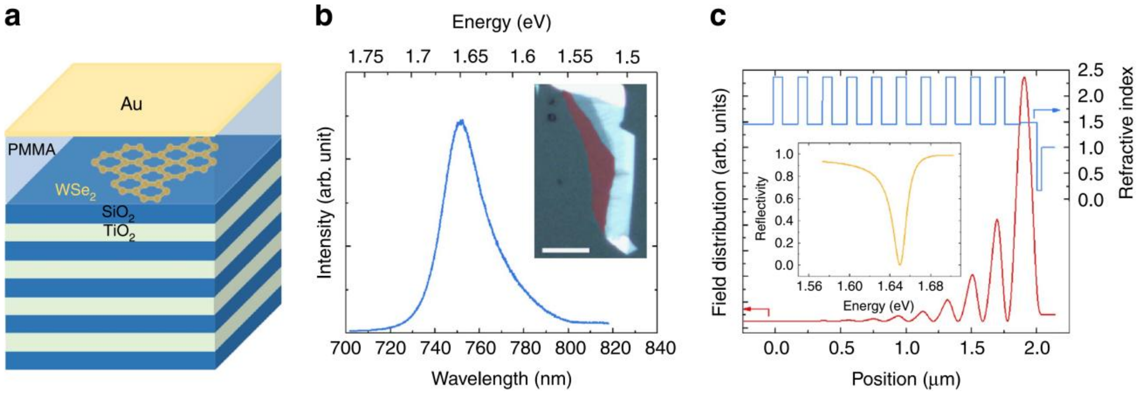

Figure 4.11: Tamm-monolayer device. (a) Schematic illustration of the Tamm-plasmon device with the embedded WSe_2 monolayer. The monolayer is capped with a polymer, whose thickness primarily determines the frequency of the device's optical resonance. (b) PL spectrum of the WSe_2 monolayer before capping, recorded under ambient conditions. The dominant emission is identified to stem from the A-valley exciton. Inset: false-colour optical microscopy image of the used WSe_2 flake (monolayer in red shaded area; scale bar, 20 mm). (c) Calculation of the electromagnetic field intensity in the heterostructure and the optical resonance (inset). The Tamm-plasmon features a strongly enhanced field maximum close to the surface of the structure, which coincides with the vertical position of the monolayer in the device.
Figure taken from Ref. [107].

Figure 4.11 shows a sketch of the device, employed in the experiment – (a), the characteristic profile from the A-valley exciton with a linewidth of 37.5 meV – (b), and the vertical optical mode profile obtained by a transfer matrix calculation, the corresponding refractive indices of the layer sequence and the resulting reflectivity spectrum without embedded monolayer – (c). The sample was held at 300 K and angle-resolved PL spectra was studied. The embedded monolayer was excited via a non-resonant continuous wave laser at a wavelength of 532 nm at an excitation power of 3 mW.

In Figure 4.12(a) the PL spectra extracted from the device at various in-plane momenta are presented. At an in-plane momentum of 1.84 μm^{-1} (corresponding to an emission angle of 12.67°), a minimum peak distance between the two prominent features was observed which was identified as the lower and upper polariton branch. These two branches feature the characteristic anti-crossing behaviour with a Rabi splitting of 23.5 meV, the key signature of the strong coupling regime. This strong coupling regime is primarily a result of the tight mode confinement provided by the Tamm-structure. Figure 4.12(b) depicts the fully mapped out energy-momentum dispersion relation of the two polariton resonances by plotting the corresponding peak energies as a function of the in-plane momentum. As expected for coupled oscillators with different effective masses, the characteristic potential minimum was observed in the lower polariton branch with a modest negative detuning of $\Delta = E_C - E_X$ = -11.7 meV. This negative detuning condition leads to an effective polariton mass of 1.45×10^{-5} m_e at the bottom of the lower polariton, where m_e is the free electron mass. Furthermore, the characteristic transition from a light particle close to $k_{||} = 0$ to a heavy, exciton-like particle at large $k_{||}$ values can be observed. The corresponding Hopfield coefficients, which characterize the excitonic and photonic fraction of the lower polariton ($|X|^2$ vs. $|C|^2$, respectively) are plotted as a function of the in-plane momentum in Figure 4.12(c). The potential minimum, which is formed in the lower polariton branch, is another key signature of an exciton-polariton in the presence of vertically confined field. It furthermore provides a well-defined final energy state with a distinct effective mass, which is crucial for advanced parametric and stimulated scattering experiments [162]. A key advantage of exciton polaritons, as compared to other composite bosons (such as excitons), is the possibility to conveniently tune the depth of this attractive potential, and simultaneously the particles' effective masses as well as light-versus-matter composition by changing the detuning between the light and the matter oscillators. In addition, reflectivity measurements were carried out in the experiment to provide further evidence that the device worked in the strong coupling regime. The results are presented in Figure 4.12(d) and were analyzed and fitted the same way as for the PL data. Similarly compared to the PL experiment, there is a clear appearance of two normal modes that can be well described by the coupled oscillator model.

For the sake of clarity, the reflectivity spectra is inverted, thus the reflection dips appear as positive signals in the graph. In Figure 4.12(e) the graph shows the extracted values of the reflection resonances as a function of the in-plane momentum, which allows reconstructing the polariton dispersion relation. The dispersion features the characteristic avoided crossing behaviour with a Rabi splitting of 14.7 meV.

In order to interpret the experimental data, the dispersions were fitted with the coupled oscillator model:

$$\begin{bmatrix} E_{ph} + i\hbar\Gamma_{\mathrm{ph}} & \hbar\Omega/2 \\ \hbar\Omega/2 & E_{ex} + i\hbar\Gamma_{\mathrm{ex}} + \Delta \end{bmatrix} \begin{bmatrix} \alpha \\ \beta \end{bmatrix} = E \begin{bmatrix} \alpha \\ \beta \end{bmatrix}, \tag{4.25}$$

where E_{ph} and E_{ex} are the photon and exciton energies, respectively, Δ is the detuning between the two modes, Γ_{ph} and Γ_{ex} are the photon and the exciton mode broadening.

The eigenvectors represent the weighting coefficients of exciton and photon fraction and $\hbar\Omega$ represents the Rabi splitting in the system. Solving the dispersion equation:

$$det\begin{bmatrix} E_{ph}+i\hbar\Gamma_{\mathrm{ph}}-\mathrm{E} & \hbar\Omega/2 \\ \hbar\Omega/2 & E_{ex}+i\hbar\Gamma_{\mathrm{ex}}+\Delta-\mathrm{E} \end{bmatrix}\begin{bmatrix}\alpha \\ \beta\end{bmatrix}=0, \qquad (4.26)$$

one can obtain two polariton branches. The result of this modelling is shown in Figure 4.12(b) and Figure 4.12(c) (solid lines) along with the experimental data (symbols). The fitting was carried out via solving the optimization problem with detuning, Rabi splitting and photon mass used as parameters. As the exciton mass is several orders of magnitude larger than the photon mass, it does not affect the result of the simulation and its value is taken to be 0.8 m_e, as defined in Ref. [163] The dashed lines show photon and exciton energies as a function of the in plane wave vector $k_{||}$.

Another part of the experiment addresses the occupation of the polariton states in the device, operated under ambient conditions. The overall, momentum-resolved PL spectrum of the structure is plotted in Figure 4.13(a). In stark contrast to previous reports discussing polariton emission with TMDC materials at room temperature [129], a pronounced occupation of the low energy states in the lower polartion branch and a reduced occupation of the excited polariton states are observed. The following model was used to analyze the luminescence experiment: In a first approximation, due to the comparably low particle numbers and high temperatures, a Boltzmann distribution law for the particles is assumed: $N_i \sim \exp(-E_i/k_B T)$, where N_i and E_i denote i-state population and energy, and k_B is the Boltzmann constant. The modeled PL is thus generated by a polariton gas at room temperature (T = 300 K). Another important assumption is that the emission stems from the photonic mode only and is broadened in energy according to the Lorentz distribution. This allows relating the PL intensity to the photonic Hopfield coefficients via:

$$I(k,E) \sim \sum_i \frac{\left|C_{ph}^i\right|^2 \exp(-E_i(k)/k_B T)}{(E-E_i(k))^2+\Gamma_{ph}^2}, \qquad (4.27)$$

where Γ_{ph} is the broadening of the photonic mode and the *i*-index spans over the two polariton branches. The value of $\Gamma_{ph}=15$ meV is extracted from the experimental data.

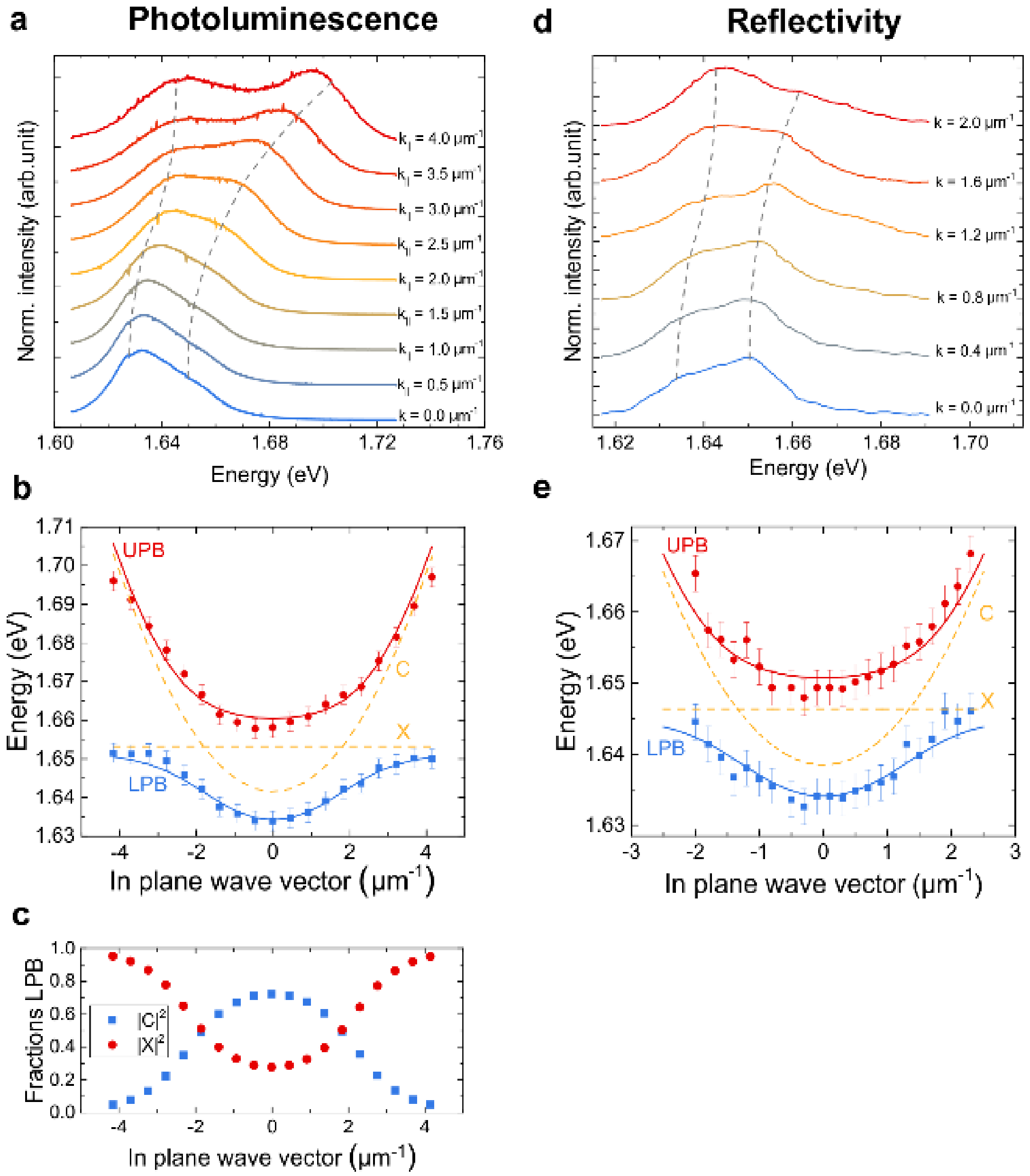

Figure 4.12: Exciton-polariton formation with Tamm-plasmons. (a) PL spectra recorded from the coupled device at room temperature at various in-plane momenta (depicted in a waterfall representation). Two pronounced resonances evolve in the system, which feature the characteristic anti-crossing behaviour of exciton-polaritons. (b) Energy–momentum dispersion relation of the lower and upper polariton branch at room temperature: the polariton energies are extracted by fitting spectra at various in-plane momenta (solid symbols). The coupled oscillator approach is employed to fit the data and to demonstrate agreement between experiment and theory (lines). (c) Plot of the exciton and photon fraction of the lower polariton branch as a function of the in-plane momentum extracted from coupled oscillator fit. (d) Inverted reflectivity spectra at different in-plane momenta. (e) Energy– momentum dispersion relation extracted from the reflectivity spectra. Figure taken from Ref. [107].

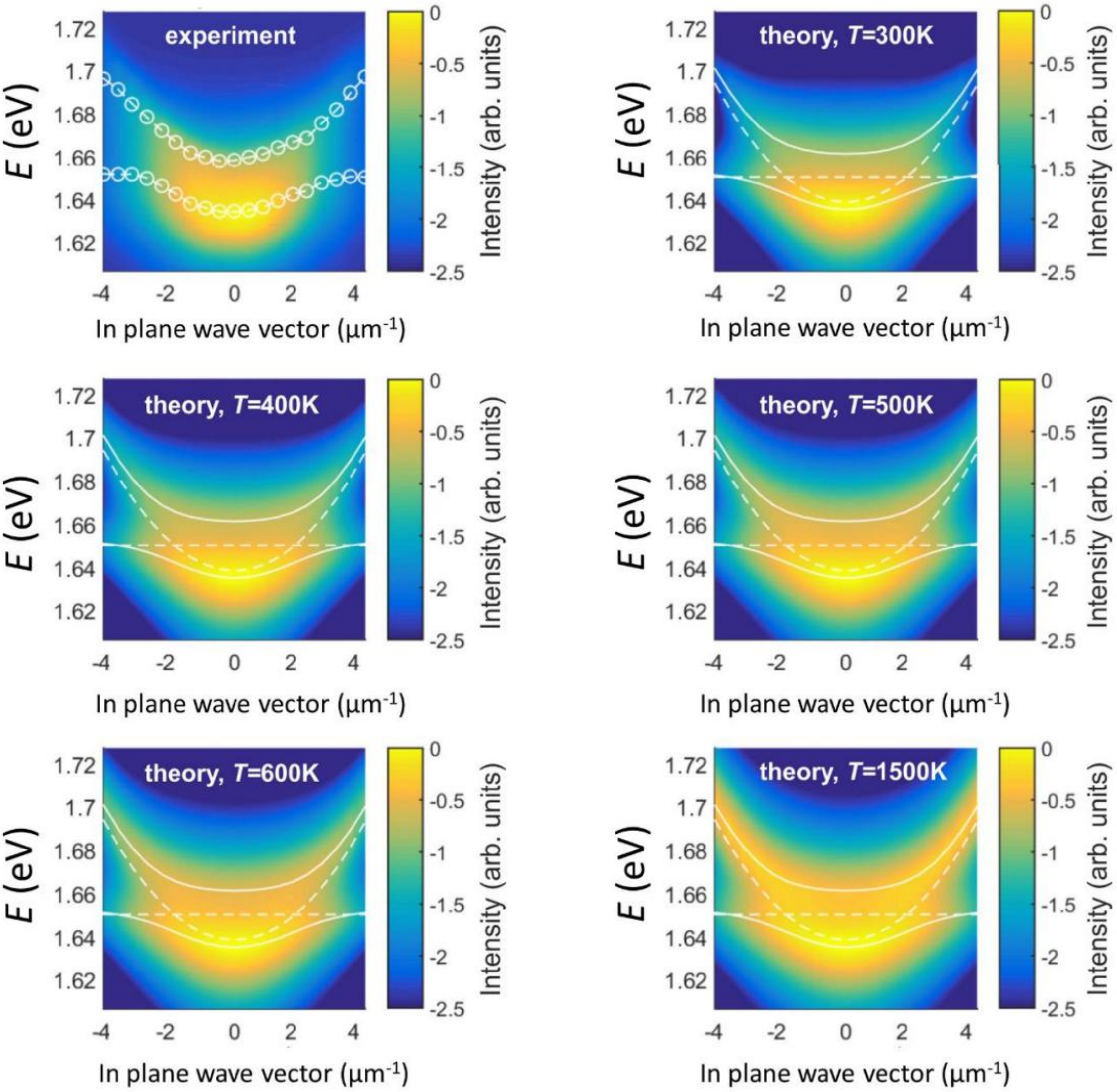

Figure 4.13: Experimental and theoretical polariton dispersion relations in the studied Tamm structure. (a) Room-temperature false colour intensity profile of the full polariton dispersion relation extracted from the PL measurements. (b) Model of the full dispersion by assuming a Boltzmann distribution of the quasi-particles with an effective temperature of 300 K c),d),e),f) the dispersion, modelled at higher temperatures; Figure taken from Ref. [107].

The experimental results and the theoretically calculated dispersion relation are plotted in Figure 4.13(a) and (b), respectively. Figure 4.13 (c),(d),(e), and (f) present additional theoretical simulations showing the momentum-resolved PL intensity as a function of temperature ranging from 300 K to 1500 K. The exciton-polariton gas in microcavities is usually out of thermal equilibrium with the crystal lattice because of the pumping and dissipation processes. The comparison with the experimental data in Figure 4.13(a) shows that the polariton gas is not cooled down to the lattice temperature in the experiments, and it may be characterized by an effective temperature of 300-500 K. Also, it should be noted that the emission from the upper polariton branch is amplified due to the high value of the photonic Hopfield coefficient at this branch at high momenta.

Here a good agreement between the theory and the experiment is achieved. While the used model is phenomenological and cannot account for any dynamic and microscopic effects in the system, it already serves as the first indicator that, despite the pronounced dissipation, polariton relaxation is indeed significant.

4.5 Conclusions

In conclusion, a clear evidence for the formation of exciton-polaritons was observed in a hybrid dielectric and polymer Tamm-plasmon-polariton device featuring an integrated single atomic layer of the transition metal dichalcogenide WSe_2. The distinct polariton dispersion relation was shown in angle-resolved PL and reflectivity measurements, both polariton branches were resolved including the characteristic parabolic energy minimum and the flattening towards the exciton band. The experimental data is supported by a coupled harmonic oscillator model, and a very good agreement is achieved both for the energy evolution of the polariton resonances as well as for the population of polariton eigenstates. This work represents a significant step towards the implementation of polariton condensates and non-linear experiments in the strong coupling regime based on single layers or stacks of several layers of TMDCs.

For future work it will be of particular interest for TMDC polaritonic experiments to harness the unique spinor and valley physics inherited by the atomic monolayers. Combining plasmonics and 2D active media in the strong light-matter coupling regime certainly carries great potential for building new architectures of highly integrated, non-linear optical circuits and logic devices which are operated at ultra-low powers and close to terahertz frequencies. The observation of room temperature polaritons paves the way towards the realization of hybrid Bose-Fermi system with integrated monolayers for the observation of exciton-polariton mediated superconductivity.

The experimental work described in this Chapter was carried out in the University of Würzburg, in the group lead by Dr. Christian Schneider. My contribution to this work includes theoretical simulations for the experiments, with the exception of simulations conducted in order to prepare the experimental samples. In particular, I calculated phase diagram and fitted oscillator strength in Section 4.2.3, partially developed variational approach and provided subsequent calculations in the Section 4.3 and provided modelling in Section 4.4. Finally I took part in preparation of the parts of the manuscripts that were further published in peer reviewed journals.

Appendix A

Parameter	Meaning	Value
ε	Permittivity	13.1
β_e	Electron reduced mass	0.063 m_0
β_h	Hole reduced mass	0.45 m_0
L	Distance between wells	10 nm
κ	Coulomb screening length	10 nm
a_B	Exciton Bohr radius	90Å
R_y	Exciton Rydberg	4.1 meV
d	Dipole moment	10 nm
$2g$	Rabi splitting	10 meV
X	Hopfield coefficient	$1/\sqrt{2}$
m_p	Polariton mass	$10^{-5}m_0$
UA	Polariton Interaction	0.24 μeV μm^2
d	Dipole moment	10 nm

Table A-1 the parameters, used in the calculations of the electron-electron interaction potential for GaAs-based structure in Chapter 3:

Bibliography

[1] J. Frenkel, "On the Transformation of light into Heat in Solids. I," *Physical Review Letters,* vol. 37, pp. 17-44, 1931.

[2] G. H. Wannier, "The Structure of Electronic Excitation Levels in Insulating Crystals," *Physical Review,* vol. 52, pp. 191-197, 1937.

[3] V. M. Agranovich, *Theory of excitons,* Nauka, Moscow, 1968.

[4] A. Kavokin, J. J. Baumberg, G. Malpuech and F. P. Laussy, Microcavities Oxford University Press, Oxford University Press, 2007.

[5] K. J. Vahala, "Optical microcavities," *Nature,* vol. 424, pp. 839-846, 2003.

[6] M. Cai, O. Painter and K. J. Vahala, "Observation of Critical Coupling in a Fiber Taper to a Silica-Microsphere Whispering-Gallery Mode System," *Physical Review Letters,* vol. 85, pp. 74-77, 2000.

[7] E. S. Sedov, E. D. Cherotchenko, S. M. Arakelian and A. V. Kavokin, "Light propagation in tunable exciton-polariton one-dimensional photonic crystals," *Physical Review B,* vol. 94, p. 125309, 2016.

[8] M. R. Vladimirova and A. V. Kavokin, "Edge electronic states in semiconductor superlattices," *Physics of the Solid State,* vol. 37, pp. 1178-1191, 1995.

[9] E. S. Sedov, I. V. Iorsh, S. M. Arakelian, A. P. Alodjants and A. Kavokin, "Hyperbolic Metamaterials with Bragg Polaritons," *Physical Review Letters,* vol. 114, p. 237402, 2015.

[10] A. Askitopoulos, L. Mouchliadis, I. Iorsh, G. Christmann, J. J. Baumberg, M. A. Kaliteevski, Z. Hatzopoulos and P. G. Savvidis, "Bragg Polaritons: Strong Coupling and Amplification in an Unfolded Microcavity," *Physical Review Letters,* vol. 106, p. 076401, 2011.

[11] E. Hanamura and H. Haug, "Condensation effects of excitons," *Physics Reports,* vol. 33, pp. 209-284, 1977.

[12] C. Weisbuch, M. Nishioka, A. Ishikawa and Y. Arakawa, "Observation of the coupled exciton-photon mode splitting in a semiconductor quantum microcavity," *Physical Review Letters ,*

vol. 69, pp. 3314-3317, 1992.

[13] R. Houdré, C. Weisbuch, R. P. Stanley, U. Oesterle, P. Pellandini and M. Ilegems, "Measurement of cavity-polariton dispersion curve from angle-resolved photoluminescence experiments," *Physical Review Letters,* vol. 73, p. 2043, 1994.

[14] R. Houdré, R. P. Stanley, U. Oesterle, M. Ilegems and C. Weisbuch, "Room-temperature cavity polaritons in a semiconductor microcavity," *Physical Review B,* vol. 49, p. 16761, 1994.

[15] P. G. Savvidis, J. J. Baumberg, R. M. Stevenson, M. S. Skolnick, D. M. Whittaker and J. S. Roberts, "Angle-Resonant Stimulated Polariton Amplifier," *Physical Review Letters,* vol. 84, pp. 1547-1550, 2000.

[16] M. H. Anderson, J. R. Ensher, M. R. Matthews, C. E. Wieman, E. A. Cornell and others, "Observation of Bose-Einstein condensation in a dilute atomic vapor," *Science,* vol. 269, pp. 198-201, 1995.

[17] K. B. Davis, M.-O. Mewes, M. R. Andrews, N. J. Van Druten, D. S. Durfee, D. M. Kurn and W. Ketterle, "Bose-Einstein condensation in a gas of sodium atoms," *Physical Review Letters,* vol. 75, p. 3969, 1995.

[18] Y. Sun, "Exciton-Polaritons in Thermal Equilibrium: From Bose-Einstein Condensation to Exciton-Polaritonics,", Ph.D dissertation, MIT, 2017.

[19] H. Deng, H. Haug and Y. Yamamoto, "Exciton-polariton bose-einstein condensation," *Reviews of Modern Physics,* vol. 82, p. 1489, 2010.

[20] J. Kasprzak, M. Richard, S. Kundermann, A. Baas, P. Jeambrun, J. M. J. Keeling, F. M. Marchetti, M. H. Szymanska, R. Andre, J. L. Staehli and others, "Bose-Einstein condensation of exciton polaritons," *Nature,* vol. 443, p. 409, 2006.

[21] H. Deng, G. Weihs, C. Santori, J. Bloch and Y. Yamamoto, "Condensation of semiconductor microcavity exciton polaritons," *Science,* vol. 298, pp. 199-202, 2002.

[22] J. D. Plumhof, T. Stöferle, L. Mai, U. Scherf and R. F. Mahrt, "Room-temperature Bose-Einstein condensation of cavity exciton-polaritons in a polymer," *Nature Materials,* vol. 13, p. 247, 2014.

[23] S. Christopoulos, G. B. von Högersthal and Höger, A. J. D. Grundy, P. G. Lagoudakis, A. V. Kavokin, J. J. Baumberg, G. Christmann, R. Butté, E. Feltin, J.-F. Carlin and N. Grandjean, "Room-Temperature Polariton Lasing in Semiconductor Microcavities," *Physical Review Letters,* vol. 98, p. 126405, 2007.

[24] M. Richard, J. Kasprzak, R. André, R. Romestain, L. S. Dang, G. Malpuech and A. Kavokin, "Experimental evidence for nonequilibrium Bose condensation of exciton polaritons," *Physical Review B,* vol. 72, p. 201301, 2005.

[25] G. Malpuech, A. Di Carlo, A. Kavokin, J. J. Baumberg, M. Zamfirescu and P. Lugli, "Room-temperature polariton lasers based on GaN microcavities," *Applied Physics Letters,* vol. 81, pp. 412-414, 2002.

[26] G. Christmann, R. Butté, E. Feltin, J.-F. Carlin and N. Grandjean, "Room temperature polariton lasing in a GaN∕AlGaN multiple quantum well microcavity," *Applied Physics Letters,* vol. 93, p. 051102, 2008.

[27] S. Kéna-Cohen and S. R. Forrest, "Room-temperature polariton lasing in an organic single-crystal microcavity," *Nature Photonics,* vol. 4, pp. 371-375, 2010.

[28] N. Grandjean, G. Christmann, E. Feltin, J. F. Carlin, A. Altoukhov, A. Castiglia and R. Butte, "Room-Temperature Polariton Laser," in *2008 Device Research Conference*, 2008.

[29] M. M. Glazov, H. Ouerdane, L. Pilozzi, G. Malpuech, A. V. Kavokin and A. D'Andrea, "Polariton-polariton scattering in microcavities: A microscopic theory," *Physical Review B,* vol. 80, p. 155306, 2009.

[30] A. Kavokin, G. Malpuech and M. Glazov, "Optical spin Hall effect," *Physical Review Letters,* vol. 95, p. 136601, 2005.

[31] F. Tassone, C. Piermarocchi, V. Savona, A. Quattropani and P. Schwendimann, "Bottleneck effects in the relaxation and photoluminescence of microcavity polaritons," *Physical Review B,* vol. 56, pp. 7554-7563, 1997.

[32] N. Bogoliubov, "On the theory of superfluidity," *Journal of Physics,* vol. 11, p. 23, 1947.

[33] M. Wouters and I. Carusotto, "Excitations in a nonequilibrium Bose-Einstein condensate of exciton polaritons," *Physical Review Letters,* vol. 99, p. 140402, 2007.

[34] E. Estrecho, T. Gao, N. Bobrovska, M. D. Fraser, M. Steger, L. Pfeiffer, K. West, T. C. H. Liew, M. Matuszewski, D. W. Snoke and others, "Spontaneous condensation of exciton polaritons in the single-shot regime," *arXiv preprint arXiv:1705.00469,* 2017.

[35] J. Steinhauer, R. Ozeri, N. Katz and N. Davidson, "Excitation Spectrum of a Bose-Einstein Condensate," *Physical Review Letters,* vol. 88, p. 120407, 2002.

[36] S. Utsunomiya, L. Tian, G. Roumpos, C. W. Lai, N. Kumada, T. Fujisawa, M. Kuwata-Gonokami, A. Löffler, S. Höfling, A. Forchel and others, "Observation of Bogoliubov excitations in exciton-polariton condensates," *Nature Physics,* vol. 4, p. 700, 2008.

[37] A. Kavokin, "Polaritons: The rise of the bosonic laser," *Nature Photonics,* vol. 7, pp. 591-592, 2013.

[38] V. Savona, "Fifteen years of microcavity polaritons," *The Physics of Semiconductor Microcavities,* 2007.

[39] G. Weihs, H. Deng, R. Huang, M. Sugita, F. Tassone and Y. Yamamoto, "Exciton--polariton lasing in a microcavity," *Semiconductor Science and Technology,* vol. 18, p. S386, 2003.

[40] T. C. H. Liew, M. M. Glazov, K. V. Kavokin, I. A. Shelykh, M. A. Kaliteevski and A. V. Kavokin, "Proposal for a Bosonic Cascade Laser," *Physical Review Letters ,* vol. 110, p. 047402, 2013.

[41] M. Tonouchi, "Cutting-edge terahertz technology," *Nature Photonics,* vol. 1, pp. 97-105, 2007.

[42] J. Faist, F. Capasso, D. L. Sivco, A. L. Hutchinson, C. Sirtori, S. N. G. Chu and A. Y. Cho, "Quantum cascade laser: Temperature dependence of the performance characteristics and high T0 operation," *Applied Physics Letters,* vol. 65, pp. 2901-2903, 1994.

[43] A. A. Bogdanov and R. A. Suris, "Mode structure of a quantum cascade laser," *Physical Review B,* vol. 83, p. 125316, 2011.

[44] R. F. Kazarinov and R. Suris, "Possibility of amplification of electromagnetic waves in a semiconductor with superlattice," *Sov. Phys.-Semicond.,* vol. 5, pp. 707-709, 1971.

[45] M. A. Kaliteevskii and K. A. Ivanov, "Double-boson stimulated terahertz emission in a polariton cascade laser," *Technical Physics Letters,* vol. 39, pp. 91-94, 2013.

[46] J. Ulrich, R. Zobl, K. Unterrainer, G. Strasser, E. Gornik, K. D. Maranowski and A. C. Gossard, "Temperature dependence of far-infrared electroluminescence in parabolic quantum wells," *Applied Physics Letters,* vol. 74, pp. 3158-3160, 1999.

[47] M. Geiser, F. Castellano, G. Scalari, M. Beck, L. Nevou and J. Faist, "Ultrastrong coupling regime and plasmon polaritons in parabolic semiconductor quantum wells," *Physical Review Letters,* vol. 108, p. 106402, 2012.

[48] R. Colombelli, C. Ciuti, Y. Chassagneux and C. Sirtori, "Quantum cascade intersubband polariton light emitters," *Semiconductor science and technology,* vol. 20, p. 985, 2005.

[49] I. G. Savenko, I. A. Shelykh and M. A. Kaliteevski, "Nonlinear Terahertz Emission in Semiconductor Microcavities," *Physical Review Letters,* vol. 107, p. 027401, 2011.

[50] A. V. Kavokin, I. A. Shelykh, T. Taylor and M. M. Glazov, "Vertical Cavity Surface Emitting Terahertz Laser," *Physical Review Letters,* vol. 108, p. 197401, 2012.

[51] B. Ferguson and X.-C. Zhang, "Materials for terahertz science and technology," *Nature Materials,* vol. 1, pp. 26-33, 2002.

[52] T. Hochrein, "Markets, Availability, Notice, and Technical Performance of Terahertz Systems: Historic Development, Present, and Trends," *Journal of Infrared, Millimeter, and Terahertz Waves,* vol. 36, pp. 235-254, 2015.

[53] C. Sirtori, F. Capasso, J. Faist, A. L. Hutchinson, D. L. Sivco and A. Y. Cho, "Resonant tunneling in quantum cascade lasers," *IEEE Journal of Quantum Electronics,* vol. 34, pp. 1722-1729, 1998.

[54] B. S. Williams, S. Kumar, Q. Hu and J. L. Reno, "Operation of terahertz quantum-cascade lasers at 164 K in pulsed mode and at 117 K in continuous-wave mode," *Optics Express,* vol. 13, pp. 3331-3339, 2005.

[55] B. S. Williams, "Terahertz quantum-cascade lasers," *Nature Photonics,* vol. 1, pp. 517-525, 2007.

[56] M. A. Belkin, F. Capasso, F. Xie, A. Belyanin, M. Fischer, A. Wittmann and J. Faist, "Room temperature terahertz quantum cascade laser source based on intracavity difference-frequency generation," *Applied Physics Letters,* vol. 92, p. 201101, 2008.

[57] J. L. Carthy, "Novel Methods of Terahertz Generation with Semiconductor Microcavities and Beam Steering", Ph.D dissertation, University of Southampton, 2017.

[58] Y. Bai, S. Slivken, S. Kuboya, S. R. Darvish and M. Razeghi, "Quantum cascade lasers that emit more light than heat," *Nature Photonics,* vol. 4, pp. 99-102, 2010.

[59] P. Q. Liu, A. J. Hoffman, M. D. Escarra, K. J. Franz, J. B. Khurgin, Y. Dikmelik, X. Wang, J.-Y. Fan and C. F. Gmachl, "Highly power-efficient quantum cascade lasers," *Nature Photonics,* vol. 4, pp. 95-98, 2010.

[60] H. Soda, K.-i. Iga, C. Kitahara and Y. Suematsu, "GaInAsP/InP Surface Emitting Injection Lasers," *Japanese Journal of Applied Physics,* vol. 18, p. 2329, 1979.

[61] R. A. Kaindl, D. Hägele, M. A. Carnahan and D. S. Chemla, "Transient terahertz spectroscopy of excitons and unbound carriers in quasi-two-dimensional electron-hole gases," *Physical Review B,* vol. 79, p. 045320, 2009.

[62] I. M. Catalano, A. Cingolani, R. Cingolani, M. Lepore and K. Ploog, "Two-photon spectroscopy in GaAs/$Al_xGa_{1-x}As$ multiple quantum wells," *Physical Review B,* vol. 40, pp. 1312-1315, 1989.

[63] F. Laussy, "Quantum Dynamics of Microcavity Polaritons", Ph.D dissertation, Blaise Pascal University, 2005.

[64] E. L. Ivchenko, Optical spectroscopy of semiconductor nanostructures, Alpha Science Intĺ Ltd., 2005.

[65] A. V. Trifonov, S. N. Korotan, A. S. Kurdyubov, I. Y. Gerlovin, I. V. Ignatiev, Y. P. Efimov, S. A. Eliseev, V. V. Petrov, Y. K. Dolgikh, V. V. Ovsyankin and others, "Nontrivial relaxation dynamics of excitons in high-quality InGaAs/GaAs quantum wells," *Physical Review B,* vol. 91, p. 115307, 2015.

[66] R. Butté, G. Delalleau, A. I. Tartakovskii, M. S. Skolnick, V. N. Astratov, J. J. Baumberg, G. Malpuech, A. Di Carlo, A. V. Kavokin and J. S. Roberts, "Transition from strong to weak coupling and the onset of lasing in semiconductor microcavities," *Physical Review B,* vol. 65, p. 205310, 2002.

[67] H. Mathieu, P. Lefebvre, J. Allègre, B. Gil and A. Regreny, "Differential spectroscopy of GaAs-$Ga_{1-x}Al_xAs$ quantum wells: An unambiguous identification of light-hole and heavy-hole

states," *Physical Review B,* vol. 36, p. 6581, 1987.

[68] A. V. Trifonov, E. D. Cherotchenko, J. L. Carthy, I. V. Ignatiev, A. Tzimis, S. Tsintzos, Z. Hatzopoulos, P. G. Savvidis and A. V. Kavokin, "Dynamics of the energy relaxation in a parabolic quantum well laser," *Physical Review B,* vol. 93, p. 125304, 2016.

[69] T. C. Damen, J. Shah, D. Y. Oberli, D. S. Chemla, J. E. Cunningham and J. M. Kuo, "Dynamics of exciton formation and relaxation in GaAs quantum wells," *Physical Review B,* vol. 42, pp. 7434-7438, 1990.

[70] V. P. Kochereshko, M. V. Durnev, L. Besombes, H. Mariette, V. F. Sapega, A. Askitopoulos, I. G. Savenko, T. C. H. Liew, I. A. Shelykh, A. V. Platonov and others, "Lasing in Bose-Fermi mixtures," *Scientific Reports,* vol. 6, 2016.

[71] J. Bloch, B. Sermage, M. Perrin, P. Senellart, R. André and L. S. Dang, "Monitoring the dynamics of a coherent cavity polariton population," *Physical Review B,* vol. 71, p. 155311, 2005.

[72] L. Schultheis, J. Kuhl, A. Honold and C. W. Tu, "Ultrafast Phase Relaxation of Excitons via Exciton-Exciton and Exciton-Electron Collisions," *Physical Review Letters ,* vol. 57, pp. 1635-1638, 1986.

[73] G. Khitrova, H. M. Gibbs, F. Jahnke, M. Kira and S. W. Koch, "Nonlinear optics of normal-mode-coupling semiconductor microcavities," *Reviews of Modern Physics,* vol. 71, p. 1591, 1999.

[74] A. Kavokin and G. Malpuech, Cavity polaritons, vol. 32, Academic Press, 2003.

[75] A. Kavokin and G. Malpuech, Thin films and nanostructures, vol. 32, Academic Press, 2003.

[76] E. D. Cherotchenko, T. Espinosa-Ortega, A. V. Nalitov, I. A. Shelykh and A. V. Kavokin, "Superconductivity in semiconductor structures: the excitonic mechanism," *Superlattices and Microstructures,* vol. 90, pp. 170-175, 2016.

[77] I. A. Shelykh, T. Taylor and A. V. Kavokin, "Rotons in a hybrid Bose-Fermi system," *Physical Review Letters,* vol. 105, p. 140402, 2010.

[78] M. Matuszewski, T. Taylor and A. V. Kavokin, "Exciton supersolidity in hybrid Bose-Fermi systems," *Physical Review Letters,* vol. 108, p. 060401, 2012.

[79] O. Cotleţ, S. Zeytinoğlu, M. Sigrist, E. Demler and A. Imamoğlu, "Superconductivity and other collective phenomena in a hybrid Bose-Fermi mixture formed by a polariton condensate and an electron system in two dimensions," *Physical Review B,* vol. 93, p. 054510, 2016.

[80] J. File and R. G. Mills, "Observation of persistent current in a superconducting solenoid," *Physical Review Letters,* vol. 10, p. 93, 1963.

[81] W. Meissner and R. Ochsenfeld, "A new effect in penetration of superconductors," *Die Naturwissenschaften,* vol. 21, pp. 787-788, 1933.

[82] E. Maxwell, "Isotope effect in the superconductivity of mercury," *Physical Review,* vol. 78, p. 477, 1950.

[83] C. A. Reynolds, B. Serin and L. B. Nesbitt, "The isotope effect in superconductivity. I. Mercury," *Physical Review,* vol. 84, p. 691, 1951.

[84] B. Serin, C. A. Reynolds and C. Lohman, "The Isotope Effect in Superconductivity. II. Tin and Lead," *Physical Review,* vol. 86, p. 162, 1952.

[85] H. Fröhlich, "Theory of the superconducting state. I. The ground state at the absolute zero of temperature," *Physical Review,* vol. 79, p. 845, 1950.

[86] F. London and H. London, "The electromagnetic equations of the supraconductor," in *Proceedings of the Royal Society of London A: Mathematical, Physical and Engineering Sciences*, 1935.

[87] J. Bardeen, L. N. Cooper and J. R. Schrieffer, "Theory of Superconductivity," *Physical Review,* vol. 108, pp. 1175-1204, 1957.

[88] L. N. Cooper, "Bound Electron Pairs in a Degenerate Fermi Gas," *Physical Review,* vol. 104, pp. 1189-1190, 1956.

[89] A. S. Davydov, "Quantum Mechanics [in Russian], Fizmatgiz, Moscow (1963)," *Google Scholar,* p. 171, 1976.

[90] W. A. Little, "Possibility of synthesizing an organic superconductor," *Physical Review,* vol. 134, p. A1416, 1964.

[91] V. L. Ginzburg, "The problem of high-temperature superconductivity. II," *Physics-Uspekhi,*

vol. 13, pp. 335-352, 1970.

[92] D. Allender, J. Bray and J. Bardeen, "Model for an Exciton Mechanism of Superconductivity," *Phys. Rev. B,* vol. 7, pp. 1020-1029, 1973.

[93] F. P. Laussy, A. V. Kavokin and I. A. Shelykh, "Exciton-polariton mediated superconductivity," *Physical Review Letters,* vol. 104, p. 106402, 2010.

[94] F. P. Laussy, T. Taylor, I. A. Shelykh and A. V. Kavokin, "Superconductivity with excitons and polaritons: review and extension," *Journal of Nanophotonics,* vol. 6, pp. 64502-1, 2012.

[95] H. Haug and S. W. Koch, Quantum theory of the optical and electronic properties of semiconductors, World Scientific Publishing Co Inc, 2009, 2009.

[96] F. Tassone and Y. Yamamoto, "Exciton-exciton scattering dynamics in a semiconductor microcavity and stimulated scattering into polaritons," *Physical Review B,* vol. 59, p. 10830, 1999.

[97] H. Ibach and H. Lüth, "Solid-state physics: an introduction to principles of material science," *Advanced Texts in Physics, Springer-Verlag berlin Heidelberg New York,* 2003.

[98] L. D. Landau and E. M. Lifshitz, "Quantum Mechanics, Non-Relativistic Theory (Pergamon, New York)," 1977.

[99] T. Champel and V. P. Mineev, "de Haas--van Alphen effect in two-and quasi-two-dimensional metals and superconductors," *Philosophical Magazine B,* vol. 81, pp. 55-74, 2001.

[100] P. Skopelitis, E. Cherotchenko, A. Posazhennikova and A. Kavokin, "The interplay of phonon and exciton-mediated superconductivity in hybrid semiconductor-superconductor structures," *In preparation,* 2017.

[101] C. R. Hunt, D. Nicoletti, S. Kaiser, T. Takayama, H. Takagi and A. Cavalleri, "Two distinct kinetic regimes for the relaxation of light-induced superconductivity in $La_{1.675}Eu_{0.2}Sr_{0.125}CuO_4$," *Physical Review B,* vol. 91, p. 020505, 2015.

[102] M. Mitrano, A. Cantaluppi, D. Nicoletti, S. Kaiser, A. Perucchi, S. Lupi, P. Di Pietro, D. Pontiroli, M. Riccò, S. R. Clark, D. Jaksch and A. Cavalleri, "Possible light-induced superconductivity in K3C60 at high temperature," *Nature,* vol. 530, pp. 461-464, 2016.

[103] J. A. Wilson and A. D. Yoffe, "The transition metal dichalcogenides discussion and interpretation of the observed optical, electrical and structural properties," *Advances in Physics,* vol. 18, pp. 193-335, 1969.

[104] K. S. Novoselov, A. K. Geim, S. V. Morozov, D. Jiang, Y. Zhang, S. V. Dubonos, I. V. Grigorieva and A. A. Firsov, "Electric Field Effect in Atomically Thin Carbon Films," *Science,* vol. 306, pp. 666-669, 2004.

[105] Q. H. Wang, K. Kalantar-Zadeh, A. Kis, J. N. Coleman and M. S. Strano, "Electronics and optoelectronics of two-dimensional transition metal dichalcogenides," *Nature Nanotechnology,* vol. 7, pp. 699-712, 2012.

[106] J. S. Ross, S. Wu, H. Yu, N. J. Ghimire, A. M. Jones, G. Aivazian, J. Yan, D. G. Mandrus, D. Xiao, W. Yao and X. Xu, "Electrical control of neutral and charged excitons in a monolayer semiconductor," *Nature Communications,* vol. 4, p. 1474, 2013.

[107] N. Lundt, S. Klembt, E. Cherotchenko, S. Betzold, O. Iff, A. V. Nalitov, M. Klaas, C. P. Dietrich, A. V. Kavokin, S. Höfling and C. Schneider, "Room-temperature Tamm-plasmon exciton-polaritons with a WSe_2 monolayer," *Nature Communications,* vol. 7, 2016.

[108] A. Castellanos-Gomez, M. Barkelid, A. M. Goossens, V. Calado, H. S. J. van der Zant. and S. G.A., "Laser-Thinning of MoS_2: On Demand Generation of a Single-Layer Semiconductor," *Nano Letters,* vol. 12, pp. 3187-3192, 2012.

[109] S. Brunken, R. Mientus, S. Seeger and K. Ellmer, "The mechanism of nickel sulfide induced rapid crystallization of highly textured tungsten disulfide (WS_2) thin films: An in situ real-time diffraction study," *Journal of Applied Physics,* vol. 103, p. 063501, 2008.

[110] X. Ling, Y.-H. Lee, Y. Lin, W. Fang, L. Yu, M. S. Dresselhaus and J. Kong, "Role of the Seeding Promoter in MoS_2 Growth by Chemical Vapor Deposition," *Nano Letters,* vol. 14, pp. 464-472, 2014.

[111] M. Okada, T. Sawazaki, K. Watanabe, T. Taniguch, H. Hibino, H. Shinohara and R. Kitaura, "Direct Chemical Vapor Deposition Growth of WS_2 Atomic Layers on Hexagonal Boron Nitride," *ACS Nano,* vol. 8, pp. 8273-8277, 2014.

[112] S. Wang, Y. Rong, Y. Fan, M. Pacios, H. Bhaskaran, K. He and J. H. Warner, "Shape Evolution of Monolayer MoS_2 Crystals Grown by Chemical Vapor Deposition," *Chemistry of Materials,*

vol. 26, pp. 6371-6379, 2014.

[113] V. Podzorov, M. E. Gershenson, C. Kloc, R. Zeis and E. Bucher, "High-mobility field-effect transistors based on transition metal dichalcogenides," *Applied Physics Letters,* vol. 84, 2004.

[114] A. Kuc, N. Zibouche and T. Heine, "Influence of quantum confinement on the electronic structure of the transition metal sulfide TS_2," *Physical Review B,* vol. 83, p. 245213, 2011.

[115] A. Splendiani, L. Sun, Y. Zhang, T. Li, J. Kim, C.-Y. Chim, G. Galli and F. Wang, "Emerging Photoluminescence in Monolayer MoS_2," *Nano Letters,* vol. 10, pp. 1271-1275, 2010.

[116] A. Kumar and P. K. Ahluwalia, "Electronic structure of transition metal dichalcogenides monolayers 1H-MX2 (M = Mo, W; X = S, Se, Te) from ab-initio theory: new direct band gap semiconductors," *The European Physical Journal B,* vol. 85, p. 186, 2012.

[117] C.-H. Lee, G.-H. Lee, M. van der Zande and Arend, W. Chen, Y. Li, M. Han, X. Cui, G. Arefe, C. Nuckolls, T. F. Heinz, J. Guo, J. Hone and P. Kim, "Atomically thin p-n junctions with van der Waals heterointerfaces," *Nature Nanotechnology,* vol. 9, pp. 676-681, 2014.

[118] Y. Li, A. Chernikov, X. Zhang, A. Rigosi, H. M. Hill, M. van der Zande and Arend, D. A. Chenet, E.-M. Shih, J. Hone and T. F. Heinz, "Measurement of the optical dielectric function of monolayer transition-metal dichalcogenides: MoS_2, $MoSe_2$, WS_2, and WSe_2," *Physical Review B,* vol. 90, p. 205422, 2014.

[119] A. Kormányos, G. Burkard, M. Gmitra, J. Fabian, V. Zólyomi, N. D. Drummond and V. Fal’ko, "k · p theory for two-dimensional transition metal dichalcogenide semiconductors," *2D Materials,* vol. 2, p. 022001, 2015.

[120] C. Zhang, H. Wang, W. Chan, C. Manolatou and F. Rana, "Absorption of light by excitons and trions in monolayers of metal dichalcogenide MoS_2: Experiments and theory," *Physical Review B,* vol. 89, p. 205436, 2014.

[121] B. W. H. Baugher, H. O. H. Churchill, Y. Yang and P. Jarillo-Herrero, "Optoelectronic devices based on electrically tunable p-n diodes in a monolayer dichalcogenide," *Nature Nanotechnology,* vol. 9, pp. 262-267, 2014.

[122] F. Xia, H. Wang, D. Xiao, M. Dubey and A. Ramasubramaniam, "Two-dimensional material nanophotonics," *Nature Photonics,* vol. 8, pp. 899-907, 2014.

[123] H. Tian, M. L. Chin, S. Najmaei, Q. Guo, F. Xia, H. Wang and M. Dubey, "Optoelectronic devices based on two-dimensional transition metal dichalcogenides," *Nano Research,* vol. 9, pp. 1543-1560, 2016.

[124] M. Koperski, K. Nogajewski, A. Arora, V. Cherkez, P. Mallet, J. Veuillen, J. Marcus, P. Kossacki and M. Potemski, "Single photon emitters in exfoliated WSe_2 structures," *Nature Nanotechnology,* vol. 10, pp. 503-506, 2015.

[125] Y. Ye, Z. J. Wong, X. lu, X. Ni, H. Zhu, X. Chen, Y. Wang and X. Zhang, "Monolayer excitonic laser," *Nature Photonics,* vol. 9, p. 733–737, 2015.

[126] L. Britnell, R. M. Ribeiro, A. Eckmann, R. Jalil, B. D. Belle, A. Mishchenko, Y.-J. Kim, R. V. Gorbachev, T. Georgiou, S. V. Morozov, A. N. Grigorenko, A. K. Geim, C. Casiraghi, A. H. C. Neto and K. S. Novoselov, "Strong Light-Matter Interactions in Heterostructures of Atomically Thin Films," *Science,* vol. 340, pp. 1311-1314, 2013.

[127] O. Lopez-Sanchez, D. Lembke, M. Kayci, A. Radenovic and A. Kis, "Ultrasensitive photodetectors based on monolayer MoS_2," *Nature Nanotechnology,* vol. 8, pp. 497-501, 2013.

[128] M. Furchi, A. Urich, A. Pospischil, G. Lilley, K. Unterrainer, H. Detz, P. Klang, A. M. Andrews, W. Schrenk, G. Strasser and T. Mueller, "Microcavity-Integrated Graphene Photodetector," *Nano Letters,* vol. 12, pp. 2773-2777, 2012.

[129] X. Liu, T. Galfsky, Z. Sun, F. Xia, E.-c. Lin, Y.-H. Lee, S. Kéna-Cohen and V. M. Menon, "Strong light-matter coupling in two-dimensional atomic crystals," *Nature Photonics,* vol. 9, pp. 30-34, 2015.

[130] S. Dufferwiel, S. Schwarz, F. Withers, A. A. P. Trichet, F. Li, M. Sich, O. Del Pozo-Zamudio, C. Clark, A. Nalitov, D. D. Solnyshkov, G. Malpuech, K. S. Novoselov, J. M. Smith, M. S. Skolnick, D. N. Krizhanovskii and A. I. Tartakovskii, "Exciton-polaritons in van der Waals heterostructures embedded in tunable microcavities," *Nature Communications,* vol. 6, pp. 8579--, 2015.

[131] G. Wang, C. Robert, A. Suslu, B. Chen, S. Yang, S. Alamdari, I. C. Gerber, T. Amand, X. Marie, S. Tongay and B. Urbaszek, "Spin-orbit engineering in transition metal dichalcogenide alloy monolayers," *Nature Communications,* vol. 6, p. 10110, 2015.

[132] M. Fraser, "Coherent exciton-polariton devices," *Semiconductor Science and Technology,* 2017.

[133] A. Chernikov, T. C. Berkelbach, H. M. Hill, A. Rigosi, Y. Li, O. B. Aslan, D. R. Reichman, M. S. Hybertsen and T. F. Heinz, "Exciton Binding Energy and Nonhydrogenic Rydberg Series in Monolayer WS_2," *Physical Review Letters,* vol. 113, p. 076802, 2014.

[134] A. T. Hanbicki, M. Currie, G. Kioseoglou, A. L. Friedman and B. T. Jonker, "Measurement of high exciton binding energy in the monolayer transition-metal dichalcogenides WS_2 and WSe_2," *Solid State Communications,* vol. 203, pp. 16-20, 2015.

[135] L. C. Andreani, G. Panzarini, A. V. Kavokin and M. Vladimirova, "Effect of inhomogeneous broadening on optical properties of excitons in quantum wells," *Physical Review B,* vol. 57, pp. 4670-4680, 1998.

[136] A. Auffèves, D. Gerace, J.-M. Gérard, M. F. Santos, L. C. Andreani and J.-P. Poizat, "Controlling the dynamics of a coupled atom-cavity system by pure dephasing," *Physical Review B,* vol. 81, p. 245419, 2010.

[137] Y. V. Morozov and M. Kuno, "Optical constants and dynamic conductivities of single layer MoS_2, $MoSe_2$, and WSe_2," *Applied Physics Letters,* vol. 107, p. 083103, 2015.

[138] N. Lundt, A. Maryński, E. Cherotchenko, A. Pant, X. Fan, S. Tongay, G. Sęk, A. V. Kavokin, S. Höfling and C. Schneider, "Monolayered $MoSe_2$: A candidate for room temperature polaritonics," *2D Materials,* vol. 4, p. 015006, 2016.

[139] Y. P. Varshni, "Temperature dependence of the energy gap in semiconductors.," *Physica,* Vols. 34, 149–154, 1967.

[140] A. Arora, K. Nogajewski, M. Molas, M. Koperski and M. Potemski, "Exciton band structure in layered $MoSe_2$: from a monolayer to the bulk limit.," *Nanoscale,* vol. 7, p. 20769 – 20775, 2015.

[141] G. Moody, C. Kavir Dass, K. Hao, C.-H. Chen, L.-J. Li, A. Singh, K. Tran, G. Clark, X. Xu, G. Berghäuser, E. Malic, A. Knorr and X. Li, "Intrinsic homogeneous linewidth and broadening mechanisms of excitons in monolayer transition metal dichalcogenides," *Nature Communications,* vol. 6, pp. 8315--, 2015.

[142] J. Feldmann, "Linewidth dependence of radiative exciton lifetimes in quantum wells,"

Physical Review Letters , vol. 59, p. 2337–2340, 1987.

[143] T. Jakubczyk, V. Delmonte, M. Koperski, K. Nogajewski, C. Faugeras, W. Langbein, M. Potemski and J. Kasprzak, "Radiatively Limited Dephasing and Exciton Dynamics in $MoSe_2$ Monolayers Revealed with Four-Wave Mixing Microscopy," *Nano Letters,* vol. 16, pp. 5333-5339, 2016.

[144] D. Rosales, T. Bretagnon, B. Gil, A. Kahouli, J. Brault, B. Damilano, J. Massies, M. V. Durnev and A. V. Kavokin, "Excitons in nitride heterostructures: From zero- to one-dimensional behavior," *Physical Review B,* vol. 88, p. 125437, 2013.

[145] B. Radisavljevic, A. Radenovic, J. Brivo, V. Giakometti and A. Kis, "Single-layer MoS_2 transistors," *Nature Nanotechnology,* vol. 6, pp. 147-150, 2011.

[146] W. Ossau, D. R. Yakovlev, C. Y. Hu, V. P. Kochereshko, G. V. Astakhov, R. A. Suris, P. C. M. Christianen and J. C. Maan, "Exciton-electron interaction in quantum wells with a two dimensional electron gas of low density," *Physics of the Solid State,* vol. 41, pp. 751-756, 1999.

[147] V. P. Kochereshko, D. R. Yakovlev, R. A. Suris, W. Ossau, G. Landwehr, T. Wojtowicz, M. Kutrowski, G. Karczewski and J. Kossut, "Exciton—electron interactions in CdTe/CdMgTe modulation-doped QW structures," *Journal of Crystal Growth,* vol. 184, pp. 826-830, 1998.

[148] N. Lundt, E. Cherotchenko, O. Iff, X. Fan, Y. Shen, P. Bigenwald, A. Kavokin, S. Höfling and C. Schneider, "The interplay between excitons and trions in a monolayer of $MoSe_2$," *arXiv preprint arXiv:1702.04231,* 2017.

[149] V. Huard, R. T. Cox, K. Saminadayar, A. Arnoult and S. Tatarenko, "Bound States in Optical Absorption of Semiconductor Quantum Wells Containing a Two-Dimensional Electron Gas," *Physical Review Letters,* vol. 84, pp. 187-190, 2000.

[150] K. F. Mak, C. Lee, J. Hone, J. Shan and T. F. Heinz, "Atomically Thin MoS_2: A New Direct-Gap Semiconductor," *Physical Review Letters,* vol. 105, p. 136805, 2010.

[151] F. G. Pikus, *Fiz. Tekh. Poluprovodn.,* vol. 26, 1992.

[152] D. Xiao, G.-B. Liu, W. Feng, X. Xu and W. Yao, "Coupled Spin and Valley Physics in Monolayers of MoS_2 and Other Group-VI Dichalcogenides," *Physical Review Letters,* vol. 108, p. 196802, 2012.

[153] N. S. Rytova, "Screened potential of a point charge in the thin film," *Vestnik MSU (in Russian),* vol. 3, pp. 30-37, 1967.

[154] L. Keldysh, "Coulomb interaction in thin semiconductor and semimetal films," *Soviet Journal of Experimental and Theoretical Physics Letters,* vol. 29, p. 658, 1979.

[155] T. Ando, A. B. Fowler and F. Stern, "Electronic properties of two-dimensional systems," *Review of Modern Physics,* vol. 54, pp. 437-672, 1982.

[156] F. Stern, "Polarizability of a Two-Dimensional Electron Gas," *Physical Review Letters,* vol. 18, pp. 546-548, 1967.

[157] D. A. Dahl and L. J. Sham, "Electrodynamics of quasi-two-dimensional electrons," *Physical Review B,* vol. 16, pp. 651-661, 1977.

[158] A. Esser, E. Runge, R. Zimmermann and W. Langbein, "Photoluminescence and radiative lifetime of trions in GaAs quantum wells," *Physical Review B,* vol. 62, p. 8232, 2000.

[159] M. V. Durnev and M. M. Glazov, "Excitons and trions in two-dimensional semiconductors based on transition metal dichalcogenides," *Phys. Usp,* 2017.

[160] G. Wang, A. Chernikov, M. M. Glazov, T. F. Heinz, X. Marie, T. Amand and B. Urbaszek, "Excitons in atomically thin transition metal dichalcogenides," *arXiv preprint arXiv:1707.05863,* 2017.

[161] V. Shahnazaryan, I. Iorsh, I. A. Shelykh and O. Kyriienko, "Exciton-exciton interaction in transition-metal dichalcogenide monolayers," *Physical Review B,* vol. 96, p. 115409, 2017.

[162] W. L. Barnes, A. Dereux and T. W. Ebbesen, "Surface plasmon subwavelength optics," *Nature,* vol. 424, pp. 824-830, 2003.

[163] M. I. Vasilevskiy, D. G. Santiago-Pérez, C. Trallero-Giner, N. M. R. Peres and A. Kavokin, "Exciton polaritons in two-dimensional dichalcogenide layers placed in a planar microcavity: Tunable interaction between two Bose-Einstein condensates," *Physical Review B,* vol. 92, p. 245435, 2015.